CHANGES IN DEFORMATION WITHIN CARBONIFEROUS MASS TRANSPORT DEPOSITS, AGUA DE LA PEÑA CREEK (SAN JUAN, ARGENTINA)

by

Cole Schmidt

A Thesis Submitted in

Partial Fulfillment of the

Requirements for the Degree of

Masters of Science

in Geosciences

at

The University of Wisconsin-Milwaukee

August 2025

ABSTRACT

CHANGES IN DEFORMATION WITHIN CARBONIFEROUS MASS TRANSPORT DEPOSITS, AGUA DE LA PEÑA CREEK (SAN JUAN, ARGENTINA)

by

Cole Bradley Schmidt

The University of Wisconsin-Milwaukee, 2025
Under the Supervision of Professor John Isbell

Mass transport deposits (MTDs) play a critical role in sediment reworking and distribution within marine environments. Agua de la Peña Creek (San Juan Province, Argentina) provides a well-exposed Carboniferous succession that records the final stages of the Late Paleozoic Ice Age (LPIA) along the western margin of Gondwana. This succession, up to 1000 meters thick, consists of proglacial to subglacial sediment ranging from distal turbidites and shales to MTDs containing exotic clasts. Previous studies have primarily focused on the general characteristics and deformation of these deposits. By pairing stratigraphic sections with high-resolution imagery, this study aims to provide a detailed assessment of a singular flow evolution across a 300-meter outcrop, improving an understanding of mass transport process within proglacial to post-glacial environments along this section of western Gondwana. The study integrates deformation analysis, sediment body geometry, and high-resolution imagery to assess a singular mass transport at multiple scales. Findings indicate that (1) the basal shear zone of the studied MTD exhibits a transitional domain between erosion and liquefaction; (2) vertical deformation patterns in the MTD show a progressive increase in mixing and homogenization

intensity from the base upward, with localized zones of complex deformation and kinematic indicators; (3) laterally in the MTD, block abundance and deformation varies broadly across an oblique cut to the overall direction of flow, which is likely due to lobe deflection, energy dissipation through unconfined flow distribution, and/or the total distance from the headwall scarp; (4) there is no evidence of glacial proximal-distal influence within the studied deposit. These results refine models of basal deformation, as well as vertical and lateral variability. Furthermore, they offer a comparative framework for evaluating deformation patterns in other depositional settings within ancient deposits.

TABLE OF CONTENTS

LIST OF FIGURES

LIST OF TABLES

ACKNOWLEDGEMENTS

First and foremost, I would like to express my sincere gratitude to my advisor, Dr. John Isbell. John, I have appreciated every facet of our relationship since I first met you during my undergraduate years. From our daily conversations about peanut M&Ms and hiding pesos, to the invaluable life wisdom you've shared far beyond the realm of sedimentology, your mentorship has been a constant source of support. Your encouragement, passion for research, and willingness to give your time have made this project so rewarding. The challenges you've presented through this project have pushed me to grow both academically and personally, and there are truly no words to fully express the impact you've had on my life over the past four years.

I would like to thank Allison Kusick for the many roles she has held throughout my undergraduate and graduate years. Allison, no one else could ever hold the unique combination of best friend, teacher, mentor, roommate, "mama," and honey badger—and I sincerely appreciate that about you. You have continually been a role model to me as I've grown both personally and professionally. I'm especially grateful for your encouragement to pursue graduate studies following my undergraduate degree; your presence in my life has made a lasting impact, and I wouldn't be here without it.

I would like to acknowledge the UWM Department of Geosciences, along with the UWM Center for Latin American and Caribbean Studies, for their educational and financial support throughout this journey. I also extend my sincere thanks to my committee members, Dr. Nicholas Fedorchuk and Dr. Eduardo Menozzo da Rosa, for their time, insight, and support. I truly appreciate the time and thought you dedicated to my defense and the constructive feedback you provided regarding my research.

Finally, I would like to thank several individuals who have had a significant impact on my research during my time at UWM. I am especially grateful to our Argentine colleagues—Dr. Oscar Limarino and Dr. Pablo Joaquín Alonso-Muruaga (University of Buenos Aires), as well as Dr. Carina Columbi and Carlos Mario Alarcón (University of San Juan)—for their invaluable support and guidance during fieldwork in Argentina. I would also like to thank Ross Brandolino, Kelly Otto, and Madeline Woller for being exceptional field assistants and an incredible support system throughout both my research and studies.

1). Introduction

Mass transport deposits (MTDs) are critical agents of sediment redistribution in marine settings, exerting a fundamental control on basin architecture and depositional patterns. Their study provides valuable insights into paleoenvironmental reconstruction, including the extent and duration of glacial influence in sedimentary basins. In glaciogenic systems, MTDs can record the dynamics of ice-margin retreat, sediment flux, and post-glacial reworking (Benn & Evans, 2010; Evans, 2018; Isbell et al., 2021; Catuneanu, 2022). In non-glacial environments MTDs are common in basin margin settings due to changes in sea level, high sedimentation rates, seismic activity, and collapse of shelf-edge deposits (Flores, 1959; Alsop & Holdsworth, 2004; Posamentier & Walker, 2006; Ogata et al., 2012; Vesely et al., 2018; Catuneanu, 2022). Beyond academic significance, understanding MTDs has important applied implications: they can serve as hydrocarbon reservoirs or seals in subsurface systems, represent key stratigraphic markers of paleoenvironmental change, and inform hazard assessments related to offshore infrastructure and slope stability (Bea, 1971; McAdoo et al., 2000; Kneller et al., 2016; Henery et al., 2018; Catuneanu; 2022). The Carboniferous succession exposed at Agua de la Peña Creek Creek in San Juan Province, Argentina, offers a rare opportunity to examine well-preserved MTDs formed during the Late Mississippian-Early Pennsylvanian along the paleo-western margin of Gondwana during the Late Paleozoic Ice Age. Environmental interpretations in this region remain ambiguous with competing hypotheses as to the extent and duration of glaciation. The Guandacol Formation amasses a thicknesses of up to 1000 meters, consists of a range of proglacial and postglacial facies, including distal turbidites, fine-grained shales, and MTDs containing exotic clasts derived from older units (Colombi et al., 2018; Valdez Buso et al., 2019). Although proglacial processes in the region remain relatively understudied, the Agua de la Peña

Creek locality has received increasing attention in recent years, with several studies documenting deposits preserved within the creek (Sobiesiak et al., 2016; Sobiesiak et al., 2017; Colombi et al., 2018, 2025; Valdez Buso et al., 2019; Allen et al., 2022; Spalletti et al., 2023).

This research aims to enhance understanding of kinematics, composition, and surface interactions of an MTD within the study area in Ischigualasto Provincial Park, San Juan Province, Argentina (Figure 1). Data from high-resolution imagery and fieldwork provide valuable insight into MTD morphology and deformation. Specifically, this study seeks to contribute new perspectives on how mass transport systems redistribute sediment, evolve along their flow path, and investigates the occurrence of glacial signatures within the strata through four objectives.

1) ***Analyze the basal contact and deformities of the studied MTD.***
2) ***Conduct detailed analysis of broad kinematics and deformational change within the vertical profile of the studied MTD.***
3) ***Contribute a better understanding to how MTDs change laterally across their flow margin.***
4) ***Identify glacial signatures preserved within the studied MTD at Agua de la Peña Creek.***

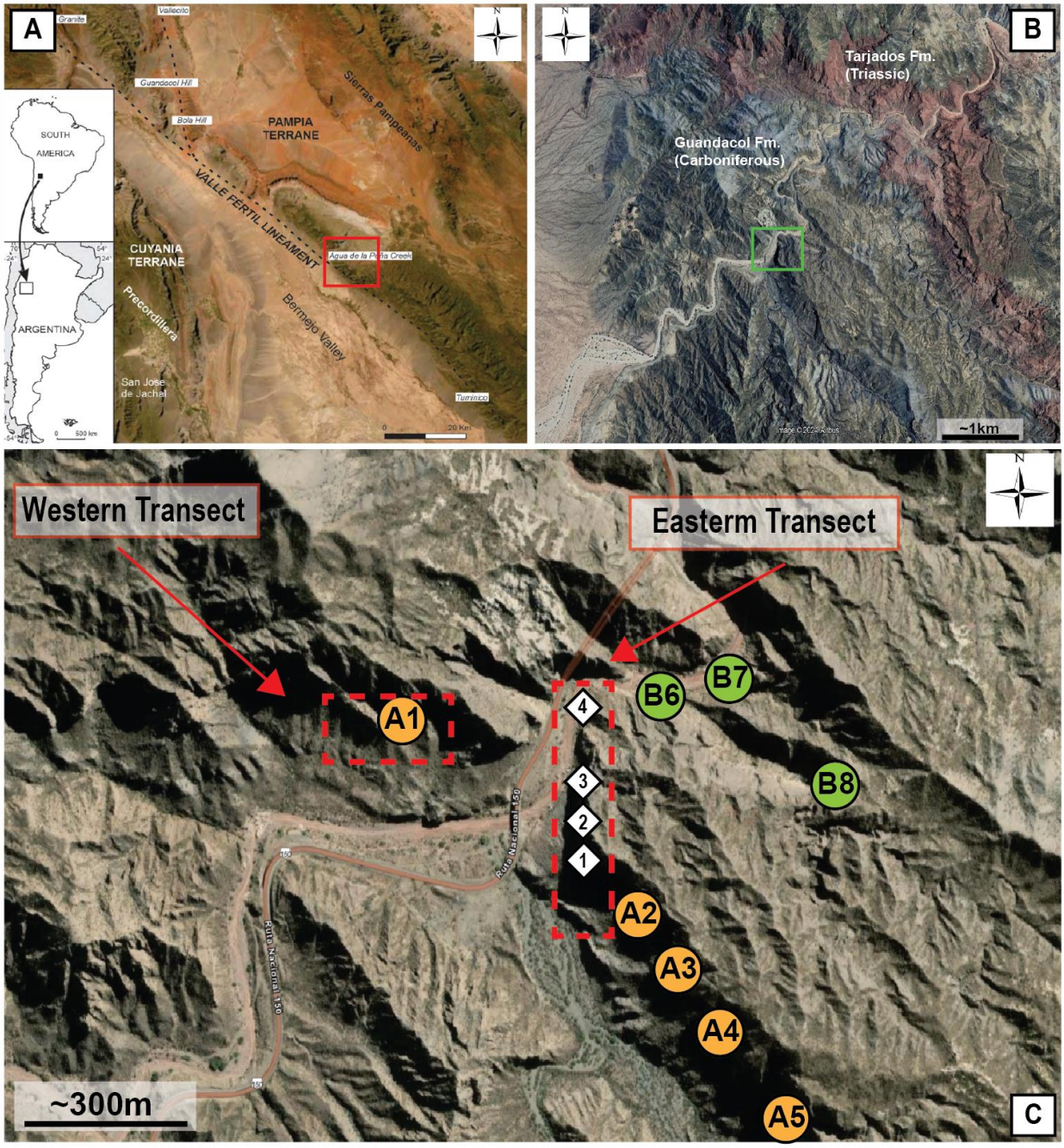

Figure 1: Imagery and maps showing the regional and local setting of the Agua de la Peña Creek study area. (A) The location of the Precordillera and the study site's proximity to the Valle Fértil Lineament Zone, where the Pampia and Cuyania terranes are sutured to form this structural feature. (B) A detailed view of the study area within the Valle Fértil range, including a transect of the studied mass transport deposit. Figure modified from Spalletti et al., (2023) (C) Overview of study location showing basal contact and vertical profile transects with stratigraphic section locations (white). Southern most stratigraphic column GPS Coordinates (30° 8'58.53"S, 68° 2'3.29"W). Northern most stratigraphic column (Section 4), GPS Coordinates (30° 8'48.18"S, 68° 2'2.08"W). Additionally, locations of photos observing lateral/oblique changes across the MTD. Points (A1 -A5) represent broad change locations for block measurements in *Table 1*. Points (B6-B8) are the locations for localized deformational change.

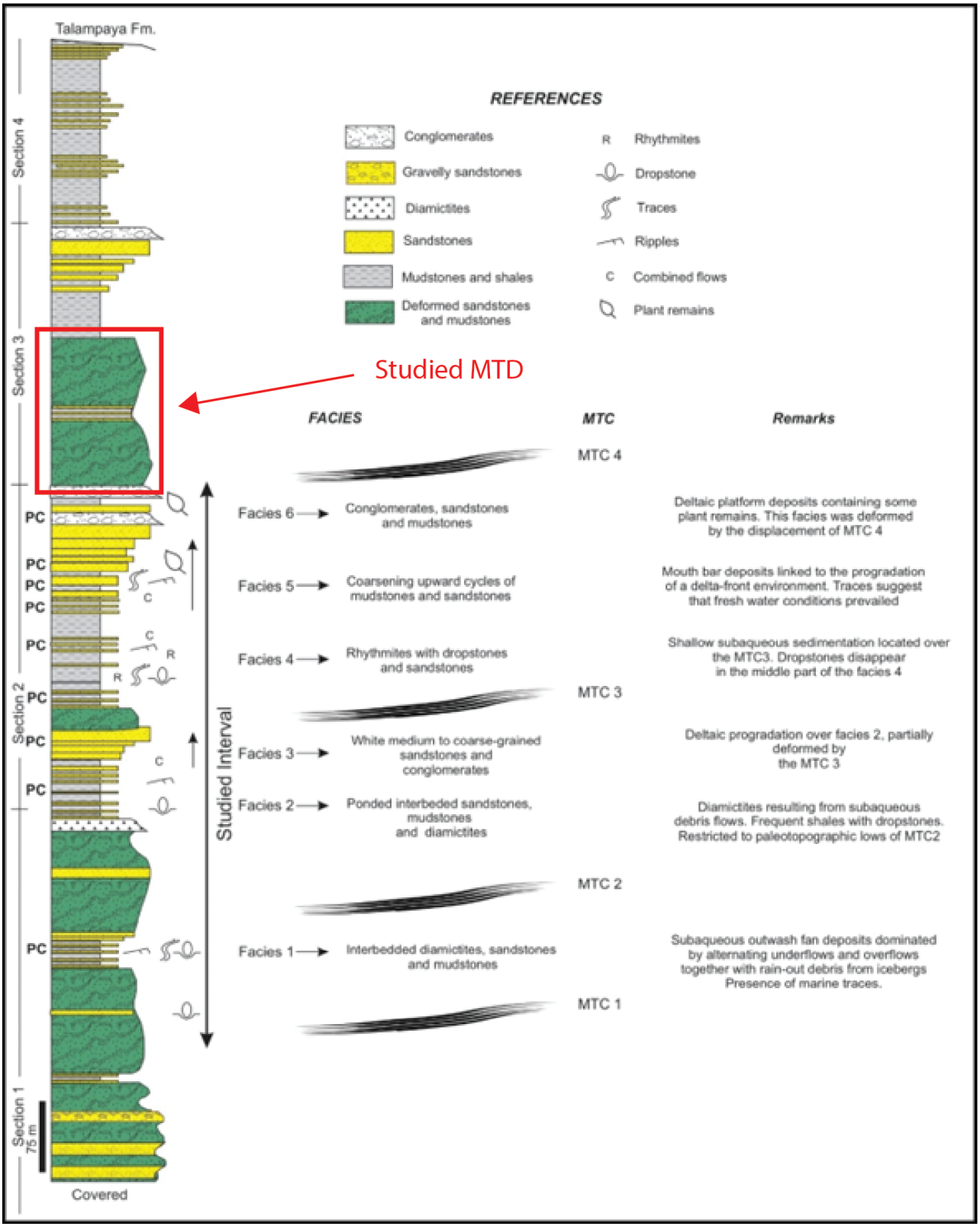

Figure 2: Constructed stratigraphic column for Guandacol Fm present within Agua de la Peña Creek. Notice the thickness of the formation and the alternation between rhythmite sequencing and MTD intervals. Figure taken from Colombi et al., (2025).

1.1.Mass Transport Process

Shifting stages in glaciation pose some of the most difficult sedimentary environments to interpret within continental basins. Complexity increases particularly when glaciers terminate in marine environments, where a diverse range of depositional characteristics can develop (cf. Dowdeswell et al., 2016). Within these regions, several factors influence sediment deposition: changing climatic conditions, glacial dynamics, regional sea level changes, changing sedimentation rates, glacial isostatic adjustment (subsidence/rebound/world sea level compensation), and tectonism (Posarnentier & Allen, 1999; Whitehouse, 2018; Isbell et al., 2021, Catuneanu, 2022; Vesely et al., 2024; Colombi et al., 2025). The origin of MTDs is considered a complicated issue, often driven by one or a combination of these factors. Mass transport involves the reworking of large volumes of material down basin slopes. Unconsolidated and water-saturated sediment deposited along sloped margins, achieves failure and is redistributed into deep-water settings (Dott, 1963; Ogata et al., 2012; Sobiesiak et al., 2018; Rodrigues et al., 2020; Spalletti et al., 2023) as MTDs or Mass transport Complexes (MTC). These deposits may achieve failure from a variety of different processes that include over-sedimentation, glacial retreat/advance, tectonism (seismic activity), changes in eustacy, degree of water saturation, and more (Benns & Evans, 2010; Vesely et al., 2018; Catuneanu, 2022). Each process yields a different response to sediment failure and creates different ways in which the material is deposited.

MTDs show an evolution of sedimentation through various processes and include transformations, starting with creep, followed by sliding, slumping, debris flows, and eventually density flows (Figure 3; Posamentier & Martinsen, 2011; Ogata et al., 2012; Ogata et al., 2014; Buso et al., 2019). As material is resedimented, it often transitions from more consolidated, less

deformed sediment packages to highly deformed and homogenized successions over longer transport distances and often evolves into debris flows and turbidity currents down flow as the MTDs disaggregate (Mutti et al., 2006; Ogata et al., 2012; Fallgatter et al., 2017; Rodrigues et al., 2020). This progression enables a flow initially classified as elastic (such as sliding) to gradually evolve into more Newtonian behavior (like density flows) as it continues to evolve over extended distances of transport (Fig. 3; Nemec, 1990; Mulder & Alexander, 2001; Mutti et al., 2006; Ogata et al., 2014). The arrangement of different deformational structures and overall characteristics of the deposits makes them unique in understanding deep-water sedimentation.

Another type of deep-water deposit, turbidites, are closely associated with MTD deposits. Turbidites are particle-composed density underflows deposited in shallow-deep water environments due to fluid turbulence (Bagnold 1962; Bouma 1962; Kneller, 1995; Mulder & Alexander, 2001; Meiburg & Kneller, 2010; Talling et al., 2012). Turbulence between sediment grains is created by the forward motion of material along a basal bounding surface. The motion of turbidites is then driven by gravity and the density differences between the sediment-laden fluid flows and the ambient water into which they flow (Hampton, 1972; Meiburg & Kneller, 2010; Talling et al., 2012; Fallgatter et al., 2017). Much like MTDs, turbidites are usually deposited into deep-water environments. Their deposition can take on a variety of different sedimentary structures and features depending on flow characteristics. Erosive, channelized flows can be deposited in submarine canyons and exhibit more ribbon-shaped deposits while extensive, graded sheet-like deposits create submarine fans and cover the proximal basin plains (Walker, 1978; Posamentier & Walker, 2006; Meiburg & Kneller, 2010). Where present, in deep-water environments, MTDs may provide an irregular topography for turbidites to accumulate as ponded deposits.

Intense internal and external deformation may cause extensive topographic relief along the upper surface of MTDs (Badalini et al., 2000; Armitage et al., 2009). Within this topography, turbidity flows may become restricted and/or ponded within the hummocky relief on the tops of these deposits. Turbidites fill these mini-basins and often display both onlap and downlap stratal relationships onto the underlying surface (Greene et al., 2006; Meiburg, E., & Kneller, B. 2010). When analyzing MTDs, turbidite deposits become relevant through the incorporation of underlying turbidite sediments into the mass transport flow. Turbidites underlie a majority of the basal surface for each of these events. The kinematic force related to mass movement causes the underlying substrate to deform and/or erode as it becomes incorporated into the flow. Incorporation of substrate can be manifested by different processes and is displayed through composition differences within the lower units of mass transport (Alves, 2015; Sobiesiak et al., 2018; Rodrigues et al., 2020). Therefore, turbidite sequences and ponded intervals play an important role in shaping the final composition within the lower units of mass transport deposits.

Flow Structure

Typically, the matrix component of an MTD displays elevated degrees of deformation compared to the solid material being rafted as coherent blocks from failure sites. The matrix accounts for most of the volume within some MTDs and represents a combination of several components including source material, incorporated basal substrate sediment, and material from lateral flow margins (Bull et al., 2009; Ogata et al., 2012; Rodrigues et al., 2020). Therefore, there are two major deformational members contained in these deposits. The least deformed material is composed of coherent blocks that can maintain original structure/bedding. In this work the **blocks** can be defined as undeformed **bodies** being larger than boulders in size (>4.1 m) and composed of sand or gravel (Varnes, 1978; Bull et al., 2009; Ogata et al., 2014; Alves,

2015; Sobiesiak et al., 2018). They are large volumes of undeformed to moderately deformed sediments generated in submarine environments and are transported by sediment gravity processes (Borgomano, 2000; Emmerich et al., 2005; Kvalstad et al., 2005; Alves, 2015). Blocks can be easily identified within outcrops due to the differences in lithology from the surrounding substrate and they are in discordant contact with surrounding matrix and are often internally coherent and stratified or slightly deformed (Sobiesiak et al., 2016). In contrast, the matrix is the most deformed material seen within flow deposits and consists of mixtures of sand, silt, clay, and potentially gravel. Often the matrix would be classified as a diamict through a variety of grain sizes and lack of depositional structure. Mass movements create a scale of matrix compositions and deformation as they evolve downslope through mixing, amalgamation, and alteration of original beds and associated sedimentary structures. The degree of deformation seen within the matrix can be referred to as a process of homogenization (Farrell, 1984; Thorton, 1986; Rodrigues et al., 2020). Lithified material with little alteration is considered to be unhomogenized (blocks or rafts), whereas disaggregated source material creates a diamict without any original structure and is referred to as homogenized (matrix; cf. Rodrigues et al., 2020). However, the degree of homogenization is rarely constant. Deformation of the protolith (original undeformed sedimentary material) increases with transport distance for several reasons: 1) The material has more interaction with seafloor topography, 2) the flow experiences more kinetic energy farther downslope, 3) there is an increased incorporation of substrate material incorporated into flow from lateral and basal margins, 4) increased water content due to the mixing of sea water into flow. Therefore, the degree of homogenization increases downslope from the failure escarpment through means of flow interaction and transformation (Ogata et al., 2014; Buso et al., 2019; Rodrigues et al., 2020).

Deformation Styles

Soft-sediment deformation in mass transport is structurally complex. In MTDs, overall deformation typically involves extension at the head of the deposit, transitioning to compression near the toe of the flow (Hansen, 1971; Farrell, 1984; Martinsen & Bakken, 1990; Alsop & Marco, 2012). However, extension and compression can occur locally anywhere within the flow. Both deformation types occur within plastic and brittle deformational regimes. Extensional deformation occurs when material is stretched in the direction of flow, driven by stress along the σ3 axis (Dykstra et al., 2011; Sobeisiak et al., 2019). The long axis of the extensionally deformed material often serves as a useful flow direction indicator. Plastic extensional deformation is commonly observed in boudins, which are sand bodies of varying size that are deformed during transport. Their elongation in one direction serves as an indicator of extensional stress (Sobiesiak et al., 2016). Brittle extensional deformation often occurs post-depositionally through fault settling. Normal faulting develops when the flow settles and extensional stress occurs due to weight distribution over the basal substrate and expulsion of water through the saturated material (Jamil et al., 2020; Oyanyan et al., 2020; Rodrigues et al., 2020; Alsop et al., 2024).

Compressional deformation involves stress along the σ1 and σ3 directions, leading to strain called simple shear (Dykstra et al., 2011). This stress, often associated with basal sliding, transport deceleration, and flow interaction, allows compressional features to form. Plastically deformed compressional features include folds, and secondary fabrics (Strachan, 2008; Rodrigues et al., 2020), while brittle compressional deformation usually develops during flow deposition, forming shear zones and thrust faults both within the MTD body and in the down flow terminal zone. These shear planes result from stress acting in different directions due to fluid and basal substrate interactions (Posarnentier & Allen, 1999; Strachan, 2008; Alves, 2015;

Sobiesiak et al., 2018). The degree of deformation varies both vertically and horizontally within MTDs (Ogata et al., 2012; Ogata et al., 2014; Sobiesiak et al., 2016; Rodrigues et al., 2020). This study aims to explore these deformational changes to improve the understanding of flow kinematics, stratal disruption, and the protolith source(s), which can all assist in interpreting the paleoenvironment during deposition and to understand the kinematics of a MTD flow.

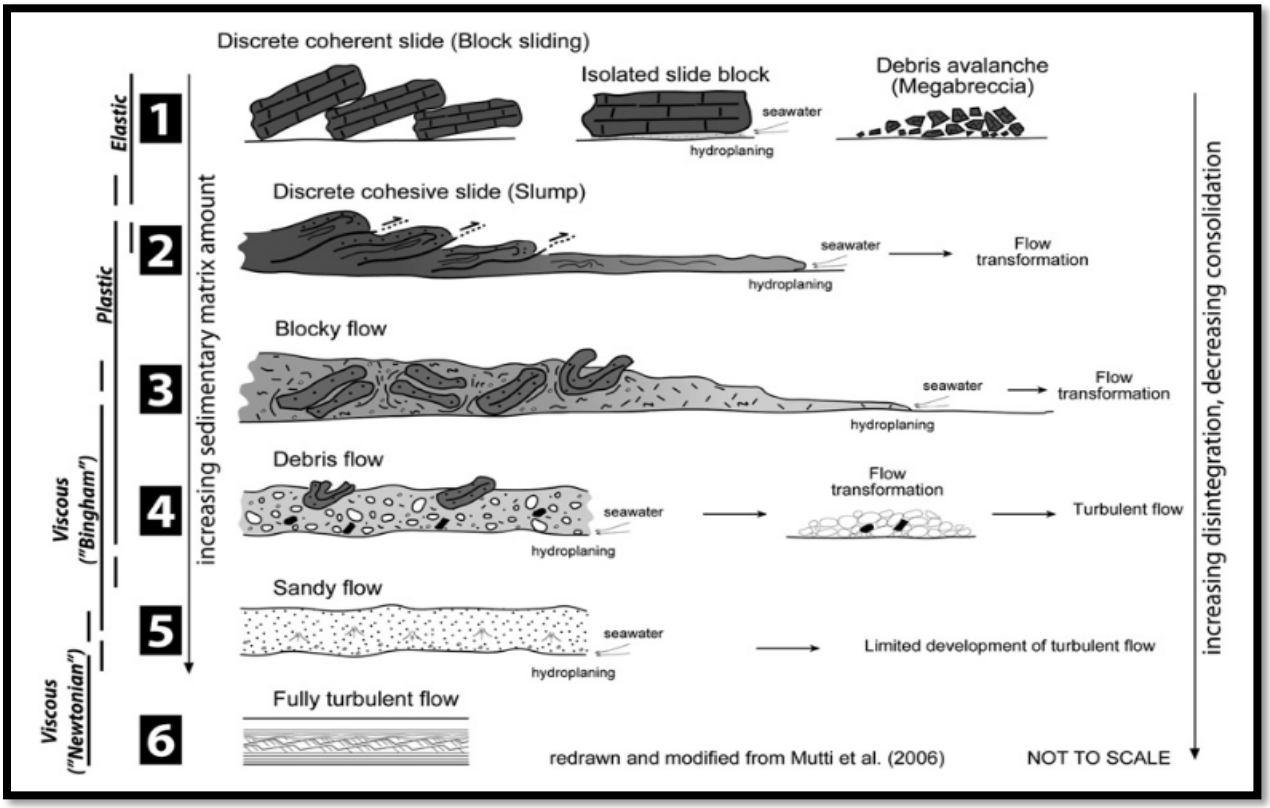

Figure 3: Figure depicting dynamic flow evolution of mass transport showing how increasing disaggregation/homogenization creates different types of flows (Elastic – Newtonian). Deformation evolves from sliding blocks to turbulent flows based on the composition and transport distance of material. Originally from Mutti et al., (2006) modified by Ogata et al., (2014).

1.2.The Late Paleozoic Ice Age

From the Late Devonian to Late Permian (372 Ma to 254 Ma) glacial advance and retreat cycles were associated with a global icehouse interval referred to as the Late Paleozoic Ice Age (LPIA). The LPIA is considered to be one of the most important glacial episodes recording the

only complete transition of icehouse-to-greenhouse conditions during a time when complex, terrestrial fauna and flora activity existed on Earth (Crowell & Frakes, 1970; Frakes et al., 1992; Eyles, 1993; Gastaldo et al., 1996; Isbell et al., 2003, 2008, 2012, 2021; Montañez et al., 2007; Fielding et al., 2008a, 2008b; Montañez & Poulsen, 2013; Fedorchuk et al., 2010; Rosa & Isbell, 2021). Therefore, studying this time interval offers comparison to the modern Cenozoic Ice Age and its potential termination due to anthropogenic climate change. During greenhouse phases, global temperatures rise due to the contribution of higher pCO_2 in the atmosphere. The origin of icehouse phases is tied to complex, interrelated factors such as plate tectonics, Earth's orbital cycles, and changing abundance of greenhouse gasses in conjunction with rates of chemical weathering and the terrestrial vegetation-CO2 feedback (Grobe et al., 2012; Montañez et al., 2016; Wang & Du, 2020). Previous interpretations held that glaciation was synchronous across global depositional basins during the LPIA (Crowell & Frakes, 1970; Frakes et al., 1992; Eyles, 1993). A large ice sheet over southern Gondwana is hypothesized to have advanced and retreated with transitions between glacial and interglacial periods (Veevers & Powell, 1987; Frakes et al., 1992; Ziegler et al., 1997; Scotese, 1999; Starck et al., 2021). However, emerging views suggest LPIA glaciation may have been more asynchronous, occurring in different depositional basins at different times. Studies of high-latitude glaciation indicates that the LPIA had multiple ice centers lasting 1-8 million years, separated by non-glacial periods (Visser, 1997; López Gamundí, 1997; Isbell et al., 2003, 2008, 2012, 2021; Fielding et al., 2008a, 2008b; Gulbranson et al., 2010; Ives and Isbell, 2021; Rosa and Isbell, 2021). Continued collection of field evidence showing glacial indicators and paleo-ice flow directions within studied widely dispersed deposits, across multiple depositional basins, will contribute data to determining which model best fits LPIA glaciation. Additionally, subaqueous sediment gravity flow deposits are

commonly associated with glacial sedimentation near marine margins (e.g., Lawson, 1979a, 1981a, 1989; Evans, 2018). These deposits can form through a variety of mechanisms, including over-sedimentation along sloped glaciomarine margins or the collapse of active push moraines (Evans, 2018). Non-glacial sediment gravity flows, including mass transport (slides and slumps) occur where there are high sedimentation rates and unstable accumulations of unconsolidated and weakly consolidated sediments and sedimentary rocks (e.g., Pickering and Corregidor, 2005; Arnott, 2010; Catuneanu, 2022; Rotzien et al., 2022). Differentiating between subglacially derived diamictites and those generated by mass transport processes remains a key source of uncertainty in LPIA glaciation models. This challenge is increased when MTDs exhibit glacial signatures, making it difficult to distinguish primary glacial features from secondary reworking. Consequently, identifying and interpreting glacially influenced MTDs is critical for refining reconstructions of LPIA glacial dynamics and sedimentation. This study investigates a late Paleozoic sediment gravity flow succession exposed in the Sierra Valle Fertil along Agua de la Peña Creek in Ischigualasto Provincial Park, San Juan, Argentina that is considered to have been glacially influenced (Columbi et al., 2018, 2025; Valdez Busco et al., 2020; Allen et al., 2022).

2). Geologic Background

2.1. Stratigraphic Setting Paganzo Basin

The geologic setting of the Paganzo Basin is interpreted through different tectonic processes. Ramos (1988) suggested that it formed as a retro-arc foreland basin, while Fernández Seveso & Tankard (1995) propose it developed as a strike-slip basin. During basin formation, the western limits of the basin were defined by an ancient fold-thrust mountain belt called the Protoprecordillera. This structure consisted of Ordovician-aged sedimentary rock deposits and

served as an area with significant topographic relief within the region. Boundaries to the north and east are formed by Cambrian – Devonian granites and metamorphosed rocks that compose the Famatina Range and Sierras Pampeanas System (Limarino et al., 2002; Pauls, 2020; Spalletti et al., 2023). Additionally, the basin also experienced a series of uplift and thrusting events associated with the collision of Cuyanina and Chilenia terranes (Ramos, 1988; Spalletti et al., 2023). During the late Devonian – early Carboniferous, the accretion of the Chilenia terrane created large-scale shear zones through the collision of continental blocks (Ramos, 1988; Spalletti et al., 2023). These shear zones formed to dissipate stress associated with continental collision but experienced tectonic activity caused by continuous reactivation at different crustal levels through time (Spalletti et al., 2023). Relevant to the study area, one of these large-scale shear zones is referred to as the Valle Fértil Lineament/Megafracture (Spalletti et al., 2023). Located within the west central part of the Paganzo Basin, the structure occurs as a boundary between the Cuyania and Pampia terranes and serves as a structural component that shaped location, architecture, and geological processes within the region (Spalletti et al., 2023; Colombi et al., 2025). The Valle Fértille Lineament remained active for an extended period ranging from the early Paleozoic to the Cenozoic, but its importance during the late Paleozoic is understudied and often overlooked.

2.2. Glacial Development Paganzo Basin

LPIA glaciation covered vast areas of Gondwana, present today on multiple dispersed continental blocks. Associated glacial deposits span as far west as Bolivia and western Argentina while having an eastern margin as far in the opposite direction of Gondwana as Australia (López-Gamundí et al., 1997; Limarino et al., 2002, 2006, 2014; Isbell et al., 2003, 2012, 2021; Henry et al., 2008). Glaciation along the western margin of Gondwana can be divided into multiple glacial

and interglacial events that spanned the Late Devonian to Early Permian (López-Gamundí et al, 1994, 2021; Limarino et al., 2002, 2006, 2014; Isbell et al., 2003, 2012; Fielding et al., 2008a; Henery et al., 2008; Rosa & Isbell, 2021). The Paganzo Basin is interpreted to be glacially influenced during the Late Mississippian and Early Pennsylvanian within western Argentina (López-Gamundí, 1998; Limarino et al., 2002; Desjardins et al., 2009; López-Gamundí et al, 2021). There are multiple interpretations of how the Paganzo Basin was affected during this glacial interval. Some studies suggest ice caps formed atop elevated regions created by topographic relief. Evidence of incised paleovalleys throughout the basin support the potential for glaciation occurring on these topographic highs (Henery et al., 2008; Isbell et al., 2012; Limarino et al., 2014; Alonso-Muruaga et al., 2018; Malone et al., 2024). Glacial signatures within these deposits could be linked to regional glaciers sitting on areas of high relief (Isbell et al., 2012, Limarino et al., 2014; Moxness et al., 2018; Pauls et al., 2021; Malone (JE). et al., 2023; Malone (JR) et al., 2024).

Another approach proposes a broad glacial advance from the east over the eastern margin of the Paganzo Basin (cf. Sterren and Martínez, 1996; Aquino et al., 2014; Socha et al., 2014). The Olta-Malanzán paleovalley has drawn several different interpretations to glacial movement within the basin's eastern margin. Some studies suggest that valley glaciers on uplands or extensive ice sheets flowed westward through an outlet glacier that carved the paleovalley (Sterren & Martínez, 1996; Aquino et al., 2014; Socha et al., 2014; Valdez Busco et al., 2021). Others view the area as having limited/no trace of glacial activity within the region (Andreis et al., 1986; Moxness et al., 2018; Pauls et al., 2019, 2021). The collection or absence of glacial signatures during this current study will further test models of glaciation for the Paganzo Basin.

2.3. Geologic Background Agua de la Peña Creek

There are a variety of depositional environments associated with Gondwana's mid-Carboniferous glacial interval within the basins of western Argentina. Glacially influenced environments have been interpreted as terrestrial-lacustrine (Limarino & Gutierrez, 1990; Buatois & Mangano, 1995), morainal bank (Marenssi et al., 2005), glacimarine (González, C., 1982), and fjord settings (Dykstra et al., 2006; Isbell et al., 2012; Henery et al., 2014; Limarino et al., 2014; Alonso-Muruaga et al., 2018; Pauls et al., 2021; Malone (JE). et al., 2023). Within the Paganzo Basin, several stratigraphic intervals are characterized as fjord successions. These systems are known for their complex facies relationships, largely due to their deposition during major glacial episodes. These glacial events influence sea level fluctuations, leading to a series of paleovalleys carved on topographic highs within and surrounding the basin (e.g., Kneller et al., 2004; Dykstra et al., 2006; Henry et al., 2010A, 2010B; Aquino et al., 2014; Alonso-Muruaga et al., 2018; Valdez Buso et al., 2019). The steep valley walls of these paleovalleys created zones of unstable sediment accumulation. When slope failure occurred, poorly sorted sediments were redeposited as turbidites, debris flows, and forms of sliding/slumping (mass transport) within these environments (c.f. Van der Wateren, 1995; Huuse et al., 2012).

The interpreted paleovalley chosen for data collection is located near the mouth of Agua de la Peña Creek. The canyon is accessible through National Road 150 and is near the western entrance of Ischigualsto Provincial Park. Located on the border between San Juan and La Rioja provinces, the site is ~160 km northwest of the city of San Juan and ~140 km southeast of La Rioja. Regionally, the Paganzo Basin contains the Paganzo Group, which has been divided into distinct formations representing various time-related strata. In the western part of the basin, the group is separated into the Guandacol (Serpukhovian to Bashkirian), Tupe (Bashkirian to

Moscovian), and Patquí (late Pennsylvanian to Cisuralian) formations (Gulbranson et al., 2010; Limarino et al., 2014; Pauls, 2020; Colombi et al., 2025). Basal Carboniferous strata of Agua de la Peña Creek is part of the Tuminico Formation; however, this formation is often lumped regionally as the Guandacol Formation (Cuerda et al., 1979; Colombi et al., 2018; Colombi et al., 2025). Regionally, the Guandacol Formation overlays metamorphic basement rock (amphibolite, garnet-gneiss, quartzite) that outcrop to the northeast of Agua de la Peña Creek (Schwarz, 1986). This succession amasses up to 1000 m thick, is characterized by sediment deposited from distal turbidites containing ice rafted debris and MTDs containing lonestones/outsized clasts. Present Agua de la Peña Creek is carved into Carboniferous strata along the western edge of the Ischigualasto and Caballo Anca Ranges. These ranges are situated along the Valle Fértil Lineament, where they underwent uplift with strata dipping in an easterly direction away from the lineament (Spalletti et al., 2023). Previous mapping of the area shows several iterations of mass transport deposits overlain by interstratified shale and sand turbidite successions (Figure 2). Lithofacies in the Agua de la Peña Creek region were first described by Schwarz (1986) and later contributed to by Valdez Buso et al. (2019) and Allen et al. (2022). While the specific MTD examined in this study has not been the focus of previous work, several studies have described mass-transport and turbidite deposits that occur stratigraphically above and below it. Colombi et al. (2018) and Valdez Buso et al. (2019) conducted broader-scale analyses of the stratigraphy within the creek, including the general intervals that encompass the studied MTD. At a more detailed scale, Sobiesiak et al. (2017) investigated structural and kinematic features of MTDs in the broader area; however, their study focused on different exposures and did not include the specific MTD investigated in this project. As such, this study includes new, detailed observations

of this particular mass gravity flow and seeks to contribute additional data to improve the understanding of these alternating sequences within Agua de la Peña Creek.

3). Methods

3.1. Sedimentology and Stratigraphic Methods

The studied mass transport deposit for this thesis is located in Ischigualasto Provincial Park, San Juan Province, Argentina (~30° 8'52.93"S, ~68° 2'0.77"W). Fieldwork was conducted in October 2023 and August 2024. Traditional stratigraphic sections were described, with data collected on unit thickness, lithology, sedimentary structures, deformational changes, contacts, and stratigraphic surfaces. Five stratigraphic sections were constructed to analyze basal interactions and vertical deformation within the studied outcrop. In addition, imagery analysis was employed to assess how these basal relationships and deformation patterns, along with block abundance and degree of deformation, vary obliquely across the mass-gravity flow. Poorly sorted lithologies were defined in accordance to Hambrey & Glasser (2003a), revised from Moncrieff's (1989) sediment classification scheme (Figure 4). Folding classifications were used in accordance to fold structures described by Benn & Evans (2010) (Figure 5). Each question posed by the objectives of this study utilizes stratigraphic sections for specific analyses. The following paragraphs detail the significance of sedimentology and stratigraphy in addressing each question.

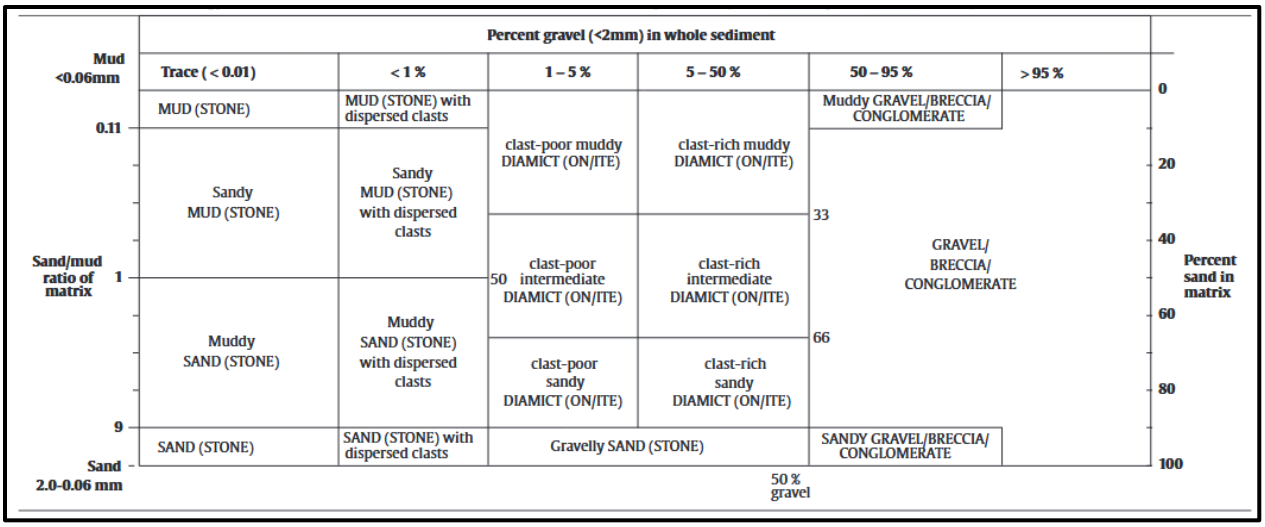

Figure 4: A non-genetic classification of poorly sorted sediment, adapted from Moncrieff (1989), is presented in this figure. It is used to categorize the various poorly sorted lithologies observed within the studied mass transport deposit.

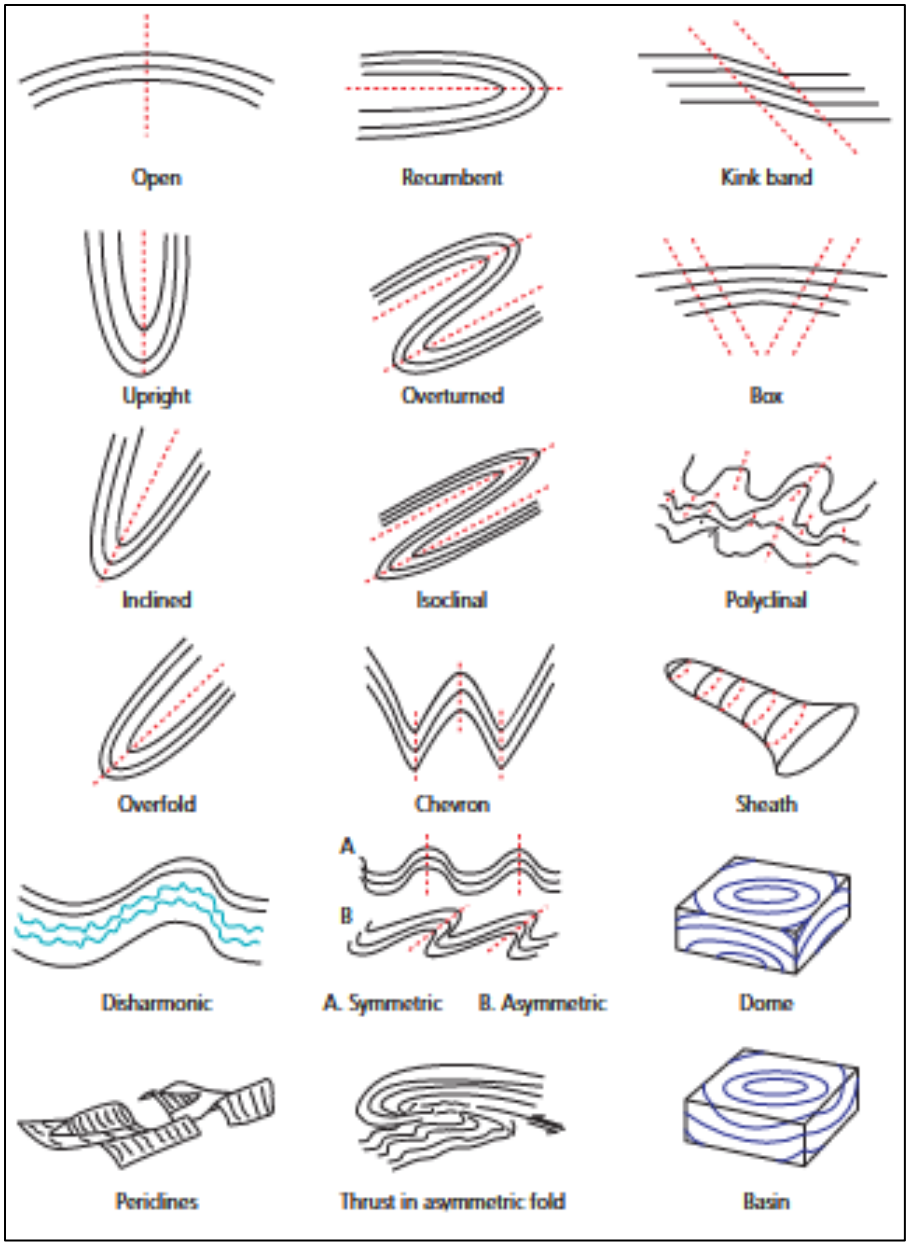

Figure 5: Figure taken from Benn & Evans (2010). Fold classification scheme used to determine different fold geometries within studied mass transport.

The studied mass transport succession along Agua de la Peña Creek exceeds 100 m in thickness throughout its exposure and is traceable for approximately 2.5 km. Due to the extensive nature of these deposits, this study partially focuses on a localized area for detailed sedimentological and deformational analyses (Figure 1, 6A-B). Stratigraphic and sedimentologic

logs were constructed using a Jacob staff equipped with an Abney Level and structural and paleocurrent orientations were made using a Brunton Compass. The compass was not adjusted for magnetic declination. After fieldwork, the magnetic declination was adjusted using the National Oceanic and Atmospheric Administration (NOAA) mobile magnetic declination calculator (https://www.ngdc.noaa.gov/geomag/calculators/mobile). Using a Jacobs Staff with an Abney level allowed for the direct measurement of the thickness of the dipping beds. Additionally, corrections for paleocurrent measurements and structural fabric were unfolded within each bedding plane using Allmendinger Stereonet 11. Fieldwork and data correction approach ensures accuracy in interpreting the sedimentological structural characteristics of the deposit in three ways:

(1) Stratigraphic sections were constructed to identify facies, changing sedimentologic conditions, transport directions, and where appropriate, kinematics of the sediment gravity flow during emplacement of the MTDs. A large stratigraphic section (Section 1) was constructed identifying the various facies and, where possible, paleocurrent flow directions. Turbidite deposits occur beneath the MTD. The contact between the turbidites and the base of the MTD were investigated by constructing several small stratigraphic sections which helped identify the occurrence of erosion/incision and deformation along the basal MTD surface.

(2) For the measured stratigraphic sections, standard sedimentologic and stratigraphic techniques were employed near the base of the MTD. For areas of steep slopes or vertical cliffs measurements and data were obtained, using a laser rangefinder (Laser Technology Inc. TruPulse 200X) to assess the thickness and drone (DJI Mavic 2 Pro with a 20 MP Hasselblad L1D-20c camera) images and high resolution photos (Canon EOS 5DSR - 50.6 MP Full Frame

CMOS Sensor; Canon RF 24-70mm F2.8L IS USM Lens, and Canon EF 100-400mm F/4.5-5.6L IS II USM lens) were used to identify visible sedimentary and deformational structures vertically and obliquely throughout the deposit. PTGui Pro (12.16) was used to stitch photo mosaics. Structural and kinematic indicators were annotated on various scales using Adobe Illustrator 2024 (28.7.1) and CorelDraw 2021.

(3) To investigate changes in the studied mass transport obliquely a table was created to document three varying characteristics of MTDs across the deposit. (1) Scaled photography was used to estimate block dimensions and flow heights. (2) The degree of block deformation was assessed on deformation features observed at multiple localities. A relative scale of deformation, ranging from low to high, was assigned by considering block coherency, the presence and extent of soft-sediment deformation, and the types of soft-sediment structures identified. This approach aligns with the scale provided by Rodrigues et al. (2021) investigating levels of flow homogenization. (3) Block abundance was estimated using a visual comparison chart allowing a block-to-matrix ratio to be established for each locality.

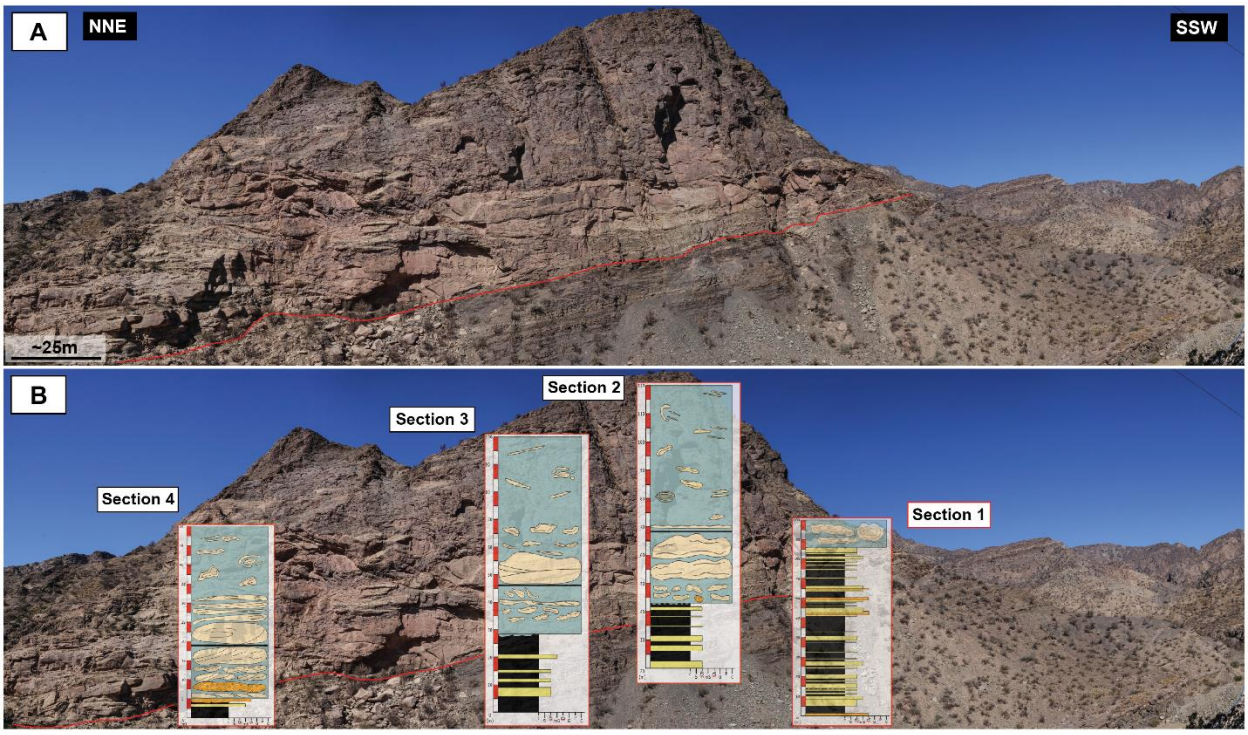

Figure 6: The outcrop provides an opportunity to observe vertical and basal deformation changes within the study area. Lithologic variations are documented using transparent stratigraphic sections (Fig. 8-11), positioned over each measurement area. GPS coordinates for the study section (30° 8'52.93"S, 68° 2'0.77"W). Basal contact of mass transport highlighted with red contact line.

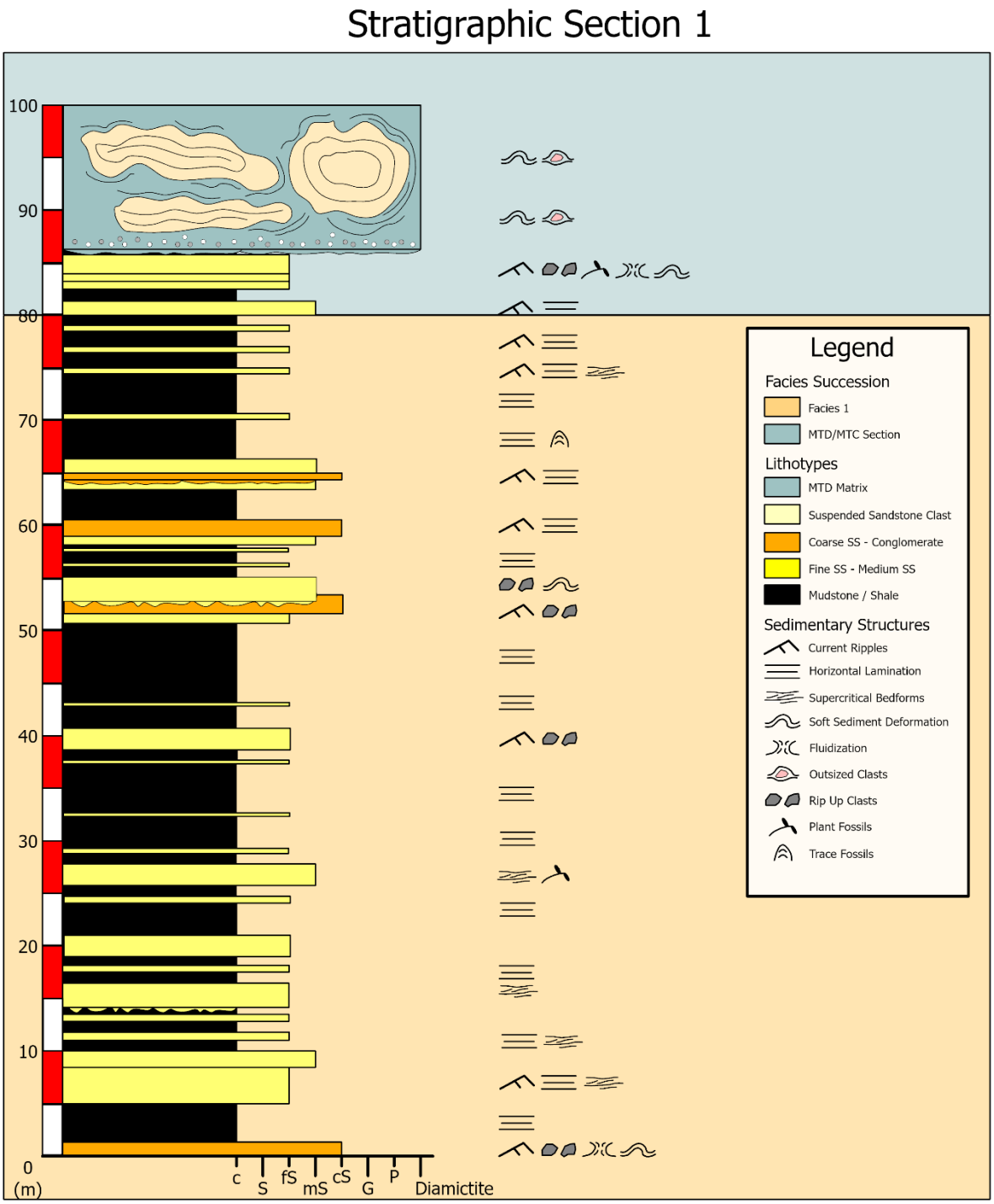

Figure 7: Sedimentologic log of Section 1. Farthest section to the SSW depicting facies succesion below the mass transport deposit. The exposure contains coarsening upaward succesions exposed beneath the mass transport deposit. Facies units extend ~85 m and mass transport succesion reaches ~100 m. Base of column begins in tributary south of outcrop at an elevation of 889 m (AMSL).

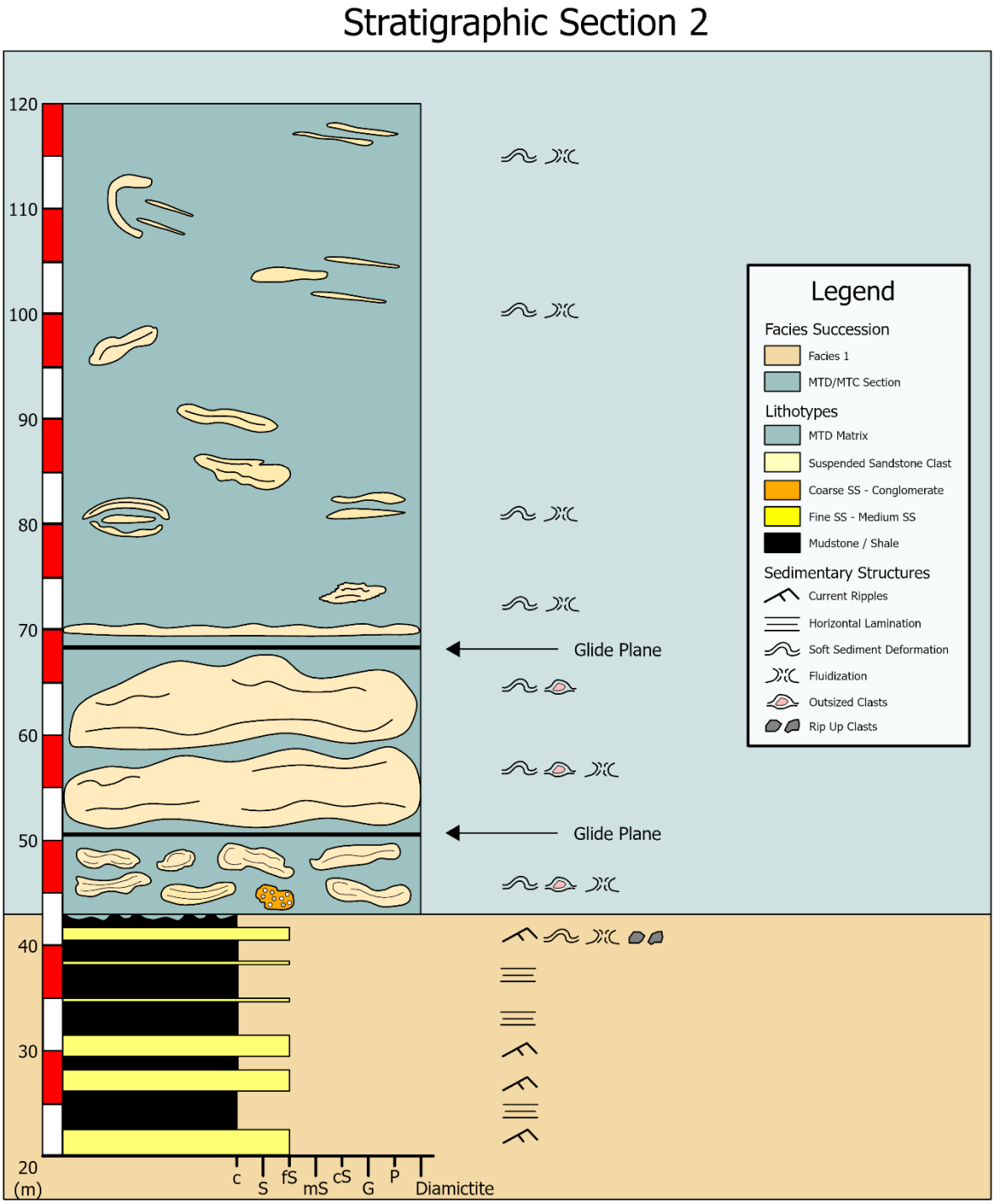

Figure 8: Sedimentologic log of Section 2 located 200 m to the NNE of Section 1. The section displays lithology changes within the thickness part of the MTD. The lower 20 m is covered by scree. The base of the section is the slope scree below Facies 1.

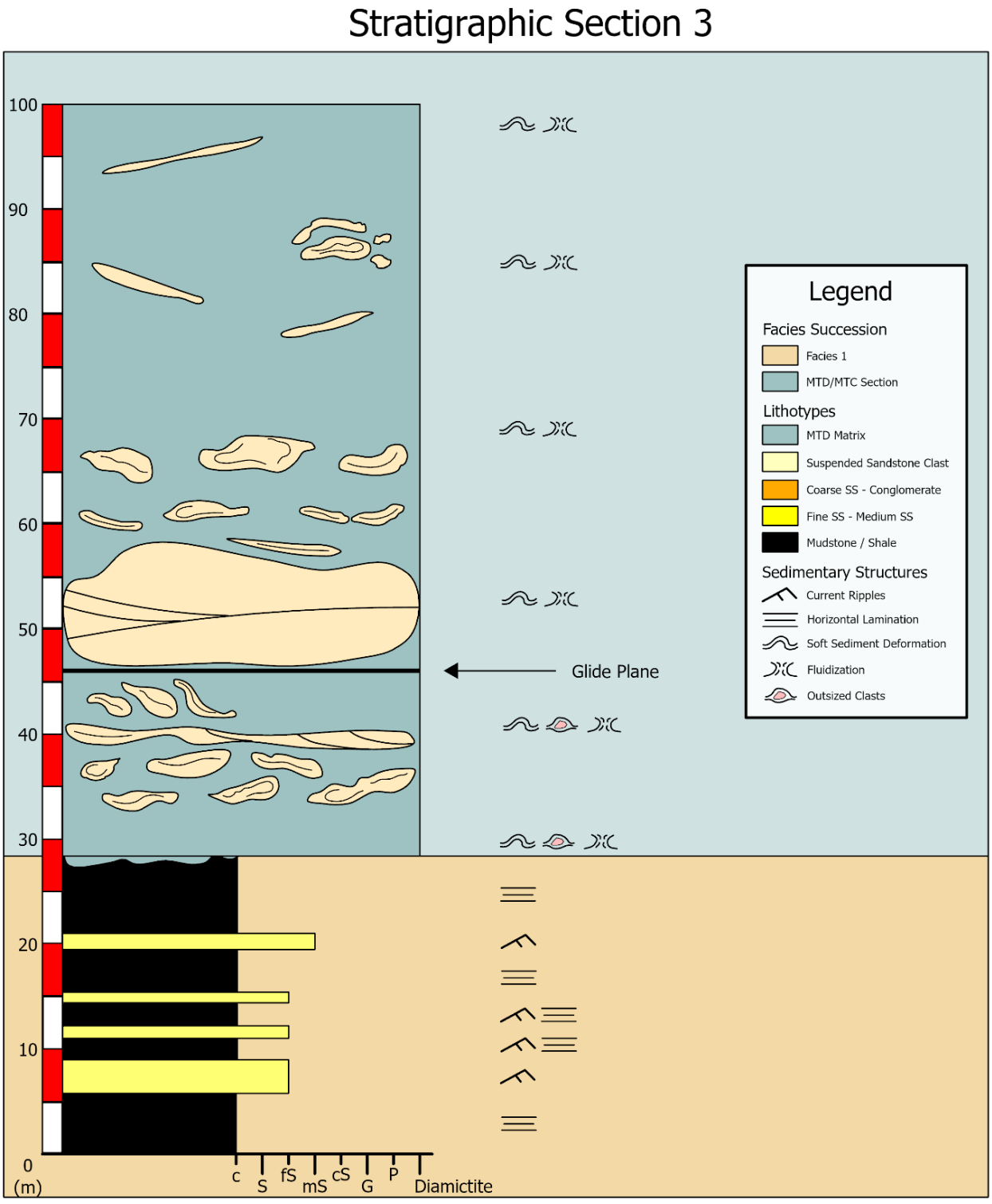

Figure 9: Sedimentological log of Section 3 located 135 m to the NNE of Section 1. Datum for section is the base of Agua de la Peña Creek.

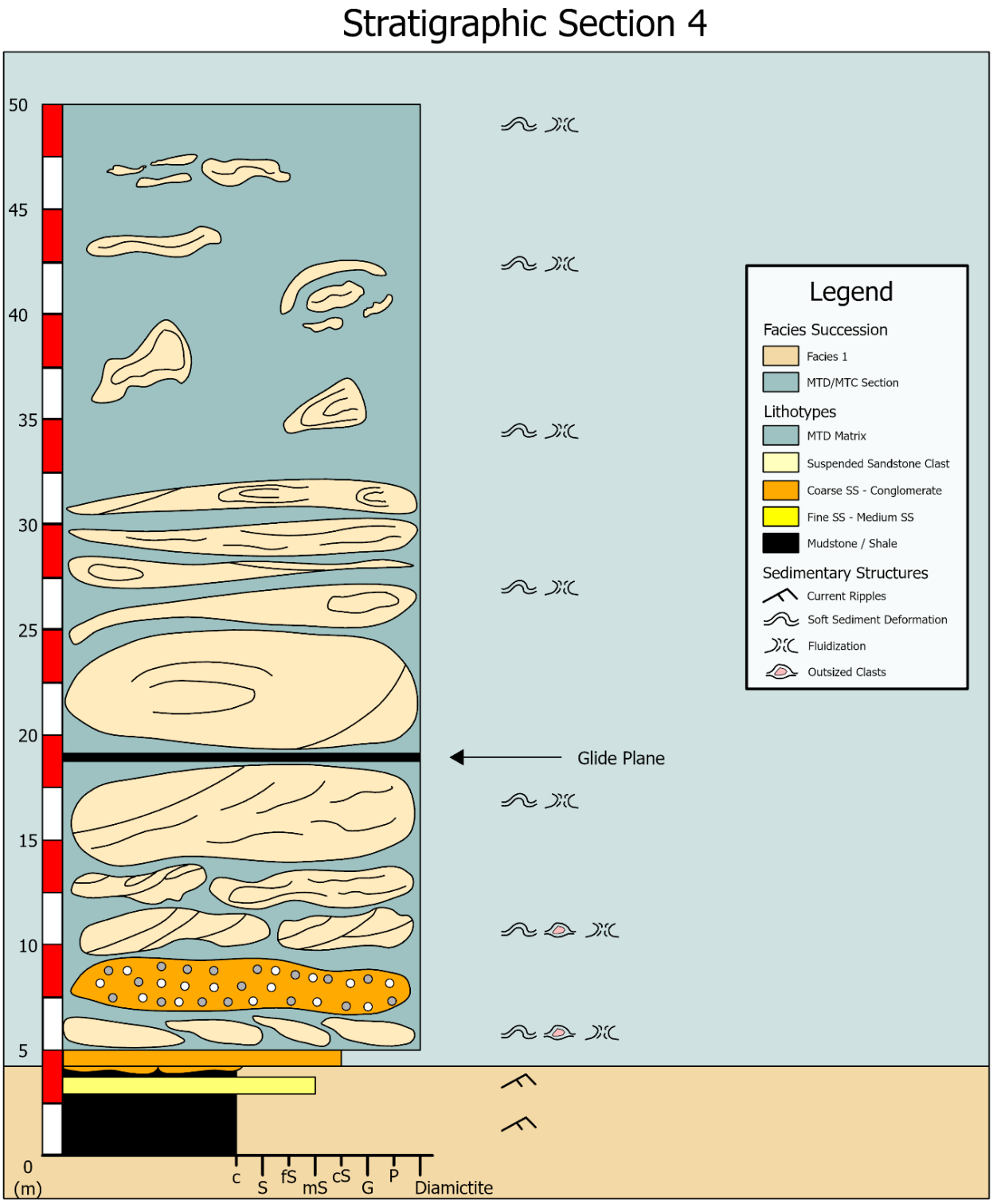

Figure 10: Sedimentology log of Section 4 located 210 m to the NNE of Section 1, the farthest section north describing lithology changes within mass transport succession. Cover and facies extend to ~ 5 m and mass transport succession reaches ~50 m.

3.2. Structural and kinematic indicators

Structures indicative of kinematic and deformational processes within the MTD include shearing, folding, faulting, boudinage, fluidization, fabric development around exotic clasts, and basal contact interactions. This section outlines each of these structures and provides examples of their expression and formation within the studied MTD. To constrain flow characteristics of the deposit, structural data on folds and thrust faulting was collected to identify flow characteristics within the MTD and adjacent strata. To obtain the paleo-slope and paleo-flow direction, measurements were employed to predict flow attitude and orientation resulting from deformation in slump structures (Woodcock, 1979; Strachan & Alsop, 2006; McNall, 2019). Measurements from two structural fabrics—fold hinges and the down-dip direction of thrust faulting—were collected to interpret flow characteristics at the basal surface. Flow direction through folding was calculated using Holdsworth (1939) and Alsop & Marco (2011, 2012) Fold Facing Direction (FFD) technique. Fold facing is the direction perpendicular to the fold hinge in which strata get younger across the axial plane. The trend of the hinge can be measured and rotated perpendicular to find flow direction from facing. These measurements provide crucial information about flow direction, kinematics, and mass transport sequencing.

Shearing

MTDs exhibit shear stress near the base of the flow within remobilized material due to gravitational and frictional forces. As a result, much of the strain is concentrated at or near the basal shear zone or basal contact (Figure 15; Middleton & Hampton, 1976; Ineson, 1985; Tripsanas et al., 2003; Cardona et al., 2016; Cardona et al., 2020). Variations in stress and

material properties at this contact lead to various styles of basal erosion and deformation along basal shear zones, as documented in (e.g., Sobiesiak et al., 2018; Cardona et al., 2020). Shear strain is also observed above the basal contact, though at a lower intensity. Higher in the deposit, shearing occurs around flow-entrained blocks and within the highly homogenized matrix that develops a fissile and foliated appearance (see Figure 12A; Ogata et al., 2012; Rodrigues, 2020) Additionally, two distinct types of shearing occur within soft sediment deformation: layer-parallel shearing (LPS) and layer-normal shearing (LNS)**.**

> **Layer-Parallel Shearing (LPS)** occurs when rock or sediment layers glide past one another along planes parallel to the flow direction. This process generates shear zones that exhibit minimal folding or tilting. LPS often develops at the base of the deposit due to differential compression between weaker and more competent layers (Alsop & Holdsworth, 1993, 2007).

> **Layer-Normal Shearing (LNS)** results from forces acting perpendicular to the flow direction. LNS structures, including folds, typically form in response to variations in flow acceleration, such as during flow surges or slackening. Vertical compression within the flow produces a range of deformation features, from thrusting to clast rotation (Alsop & Holdsworth, 2007).

Folding

Formed from compression, folding is prominent throughout the mass transport deposits (see Figure 12B, 13B; Clare et al., 2014; Jablonska et al., 2018; Rodrigues et al., 2021) Observations and measurements in the field focused on the base of the deposit, where folds occur in open configurations. Fold classification is determined by the nature of the fold hinge, the form

of the limbs, and the kinematic relationship between the fold and adjacent surfaces (Fleuty, 1964). Within shear zones, movement in one direction results in asymmetrical layer parallel shearing and stress, producing parallel cylindrical folds that range from gently-open upright to tightly-closed overturned recumbent forms. Additional folds, including recumbent, detached, thrust, and drag folds are prevalent throughout the base of the flow but often dissipate vertically upward in the succession.

Faulting

Both compressional and extensional faulting occurs within the flow deposits. Compressional faults typically develop as thrust faults, driven by block movement within the flow. Block thrusting occurs through two primary mechanisms: (1) matrix deflection induced by block rotation and (2) block compression resulting from collision and overriding (see Figure 12B; Bull et al., 2009; Ben & Evans, 2010; Evans, 2018). This displacement causes the upper layer to push over the lower one, creating reverse thrust faulting. These thrust faults can provide insight into the direction of flow during transport (Bull et al., 2009; Isbell et al., 2010; Alsop et al., 2016; Alsop et al., 2019). Following deposition, extensional forces generate normal faults through processes related to settling and accommodation. Normal faulting occurs as the saturated underlying surface gradually adjusts under the load or extension on the layer, resulting in offset. Faulting associated with this process can be observed at both macroscopic and microscopic scales and are seen within areas that behave more plastically (Gee et al., 2006; Bull et al., 2009; Rodrigues et al., 2020).

Boudins

Boudins display a wide range of sizes and deformation styles, varying from pebble-sized bodies to larger blocks. Their distribution and density fluctuate across different sections of the

mass transport deposit. Boudins form when a competent layer undergoes stretching or deformation while surrounded by a weaker matrix. This process produces extensional and compressional structures, collectively referred to as boudinage (see Figure 12C, 14A; Tripsanas et al., 2003; Alves, 2015; Sobiesiak et al., 2017; Buso et al., 2019; Rodrigues et al., 2020). Substrate blocks are no longer considered to be boudinage once completely removed and transported from the original source layer, unless a transported sedimentary body itself is being pulled apart. After detachment, the material is classified as either clasts, rafts, or blocks, which are size and composition dependent (Alves, 2015; Sobiesiak et al., 2016). Regions of boudinage dominated by extensional forces exhibit material that has been pulled apart often forms elongated, detached structures within a layer or lamination are referred to as “boudins.” Less competent beds that do not fracture but instead stretch under extension are characterized as "pinch-and-swell" structures (Ramsay and Huber 1983; Hölzel et al., 2006). Areas influenced by compressional stress may show localized extensional boudins/blocks with a variety of deformation features, including folding and more complex shapes (Ben & Evans, 2010; Evans, 2018). The degree of deformation also varies, with some areas exhibiting only minor deformation, while others display extensive deformation depending on the flow kinematics. These variations reflect localized differences in stress regimes, rheological contrasts within the deposit, and the intensity of shear during transport and emplacement. The observation of boudins/blocks can also serve as a basic indicator for direction of flow. Tail structures on extensionally deformed material indicate a long axis associated with flow direction (Figure 12C; Goscombe et al., 2004; Evans, 2016; Sobiesiak et al., 2016; Rodrigues et al., 2020).

Fluidization/Liquefaction

Various types of fluidization structures are present throughout the study area, occurring both during deposition (e.g., loading and injections) and post depositionally (e.g., dewatering features). Liquefaction occurs in subaqueous environments when sediment particles separate and become suspended in pore fluid (Broggs Jr., 2006). Grain weight is temporarily transferred to the pore fluid due to increased pore pressure. Injections are observed at multiple scales and within different lithologies (see Figure 13A; Boggs Jr., 2006; Owen & Moretti, 2011, Oyanyan, 2020). These features typically form due to the settling of a denser loading unit, where weight and density contrasts drive fluid escape within the underlying saturated material creating load and flame structures (Cooke & Johnson 1970; Allen, 1982; Lowe, 2006; Ogata et al., 2012). Additionally, numerous boudins and block-like structures are injected and cut by the surrounding matrix. Post depositional dewatering structures are observed as sheets and pipes in saturated portions of the deposit. These features arise when fluidized material settles after transport, causing water to escape due to elevated pore pressures induced by overlying sediment loads (Wentworth, 1966; Lowe & LoPiccolo, 1974; Lowe, 2006; Oyanyan, 2020). Dewatering features are frequently found within larger sandstone blocks of the mass transport deposit.

Exotic Clasts

Clasts within the studied mass transport deposit include both intrabasinal sandstone and extrabasinal granitoids, diorites, and gneisses clasts from basement sources. These clasts vary in size from pebbles to boulders, which are primarily subrounded to subangular. In certain areas, the presence of exotic clasts shapes the surrounding lithology through shearing deflection forming quarter and rotational structures (see Figure 11 A-B; Rodrigues et al., 2021; Fossen, 2016).

Basal Deformational Contact

Within MTDs, the basal contact or basal shear zone (BSZ), is localized deformation formed syndepositionally at the interface between the downslope-moving mass and the underlying substrate. This boundary commonly separates undeformed or less-deformed strata below from the overlying mass transported material and can occur as either a sharp, deformed, or gradational contact (Cardona et al., 2018; Fossen & Cavalcante, 2017). The composition of the BSZ may consist entirely of remobilized sediment from the overlying MTD or represent a mixture of gravity flow material and disrupted substrate. In some cases, the BSZ occurs as an erosional surface where the flow incises into the underlying strata, while in others it may function as a bypass surface, exhibiting minimal deformation due to limited flow-substrate interaction, possibly due to hydroplaning of the flow (Cardona et al., 2018; Sobiesiak et al., 2018). The morphology and kinematics of BSZs can vary widely, encompassing features such as free-slip conditions, hydroplaning, substrate liquefaction, and erosion (Figure 15, 16, 17A-B). These expressions are governed by multiple factors during transport, including pore-fluid pressure, basal friction, sediment viscosity, incorporation of water, and the mechanical properties of the substrate which can create a mosaic of effects across the BSZ. (Figure 15, Mohrig et al., 1998; Posamentier & Kolla, 2003; De Blasio et al., 2005; Alves, 2010; Cardona et al., 2018).

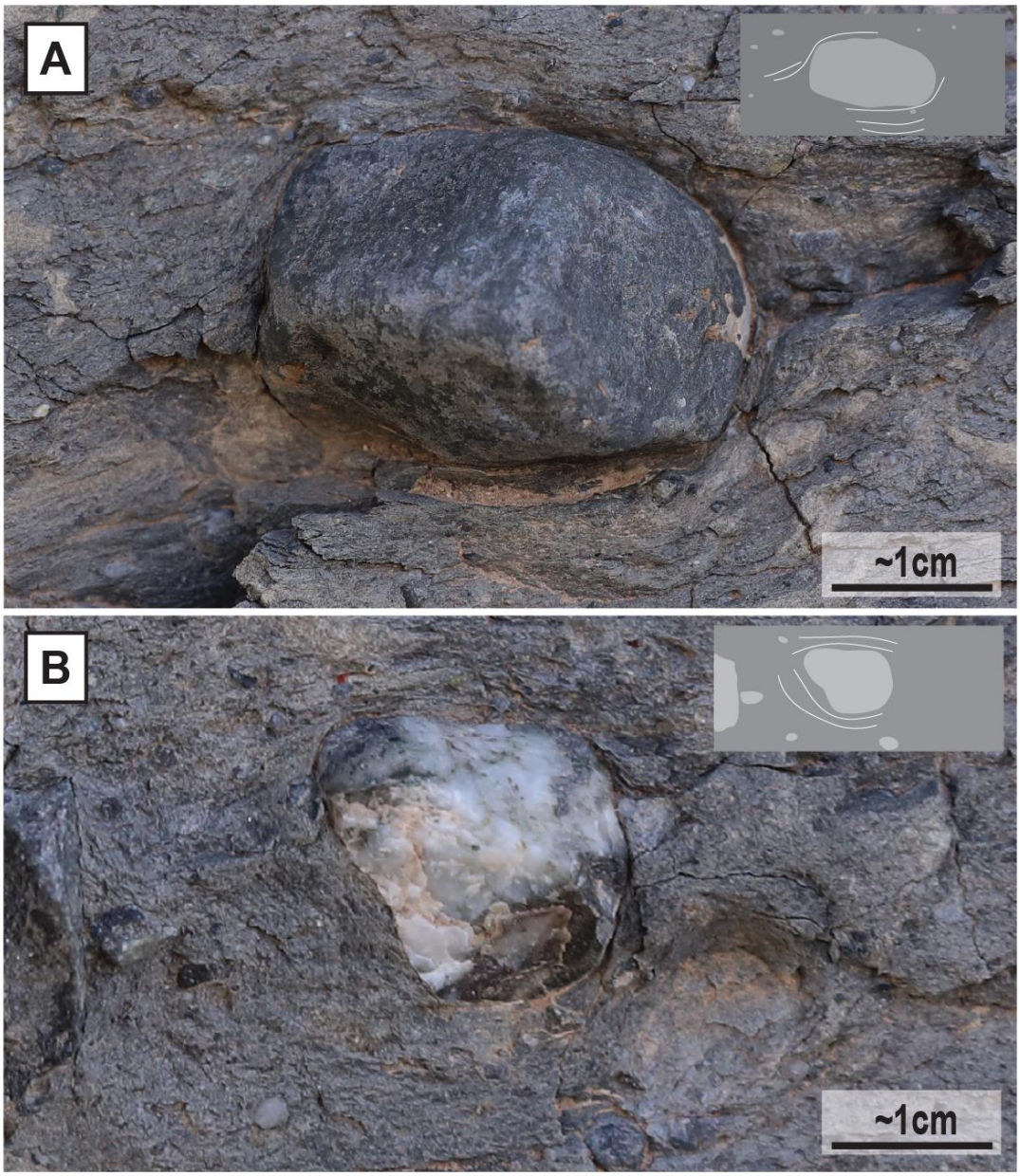

Figure 11: (A) Clast within matrix exhibiting quarter structures and pressure shadows created through LPS (Rodrigues et al., 2021). (B) Rotational deflection created around the boundary of an exotic clast.

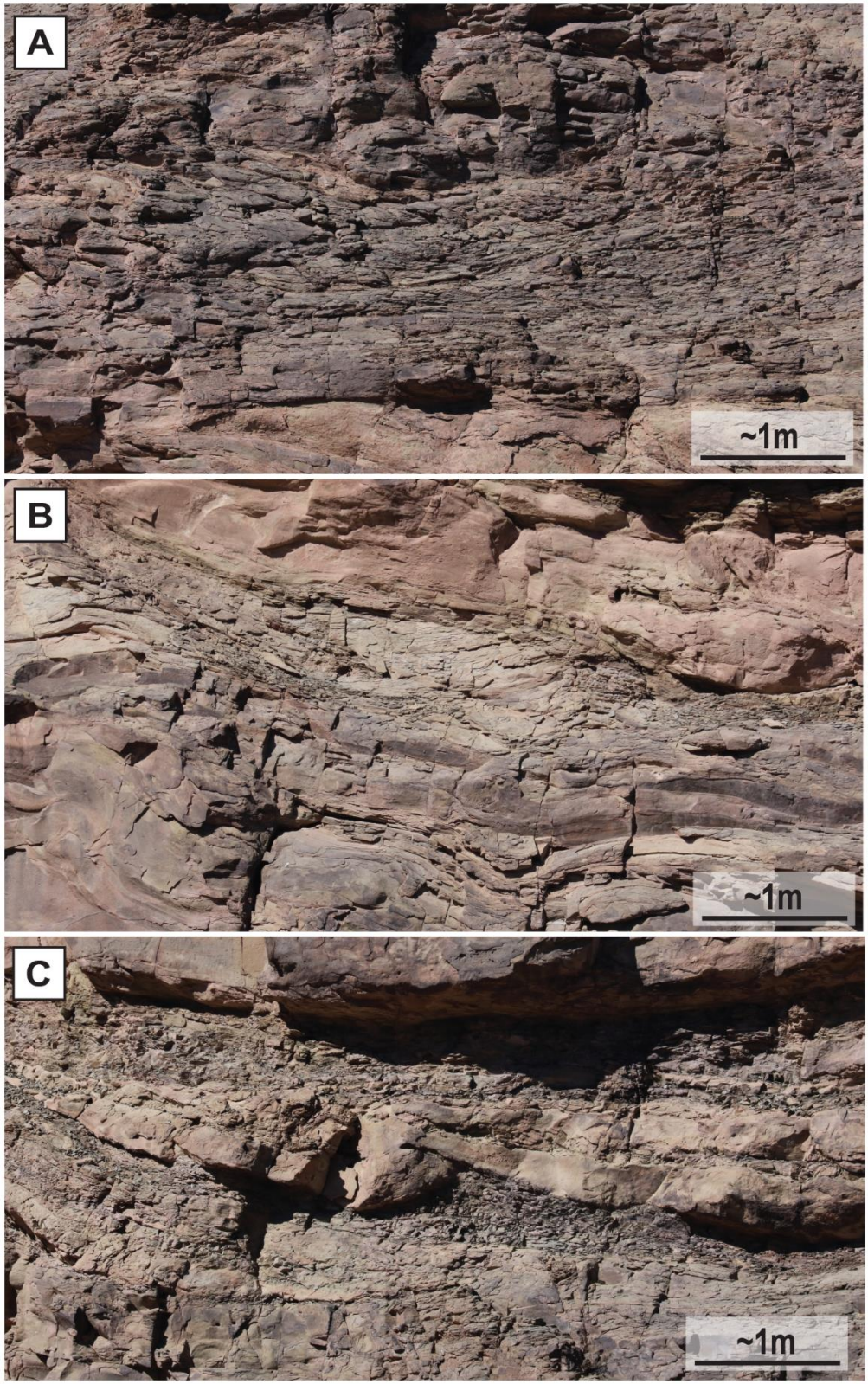

Figure 12: (A) Shear fabric developed within the matrix near the upper portion of the mass-transport deposit. **(**B) Shearing, thrust faulting, and open symmetrical folding are concentrated within a high-strain deformation zone. (C) Lateral thinning, separation, and extension of a sandstone bed resulting in boudinage structures.

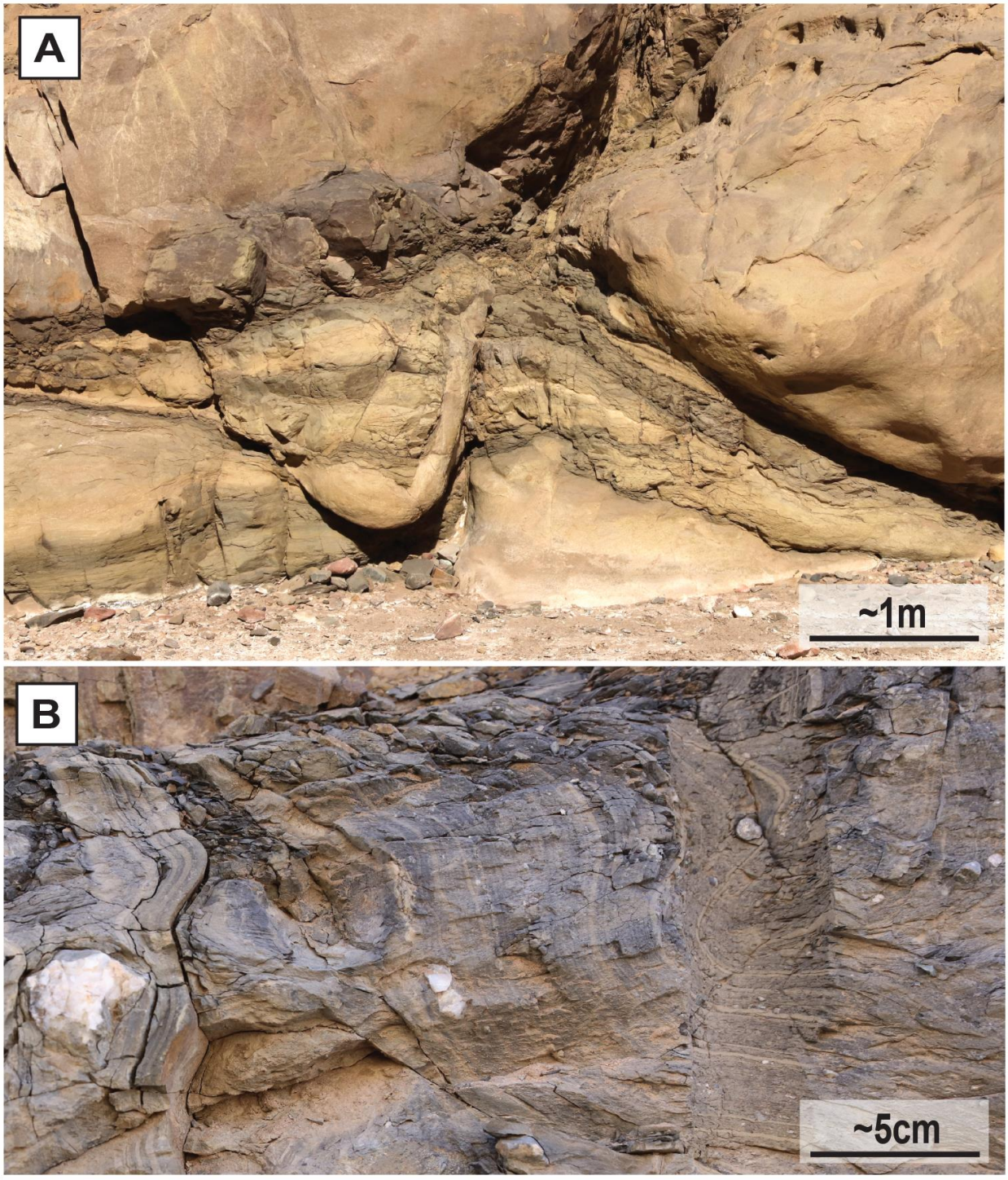

Figure 13: (A) Fluidized injection formed between block fragments above the basal contact of the mass-transport deposit MTD. (B) Disrupted asymmetrical folds surrounded by pebble-sized exotic clasts within the upper levels of the mass-transport deposit.

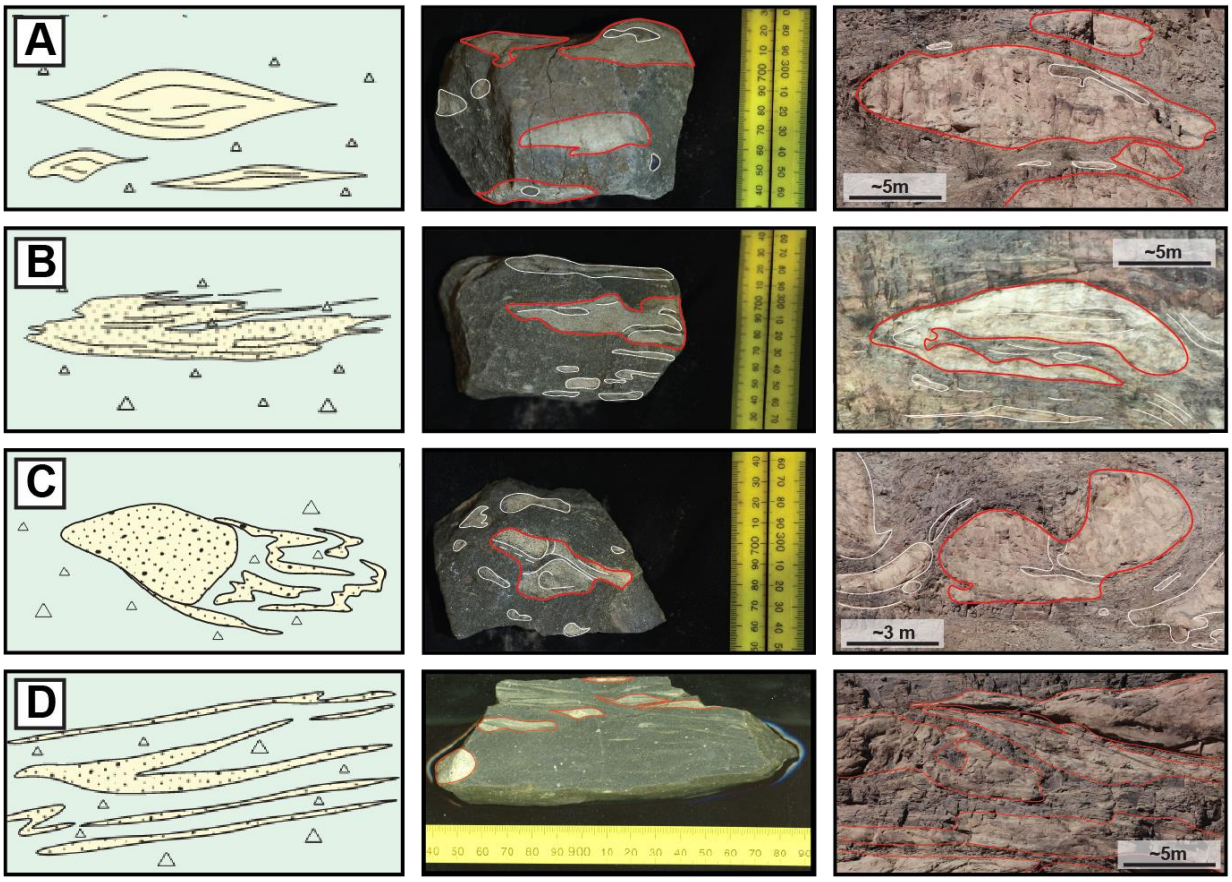

Figure 14: Soft-sediment deformation is observed at various scales within mass transport deposits. This figure illustrates how similar deformation patterns manifest across both hand-sample and outcrop scales. (A) Extensional deformation resulting in lateral pinching. (B) Compressional deformation producing a sheared lens-like structure. (C) Interaction of compression and extensional shearing material from the backs of sand bodies. (D) Compression and extension fragmenting a sand body into distinct elongated streaks. Figure adapted from Evans (2018).

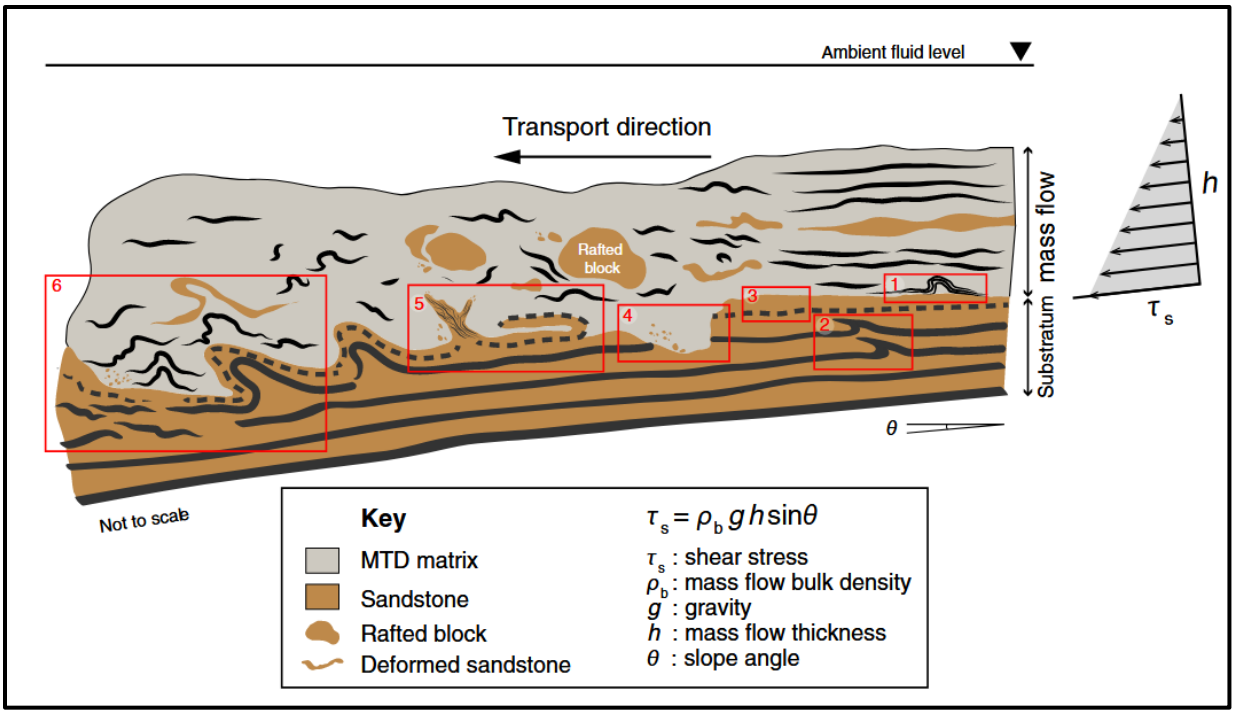

Figure 15: Figure shows how deformation within transport and specifically the basal surface changes significantly with distance in transport direction. (1) Indicates deformation above the basal contact in the mass flow protolith. (2) Deformation penetrating substrate and deforming underlying material (3) Little to no evidence of deformation (free slip). (4) Zone of erosion ripping blocked substrate into flow protolith. (5) Substrate is liquified below flow deposit causing fluidization of substrate. (6) Remobilized mass flow and substrate inclusions. Red rectangles correspond to the thickness of basal deformation. Figure taken from Cardona et al., (2020).

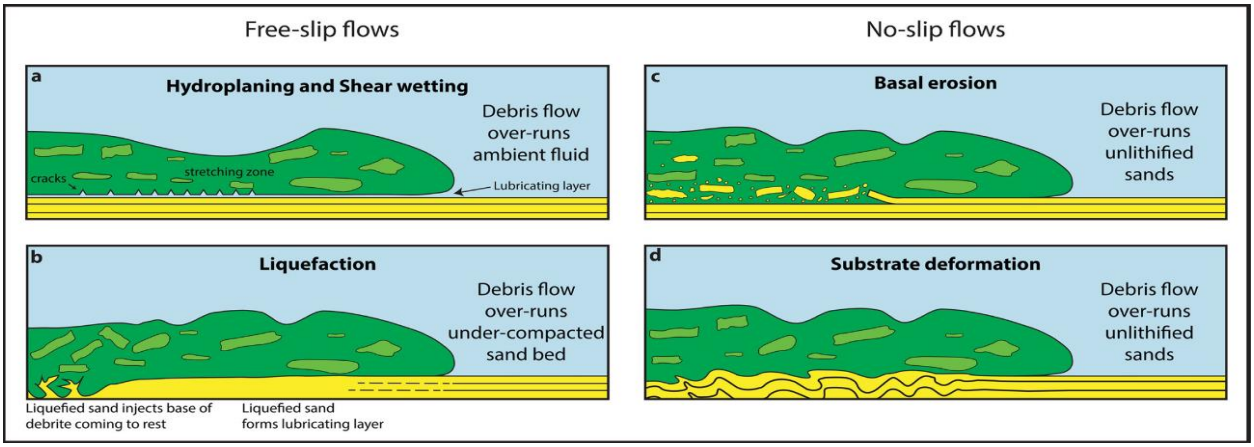

Figure 16: Diagrams illustrating various types of basal interactions and subsurface deformations that occur during mass transport deposition. The nature of the interaction at the basal surface is influenced by several factors, including the composition and structure of the underlying surface, the degree of water saturation in the substrate, flow dynamics, and other geological characteristics. Figure taken from Sobiesiak et al. (2018).

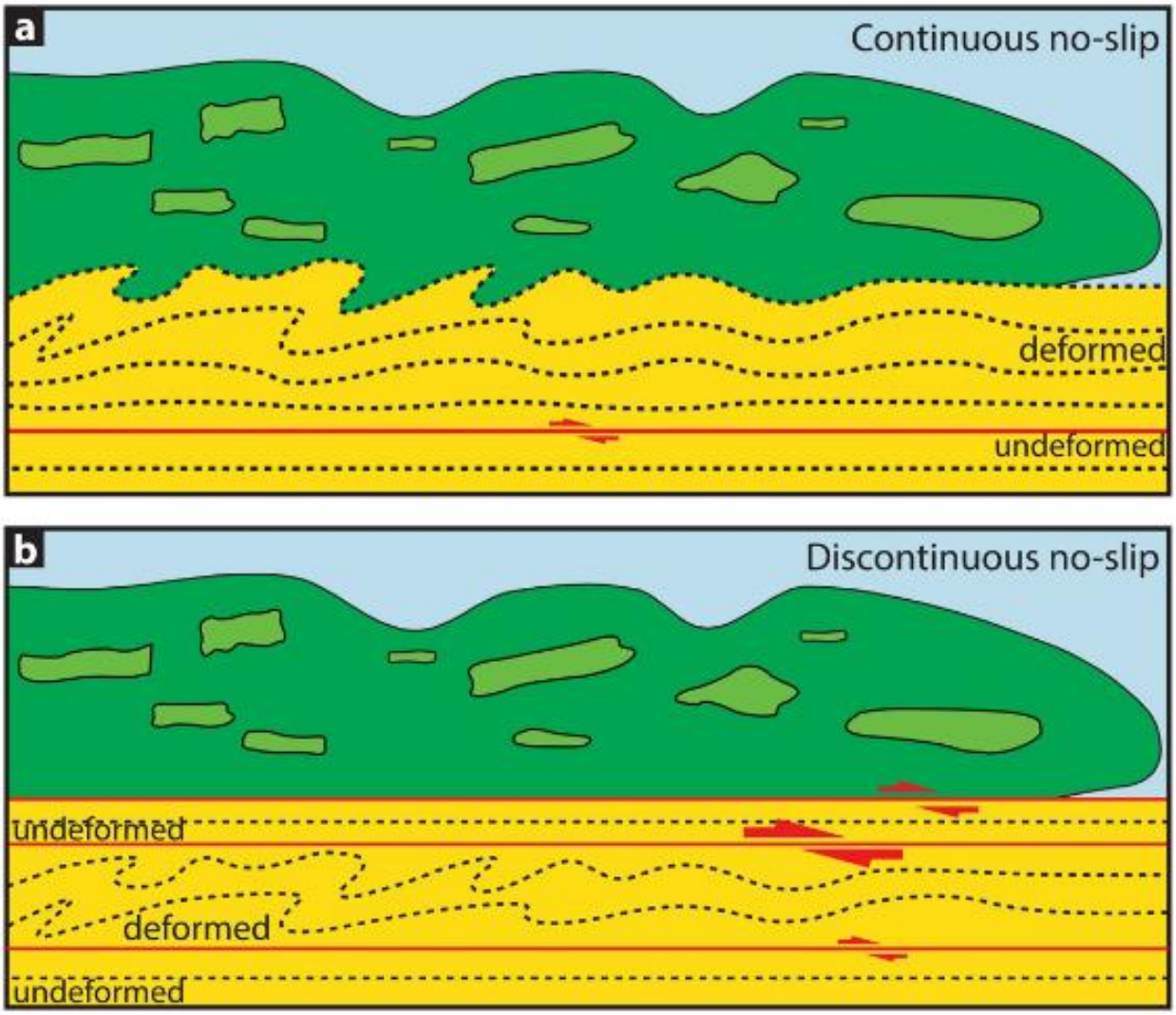

Figure 17: Block diagram illustrating two styles of no-slip substrate deformation associated with the BSZ. (A) *Continuous no-slip deformation*—substrate is entirely deformed down to either a diffuse strain front or a discrete basal shear zone that marks the boundary with underlying undeformed strata. (B) *Discontinuous no-slip deformation*—the uppermost portion of the substrate remains undeformed, preserved between an upper and lower shear zone, while deeper strata are progressively deformed down to a diffuse strain front or basal shear zone. Figure taken from Sobiesiak et al. (2018).

4). Depositional Facies Assemblages

The strata surrounding the studied deposit can be categorized into distinct facies assemblages, including interstratified shale and sandstone units, a basal deformational contact, and a Megabed assemblage subdivided into three main divisions: (1) sandy mudstone diamictite with blebs/small blocks (2) sandstone blocks, and (3) homogenized muddy diamictite.

4.1. Interstratified Shale and Sandstone (ISSF)

DESCRIPTION: This facies consists of a series of coarsening-upward successions (CUS). At the base of each cycle, thick laminated shale bedsets gradually thin upward as progressively coarser sandstone beds are observed. Conversely, sandstone occurs as thin laminations at the base and thickens upward into coarser beds ~0.25 – 1.5 m thick. The total succession reaches over 85 m in thickness from the base of Section 1 to the base of the MTD deposit (Figure 20A). Across the outcrop, 8–10 coarsening-upward cycles occur, each exhibiting similar characteristics that create a stacked/repeating facies pattern. The cycles in the middle of the outcrop are the thickest (<10 m), whereas those at the upper and lower portions are comparatively thinner (Figure 19A-C).

The lower contact of the first cycle is a sharp boundary between shale beds and the coarse sandstone of the underlying CUS (Figure 20A-B). Horizontally laminated shale beds at the base of each cycle reach thicknesses of up to 8 m but gradually thin to just a few centimeters upward. These shale bodies appear laterally continuous across the outcrop and constitute the majority of each cycle's thickness. Contacts between shale and overlying sandstone are predominantly sharp, though in some cases, medium to coarse-grained sandstone beds rest on erosional contacts with the underlying shale.

At the base of each cycle, fine sandstone occurs as laminations that progressively thicken to beds (up to 1.5 m) and coarsen upward toward the top of the cycle. The coarser sandstone exhibits laterally thinning beds that pinch out within the outcrop over tens to hundreds of meters towards the North. Fine-sandstone laminations consistently preserve current ripples and occasionally contain small fragments of plant material. As the sandstone beds thicken upward,

there is occasional grading preserved, and sedimentary structures become more diverse but vary between cycles. In the lower cycles, the coarser beds display current ripples, super-critical flow (plane bed and antidune structures), and plant material. Paleocurrent orientations (cross-laminations, n = 18) return a mean flow direction of 038.9° ± 10.1° (Figure 18A-B). Toward the middle of the outcrop, antidune beds diminish, and soft-sediment deformation, including folding, becomes more prominent. Deformed material often incorporates rip-up clasts derived from underlying shale units. In the uppermost cycles, a combination of current ripples, rip-up clasts, plant material, and fluidization features (e.g., injections and loading structures) occur (Figure 20B-F, 21A-C). Additionally, soft sediment deformation structures and folds become more pronounced near the contact with the MTD that bounds the stacked CUS facies above.

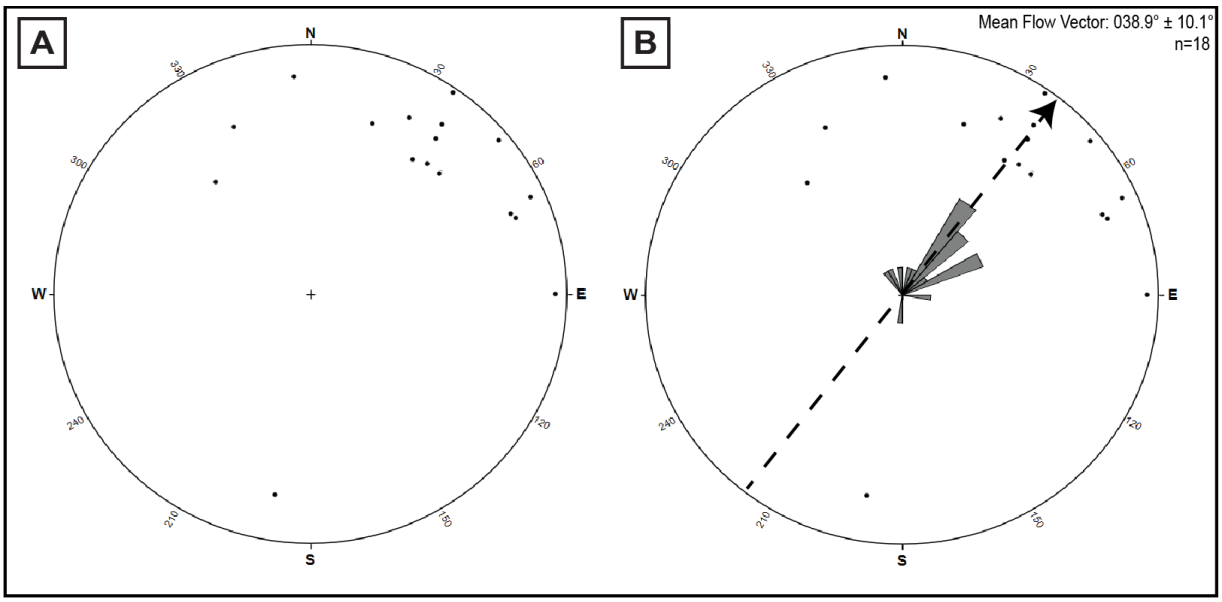

Figure 18: (A-B) Plotted planes and rose diagram for paleocurrents within Facies 1. Paleocurrent orientations (cross-stratification, n = 18) return a mean average flow direction of 038.9° ± 10.1°. Paleocurrents are consistent with a NE direction of flow across the facies succession

INTERPRETATION: The repeated cycles in Facies 1 were deposited by episodic subaqueous density currents in the form of turbidites, as indicated by coarsening-upward interstratified shale and sandstone successions, the lateral continuity of the sandstone beds, the occurrence of graded

beds, and the occurrence of asymmetric ripples deposited by both subcritical and supercritical tractive flows. Additional evidence for tractive, erosional underflows includes the presence of rip-up clasts and preserved current ripples, that reflect the capacity of these flows to erode underlying sediments and transport coarse debris (Hampton, 1972; Mulder & Alexander, 2001; Posamentier & Walker, 2006; Pickering, 2016). The paleocurrent data indicate a consistent northeast-directed sediment transport, suggesting a paleoslope dipping toward the NE at approximately 039°. This orientation implies the depositional system could be influenced by a regional topographic gradient trending in that direction. The coarsening upward progression observed within the turbidites is most likely associated with base-level change. Coarser intervals near the top of each cycle could be a result of deposition closer to continental margins as base-level nears a low. Conversely, shale beds at the bottom of each cycle could deposit with base level rise allowing for a majority of fine material to accumulate (Coe et al., 2005; Coe et al., 2005; Catuneanu, 2022). The observed variations in vertical cycle thickness—alternating from thin to thick and back to thin—throughout the succession may reflect the interplay of three primary controls: turbidite lobe switching, base-level fluctuations, and/or basin subsidence/uplift. Turbidite deposits migrate laterally across the basin floor in lobe-shaped formations. As the active lobe shifts, depositional thicknesses fluctuate depending on the changing direction of the migrating lobe (Mutti & Lucchi,1972; Posamentier & Walker, 2006). Rising and falling of base level shifts the terminal deposition of turbidites, with changing transport distance and differences in accommodation space, base-level fluctuation allows for variation in cycle thickness to develop over longer time intervals (Coe et al., 2005; Nichols, 2023). Basin subsidence/uplift may also contribute by increasing/decreasing accommodation space; shifting the distal extent of turbidites

basinward across the locality (Coe et al., 2005). Proximity to the Valle Fértil Lineament could potentially be a source of basin subsidence/uplift for this variation in succession thickness.

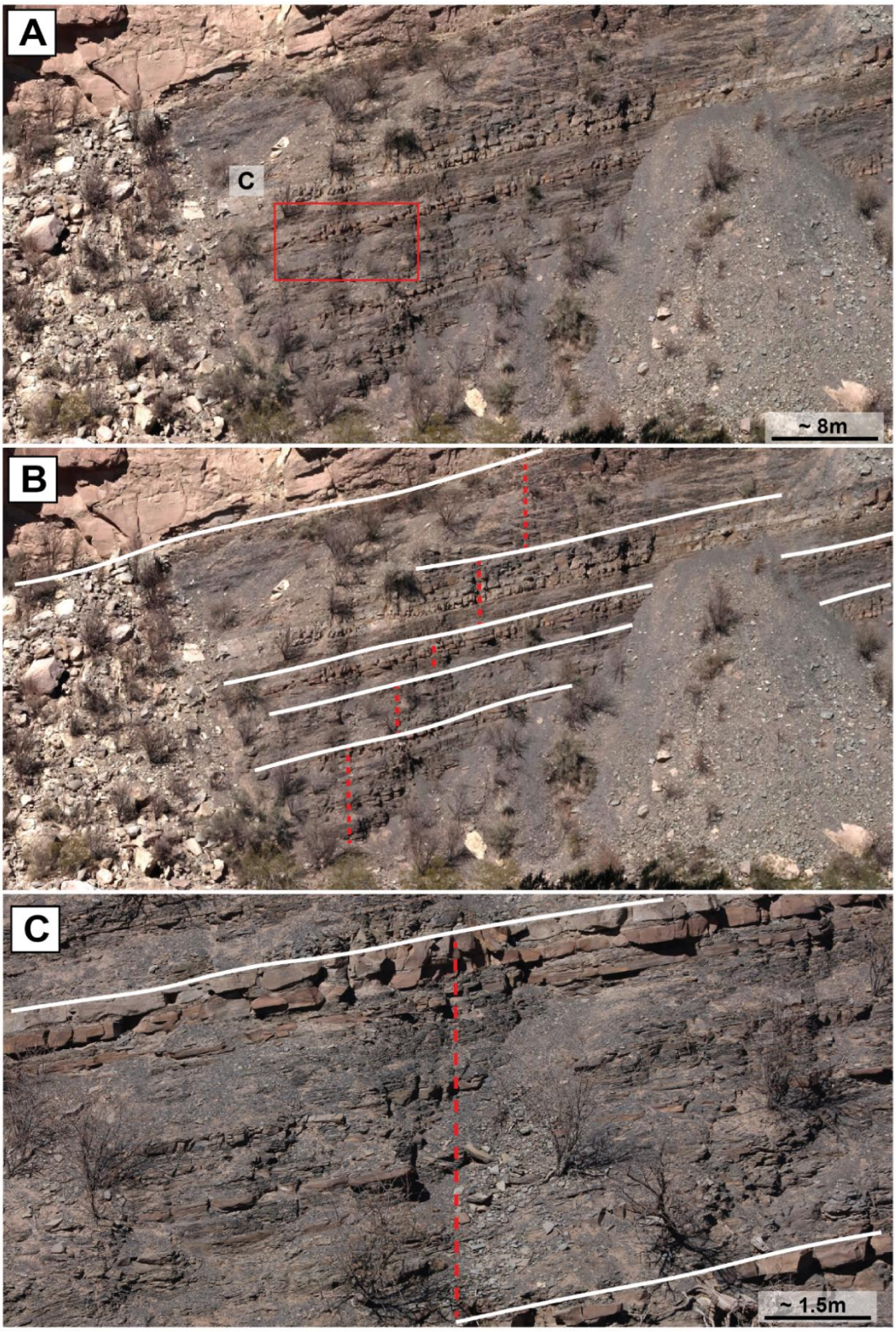

Figure 19: (A) Figure shows the CU cycles repeated throughout the outcrop. Notice the variation in thickness between the cycles present within this outcrop. (B) Annotated cycle contacts drawn to show changing cycle thickness within Facies 1. (C) Close up view showing an example of a CU cycle.

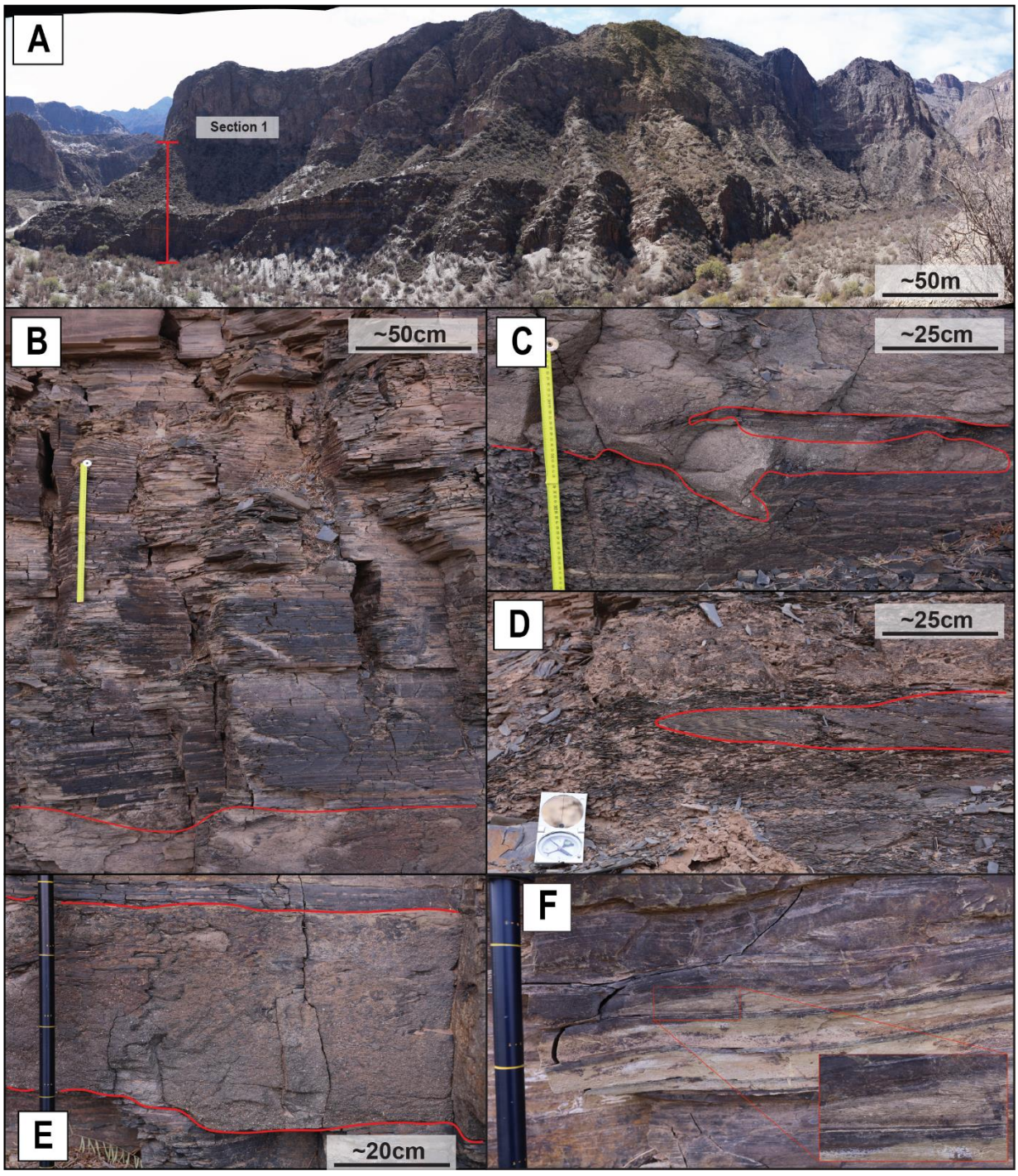

Figure 20: Images show prominent structures shown throughout the first coarsening upward sequence. (A) Displays the entire section and boundaries measured for the turbidite succession. (B) Horizontally laminated shales with thin layer of sand making up most of the turbidite succession. (C) Sand injection into the underlying substrate within a concentrated density flow. (D) Shows shearing within shale around a more competent sandstone body. (E) Erosive coarse-grained density flow containing rip-up clasts of shale from the overlying layer (F) Super critical flow structures creating sinusoidal bedding. Beds display antidunes displaying cross laminations in the opposite direction of measured flow.

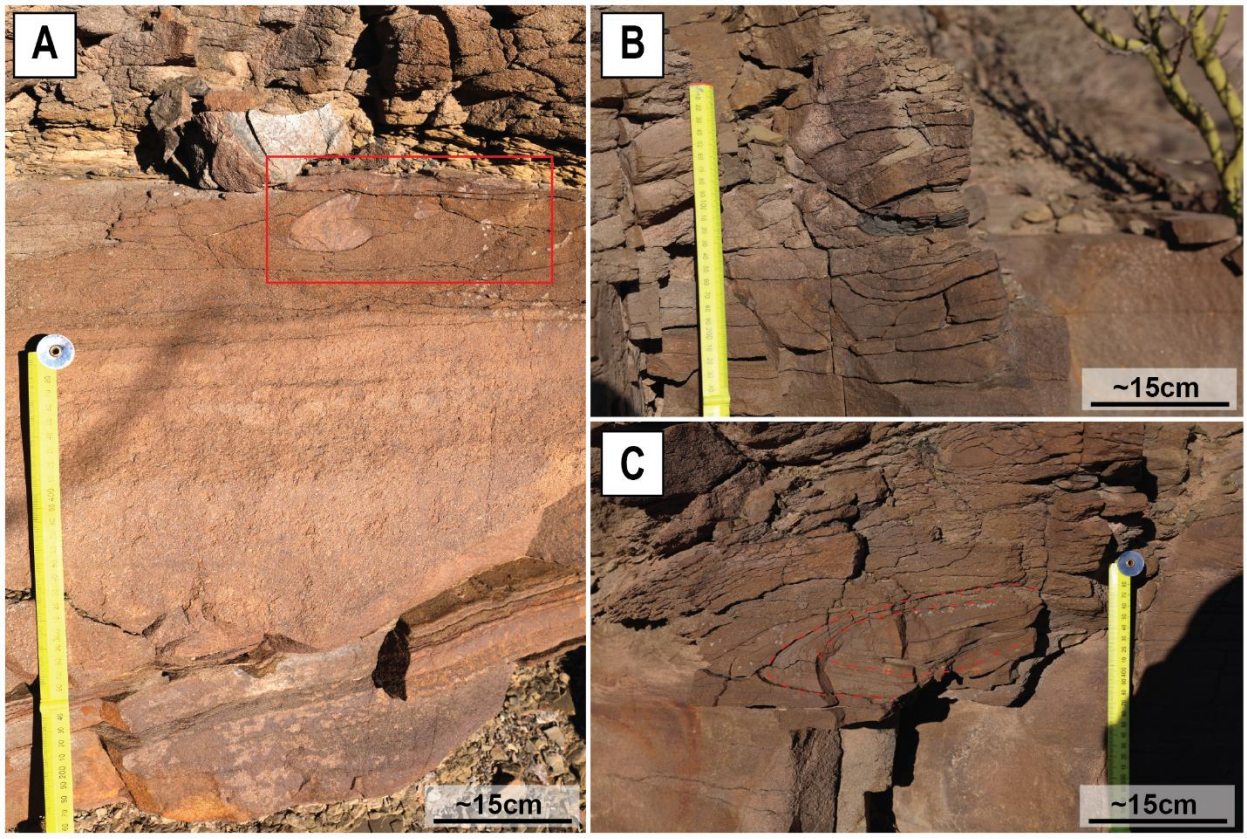

Figure 21: Changes in lithology and sedimentary structures within the second coarsening-upward sequence. (A) An erosive concentrated density flow featuring rip-up clasts in the upper portion of the bed. (B) Rip-up clasts within the same bed, surrounded by massive medium- to coarse-grained sand. (C) A fluidized sand body exhibiting folded sand laminations overlying more competent material.

4.2. Basal Deformational Contact

DESCRIPTION: The BSZ within the studied outcrop exhibits variability along the 300-m transect. BSZ thickness is greatest at the southern end (Section 1) where it exceeds 2 m and rapidly thins to 0.5–1 m northward across the remainder of the deposit. Erosion is more pronounced within thicker portions of the basal shear zone and diminishes toward the thinner, northern extent of the deposit. The overlying mass transport matrix lithology varies above the contact, ranging from a clast-poor muddy diamictite to a clast-poor sandy diamictite. In the northern portion of the transect (Section 4), matrix volume gradually decreases, transitioning to coherent/lightly deformed fine-medium sandstone blocks that overlie and incise the substrate.

Irregularly distributed sandy conglomerate patches, ranging from 50 cm to 4 m in length and 20 cm to 2 m in thickness are observed within the BSZ. Clasts within these units include intrabasinal sandstones and an assemblage of basement-derived igneous and metamorphic clasts, ranging in size from pebbles to cobbles.

The southern end of the transect (Section 1) initially exhibits two separate zones of deformation. The upper deformation zone develops at the interface between the mass transport deposit and the underlying sandstone unit. This deformation zone contains a thin (<0.25 m) layer of brecciated shale, exhibiting gentle asymmetric and recumbent folds and is laterally continuous (Figure 22A). A lower deformation zone forms between the sandstone unit and underlying shale beds. There, deformation occurs as discontinuous, open asymmetrical folds within the underlying shale, with fold heights of approximately 1 m and lengths of 3–4 m (Figure 22B). This zone extends for 25-30 m across the outcrop.

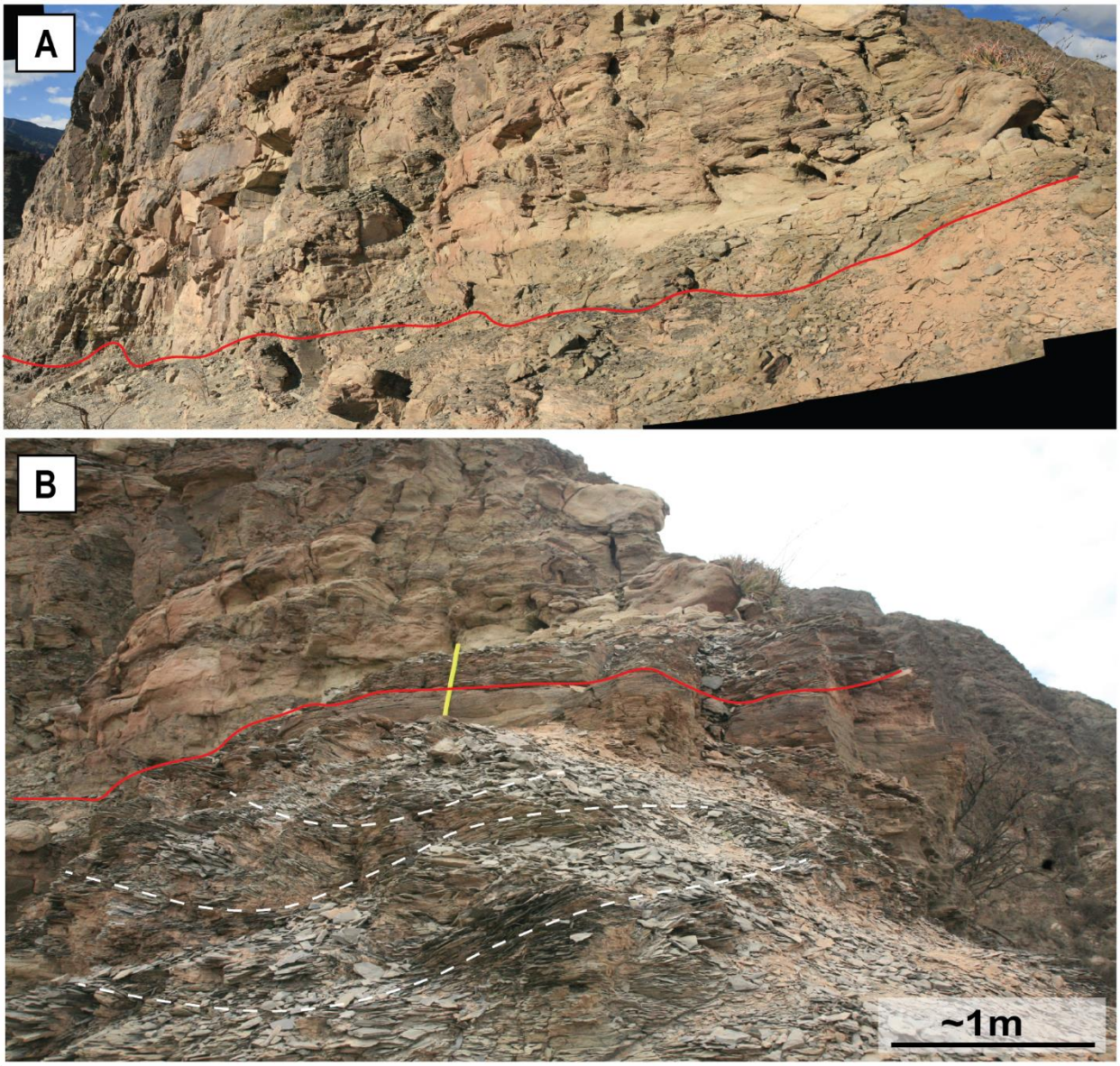

Figure 22: (A) Overview of BSZ for Section 1, note the erosive contact. (B) Lower deformational zone showing open asymmetrical folds overlain by undeformed sandstone layer. Upper deformational zone exits above red contact line < 0.25 m in thickness.

In sections 2–4, the BSZ is primarily dominated by erosion, creating a shear surface characterized by a 0.25–1.0 m thick brecciated shale. Observed soft sediment deformation structures (SSDS) include recumbent and open asymmetrical folds within the shale, containing facing directions to the north (Figure 24C, D). In Sections (2–3), a homogenized, clast-poor, mud-rich matrix occurs incising into the substrate (Figure 23A-D), with the occurrence of

sandstone blocks (1–3 m in length) incised into the underlying substrate along the contact (Figure 23B). Transitioning into Section (4), the matrix interval dissipates, and substrate erosion shapes the BSZ through the presence of large blocks (Figure 24A). Here, the BSZ maintains the same degree of incision throughout the continuation of the brecciated shale layer with direct contact with the blocks.

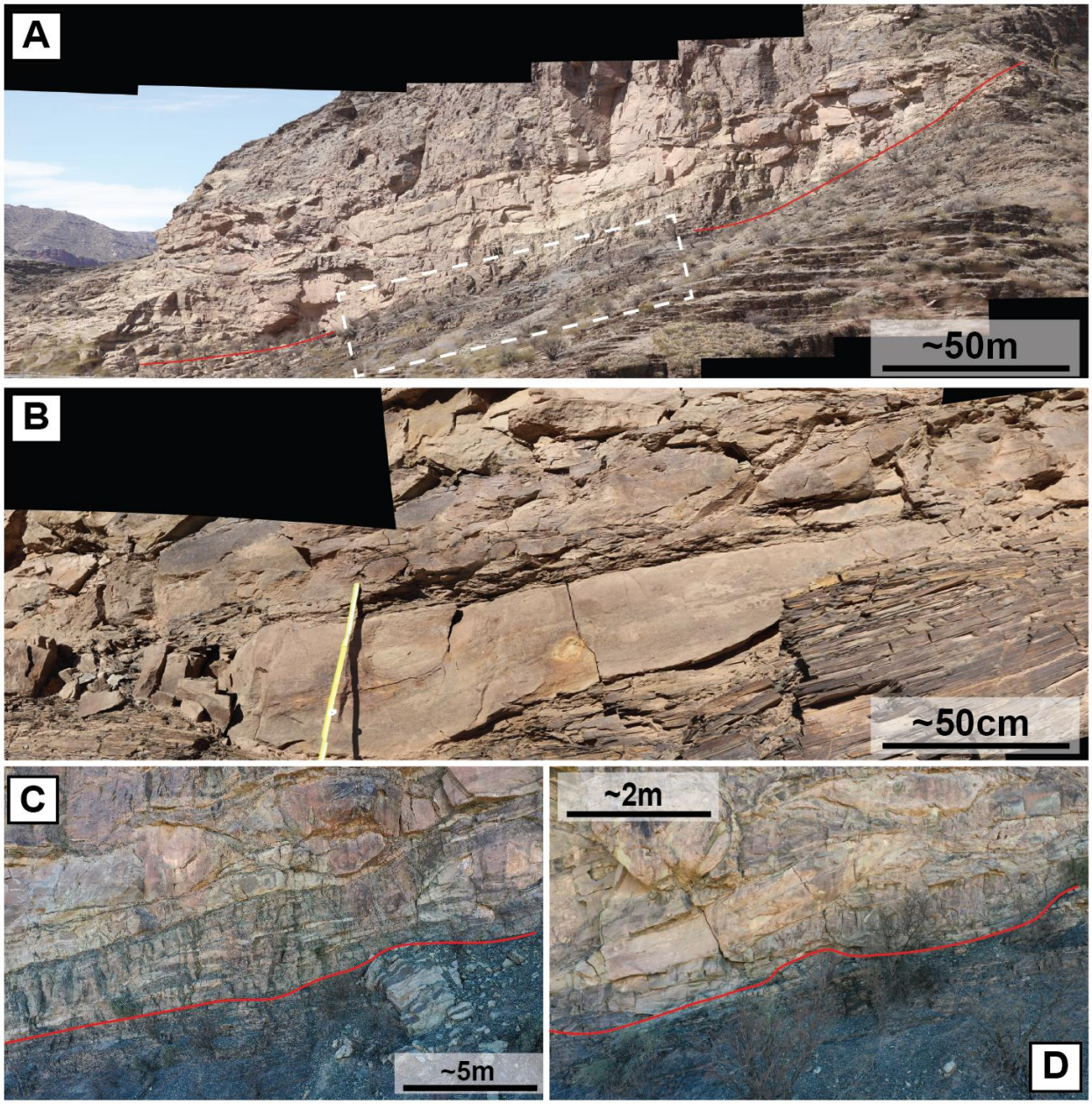

Figure 23: (A) Overview of BSZ for Section (2-3) (B) Small block ~1.5 m long incises the substrate at the BSZ. (C) Area of maximum erosion within BSZ. (D) Gradual transition to a more stable erosion regime across the remainder of the BSZ

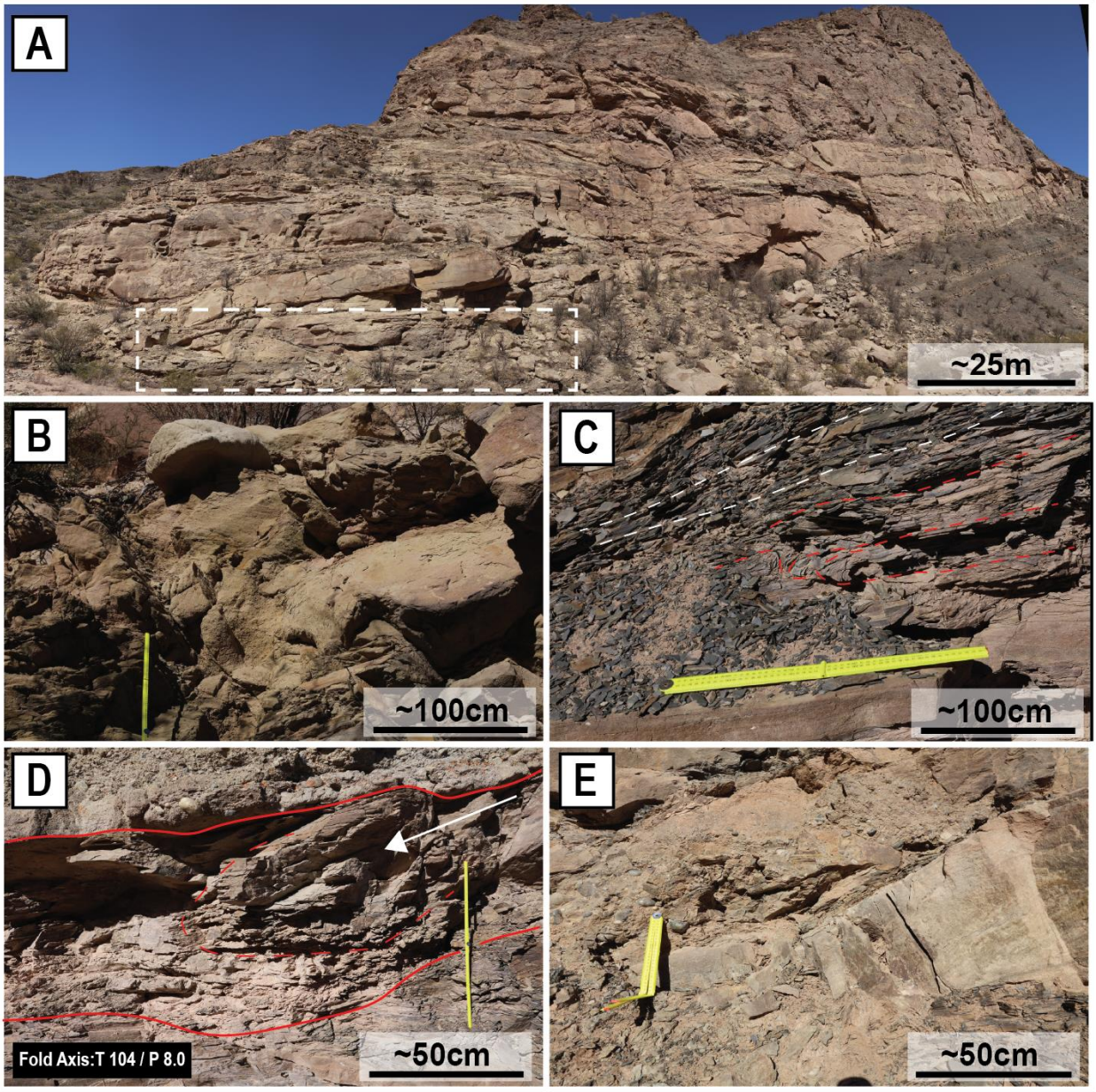

Figure 24: (A) Overview of the BSZ locality for Section 4 (B) Large sandstone blocks above BSZ exhibit thrust planes, with displacement directed to the north. Fluidization fabrics are observed within the lower portion of the blocks. (C) Sheared and brecciated BSZ displaying recumbent folds. Facing direction to the north. (D) Combination of recumbently folded shale with gravel incorporation within the BSZ. Facing direction to the north. (E) Undeformed sandstone clast and sandy conglomerate pieces incorporated into the BSZ.

Across the northern extent of Section 4, the BSZ dips below creek level and is lost into the subsurface, likely to a maximum depth of 1–2 m beneath the creek bed if the dip of the surface is maintained. Here, block behavior evolves from more coherent to increasingly plastic

and fluidized towards Section 4 (Figure 25A-E). Fluidization structures above the BSZ are preserved as large-scale pinch-and-swell features (2 m in length, 1 m in height), fluid flow fabrics, banded injections producing flames between separated blocks (<1 m – 3 m in height and 0.25 – 0.5 m in width), and dewatering pipes/sheets occur within overlying blocks throughout the remainder of the outcrop (Figure 25B-E). Normal faults and thrust faults are also prevalent within and between the blocks in Section 4.

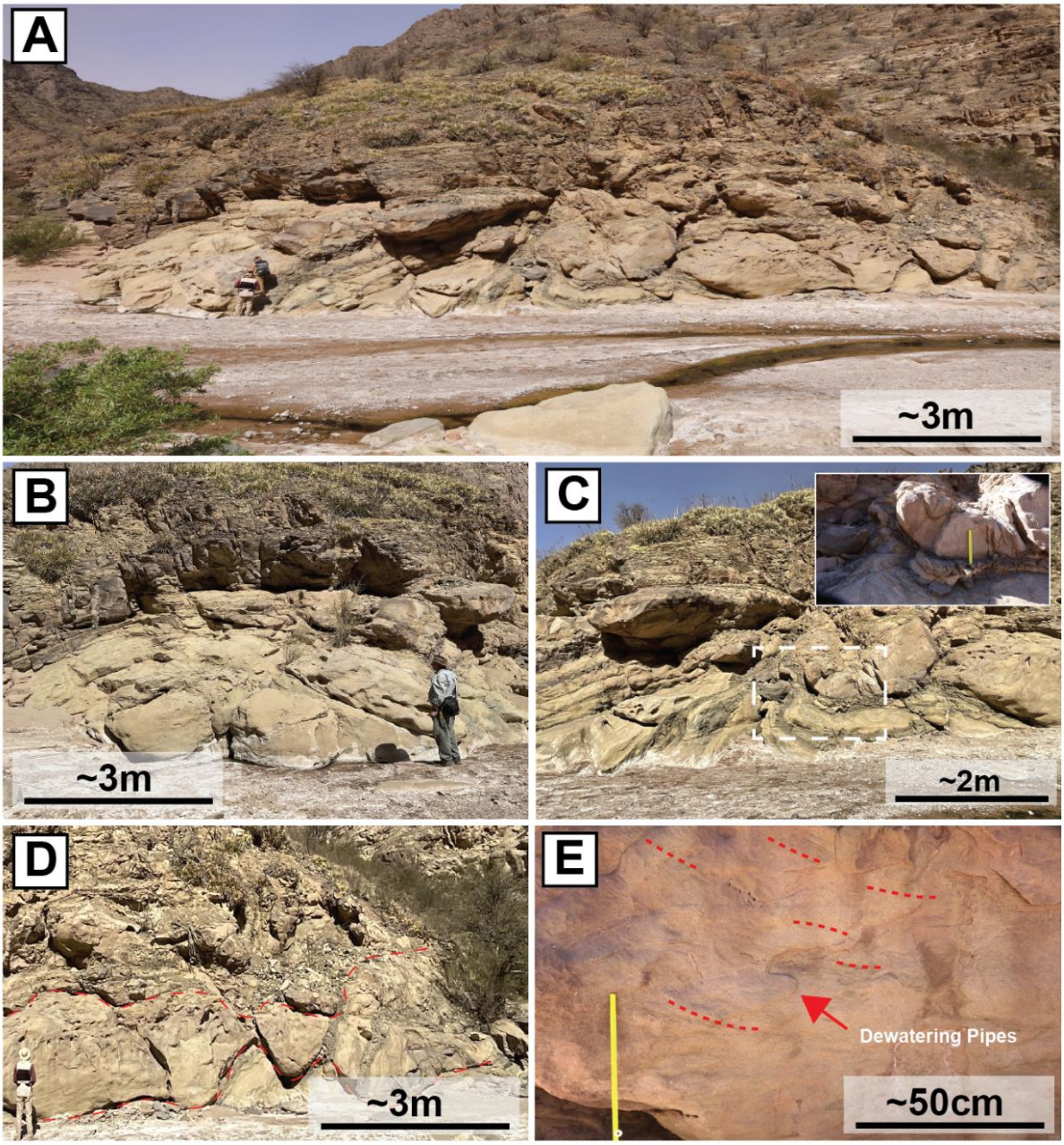

Figure 25: (A) Overview showing final extent of Section 4 along BSZ. BSZ is estimated to be 1-2 m below creek level. (B) Flow fabric and thrusting observed above BSZ. (C) Heterogeneous banded injections occurring laterally and vertically above BSZ. (D) Fabrics and pinching shape at the end of blocks creates pinch-and-swell structure between annotated lines. (E) Dewatering pipes within blocks above BSZ.

Additionally, BSZ observations were made along another transect around the same stratigraphic level approximately 0.5 km west of the primary study location (see Figure 1, 26A). The BSZ along the western transect maintains a considerable thickness (0.5–3 m) and contains sheared and brecciated shale at the contact between the mass transport deposit and the underlying

substrate, which is similar to previous observations within the eastern transect. The overlying deposit consists of an interval of blocks, 5-10 m thick & 10-15 m in length (Figure 26A), that transition to a deformed zone of heterogeneously banded sandstone and shale to the north (Figure 27A-B). Sporadically, sandy conglomerates with similar textural characteristics to the eastern transect occur along the BSZ at this site.

At the southern end of the western transect (Figure 1), the BSZ begins as an erosional contact, where blocks incise the underlying substrate (Figure 26A). Shearing and brecciation is pronounced within shale often containing small inclusions of cobbles and pebbles. To the north the blocks appear to fracture and broken clasts occur within the shale of the BSZ displaying a sheared and heterogeneously mixed appearance (Figure 26B, C). The BSZ then widens (>3 m) and transitions to heterogeneously banded sandstone and shale. The contact remains erosional, but open symmetrical, open asymmetrical, closed asymmetrical, and detached folds occur within the banded unit (Figure 27A-B). Additionally, plastic-like fabrics, injections, and dewatering structures occur within small localities of the western transect (Figure 28A-D).

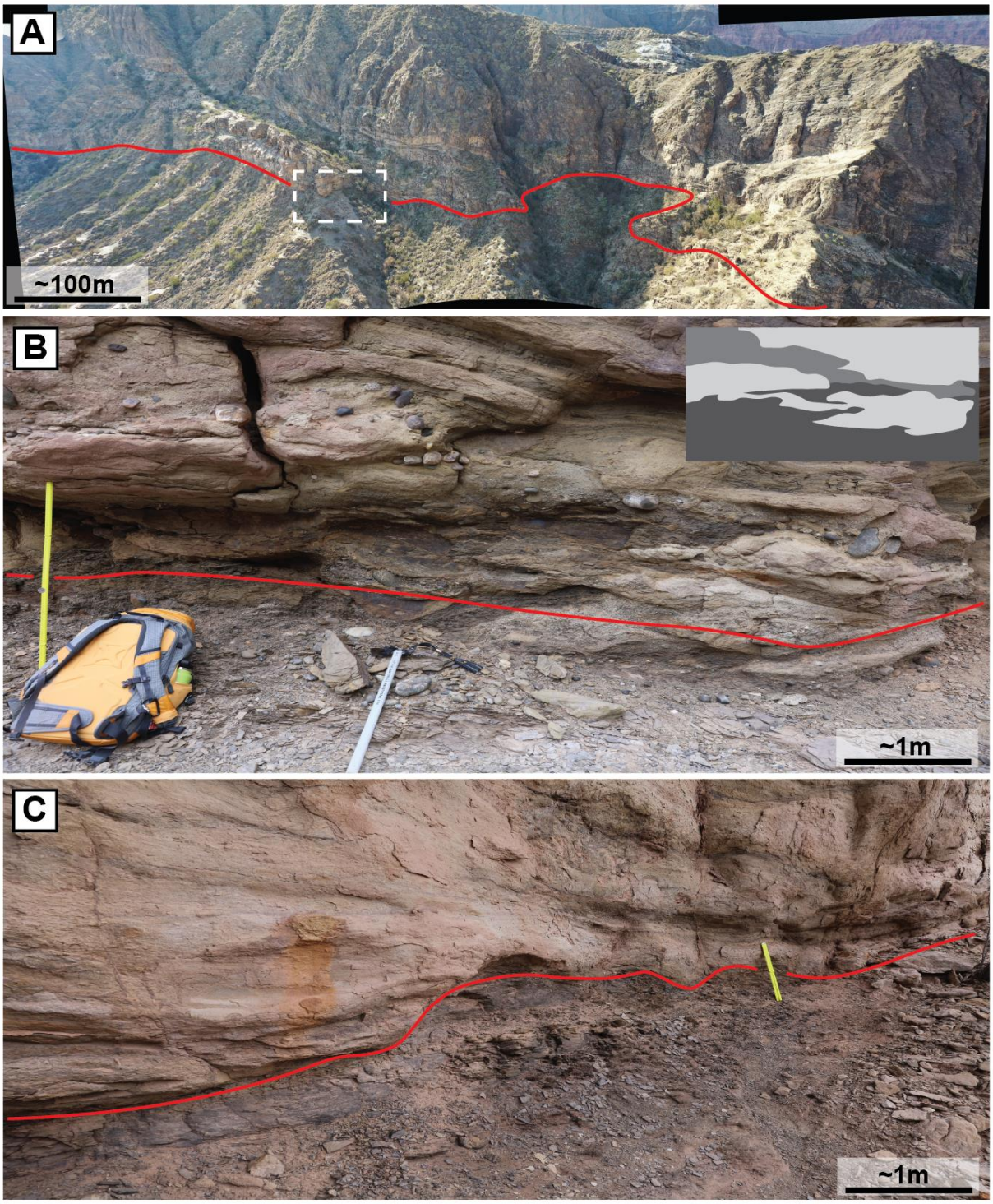

Figure 26: (A) Overview of western transect of MTD BSZ. (B) Erosive contact showing fragmentation of block with gravel inclusion at BSZ. (C) Continuation of erosive contact along BSZ.

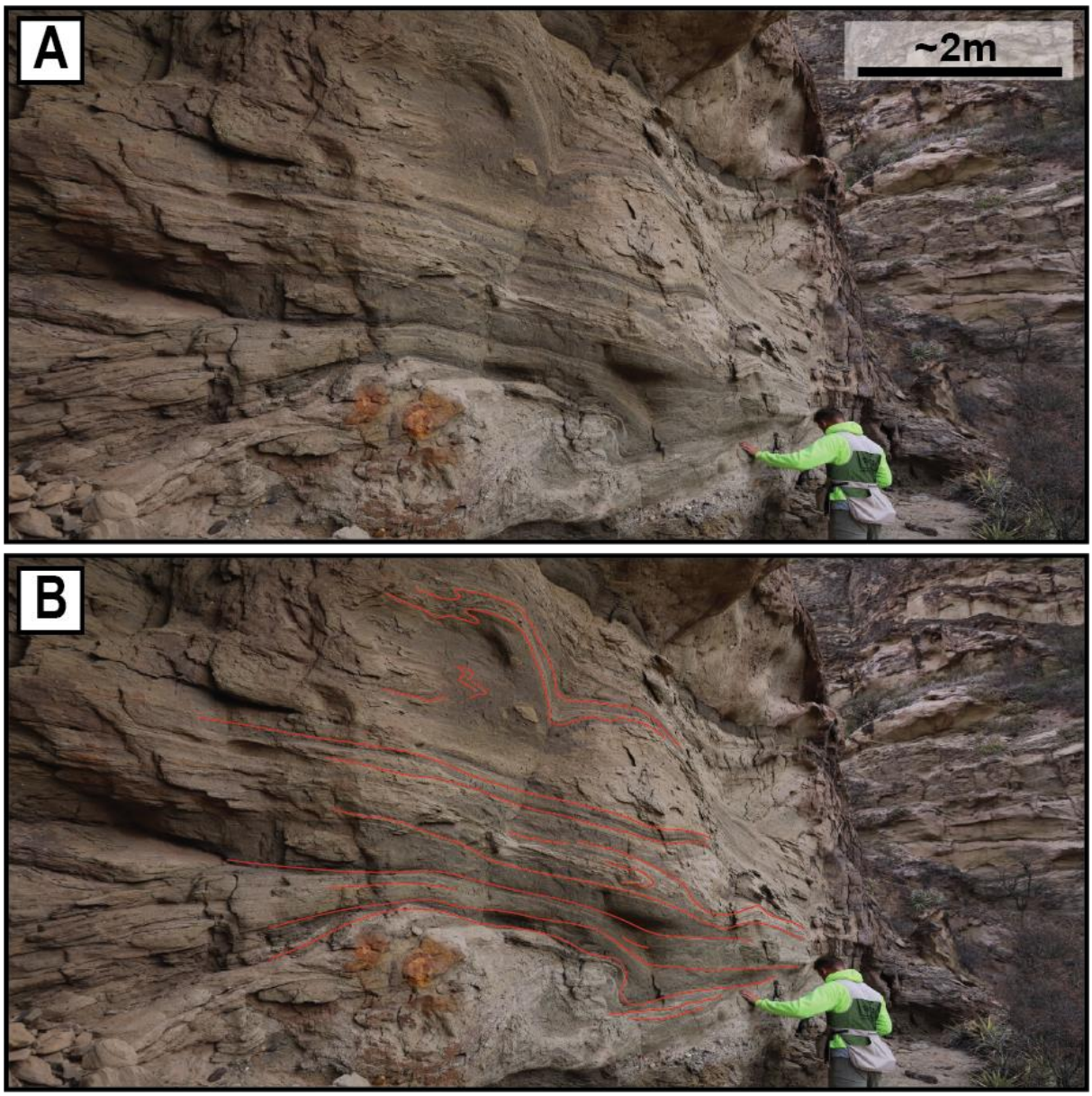

Figure 27: (A) Photograph of heterogeneously banded matrix showing various deformational structures. (B) Tracing of fold types observed in the matrix outcrop above the BSZ, including open symmetrical and asymmetrical folds, closed asymmetrical folds, and detached folds.

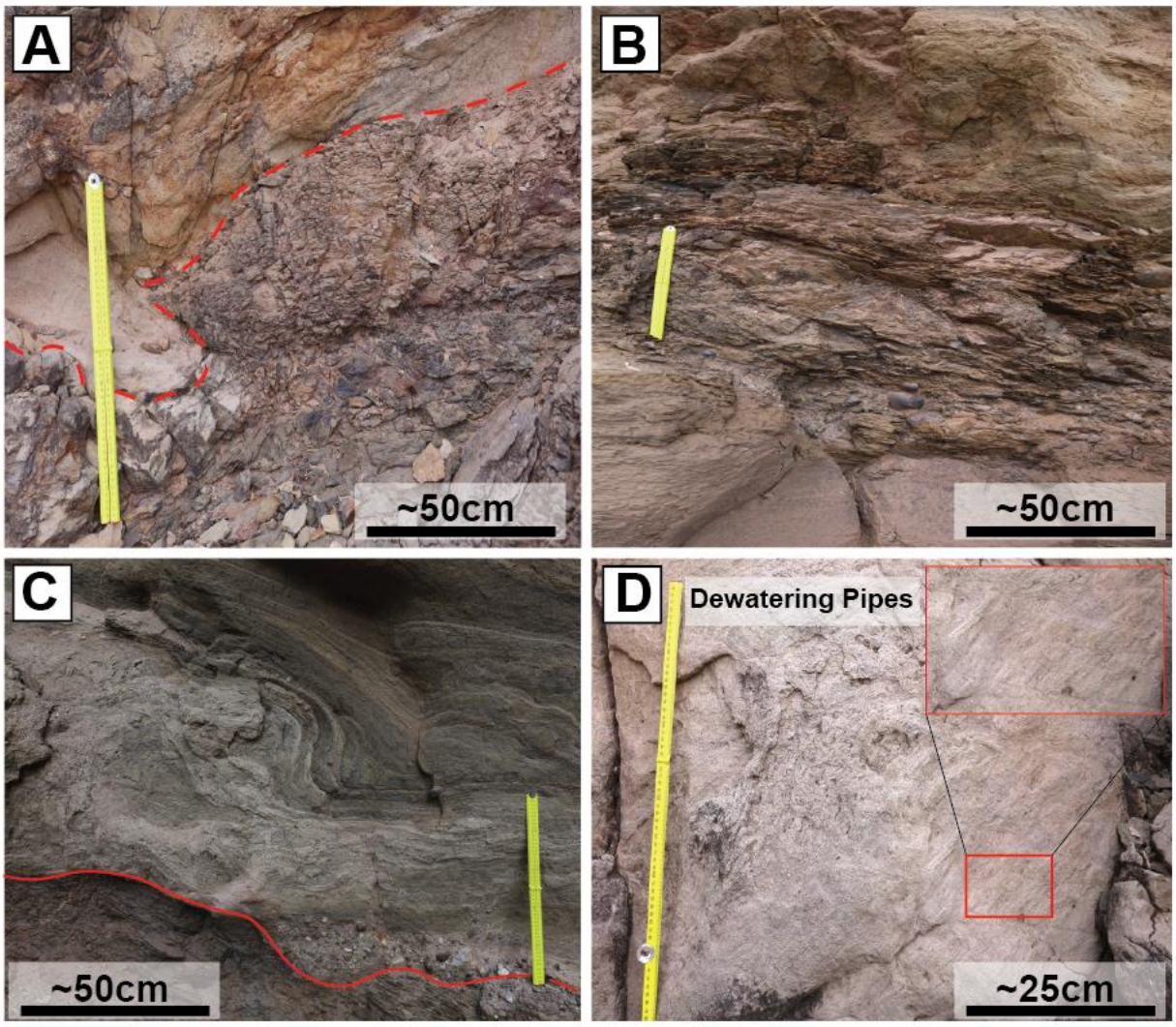

Figure 28: Soft sediment deformation structures observed across BSZ western transect. (A) Sandstone injection from the mass transport above BSZ. (B) Pronounced brecciation at BSZ with inclusion of pebbles to cobbles. Brecciation is created by cm scale spaced shear zones. (C) Asymmetrical open fold within banded matrix. (D) Dewatering pipes within sandstone blocks at BSZ contact.

INTERPRETATION: The variability in thickness, deformation style, and lithologic composition of the BSZ along the studied transect reflects dynamic changes in basal conditions during mass transport. The kinematics along the BSZ is reflected by a mosaic of changing conditions observed across the contact. Beginning at the southern end of the transect, the BSZ initiates as a discontinuous, no-slip deformational zone (Section 1), which rapidly transitions into a large segment dominated by erosion processes (Sections 2–3). The BSZ was later covered by

Quaternary sediment, but signs of fluidization are seen within the BSZ and just above it before complete coverage. Additionally, sporadic inclusions of sandy conglomerate/gravel along the BSZ are also observed, which may have played a role in facilitating fluid flow or deformation propagation.

Beginning at Section 1**,** the thicker BSZ interval exhibits discontinuous no-slip deformation**,** characterized by two distinct shear zones separated by an undeformed substrate**.** No-slip deformation occurs where the mass movement is welded to the underlying substrate and the associated strain penetrates with depth, The upper deformed unit**,** composed of thin, brecciated shale, is separated from the lower deformed unit**,** consisting of gently folded asymmetrical and recumbent folded shale, by a layer of undeformed sandstone (Figure 17A; Sobiesiak et al., 2018). This deformation sequence results from the downward penetration of stress, often influenced by localized variations in basal shear zone geometry due to faults, bedding planes, or material property differences (Sand vs mud; Bull et al., 2009; Alves & Lourenço, 2010; Omosanya & Alves, 2013). As the MTD propagated northward, the BSZ transitioned from a thick, multi-detachment zone to a more localized erosional shear surface (Sections 2–4; Figure 23A, 24A). The thinning of the BSZ, along with the presence of a brecciated shale layer, suggests that the mass flow eroded and entrained material from the underlying substrate. Ogata et al. (2012) proposed that strain coupling, including substrate erosion, occurs as a result of flow deceleration. For example, as hydroplaning dissipates in the direction of flow due to excess pore pressure generated by frictional freezing, facilitating momentum transfer to the seafloor. The development of the erosional surface may be attributed to the movement of large blocks at the base of the deposit (Section 4), which likely slid and decelerated before their final emplacement further downslope. Additionally, the brecciated strain

observed within the shale of the BSZ may reflect deformation induced by block sliding and development of a localized shear zone.

The sporadic distribution of sandy conglomerate/gravel at the BSZ may result from grain or turbulent flows preceding mass transport. Fallgatter et al. (2017) documented a similar but more intact conglomerate layer at the base of a megabed in the Cerro Bola outcrop 40 km to north. These deposits are thought to have formed from an early high-density turbidity current (Lowe, 1982) or a concentrated density flow (Mulder & Alexander, 2001), potentially acting as a gravelly traction carpet. The conglomerate layer at Cerro Bola is also inconsistent in thickness, suggesting that erosion and shearing led to its disaggregation. A similar process may explain the sporadic conglomerate distribution within the studied MTD at Agua de la Peña Creek. Additionally, Buso et al. (2019) documented a gravel/conglomerate unit at the base of another MTD within Agua de la Peña Creek, closely resembling the patches observed in this study. They suggested that gravel played a role in sustaining an overpressured hydraulic system, acting as a lubricant. The trapping of overpressured water between the moving mass and the seabed has been proposed as a mechanism for the high mobility of subaqueous debris flows (Mohrig et al., 1998; De Blasio et al., 2004). Thus, the interconnected pore fluid within the basal gravel likely formed a hydroplaning layer, reducing friction and facilitating transport movement.

The increasing presence of fluidization structures (sediment injected between pinch-and-swell features, flow fabrics, banded injections, and dewatering pipes) towards Section 4 and within the western transect, suggest a transition from frictional shearing to a domain of liquefication (Lowe, 2006; Ogata et al., 2014; Sobesiak et al., 2018, Oyanyan et al., 2020; Jamil et al., 2021). Liquefaction occurs when/where consolidated sediments experience a sudden loss of shearing resistance coupled with a grain framework collapse while there is a short-term

increase in pore pressure (Terzaghi, 1947; Lowe, 2006). According to Lowe (2006), liquefaction in the formation of fluidization structures occurs as a three-step process: (1) the near-total loss of sediment strength during liquefaction enables it to respond easily to gravitational or fluid forces; (2) fluid escape during resedimentation can induce full or partial fluidization of grains; and (3) water expelled from buried liquefied layers may trigger liquefaction and fluidization in overlying sediments.

A substantial portion of Section 4 lacks direct exposure of the MTD-to-substrate contact. However, fluidization structures are exposed just south of where the contact dips into the subsurface and assuming a consistent depth of incision along the exposure, the BSZ is unlikely to extend more than 2 m below creek level to the north of Section 4. The transition to fluidization within the BSZ may be influenced and observed by any combination of three proposed mechanisms.

1. **Sandy Conglomerate/Gravel Layer:** These deposits may act as a lubricating layer, facilitating mass movement and enhancing downslope mobility through elevated pore-water pressure and reduced friction. Increased pore-water pressure induces liquefaction, which in turn, could produce more fluidization structures. A thicker or more abundant layer of conglomerate/gravel at the buried BSZ in Section 4 could drive liquefaction.
2. **Block separation/fragmentation:** Sobiesiak et al., (2017) proposed a block-dominated emplacement model in which blocks may fragment, settle into the underlying material, and induce upward injection of substrate through newly formed gaps (Figure 13A, 25A, 29A). Similar processes of block fragmentation driven by increased kinetic energy have also been documented by Kvalstad et al. (2005), Micallef et al. (2007), and Alves (2015).

3. **Fluid escape of the underlying substrate through the presence of block loading:** Similar to block separation, injections generated through loading may result from variations in density, saturation, and compositional differences between the blocks and the underlying substrate. These factors could facilitate the upward injection of material from the BSZ, further enhancing the separation of already fluidized blocks. Moretti & Sabato, (2007), Alves, (2015), and Sobiesiak et al., (2016) discuss instances of extensive fluidization as a response to large-scale load structures.
4. **Post-seismic activity:** Seismic shaking of loose granular sediments beneath the blocks can induce densification of sandy units. With insufficient time for water dissipation, excess pore water pressures may develop beyond hydrostatic levels, reducing effective stress (e.g., Allen, 1982; Owen, 1987; Nicholas, 1995). These conditions are sufficient to initiate block movement and, if seismic shaking occurs and intensifies, it may ultimately lead to the liquefaction of underlying sediment (Lourenço et al., 2006; Alves, 2015). An immediate response often results in sliding or sinking, of blocks into the underlying strata (Alves, 2015). Jamil et al., (2021) suggested that the presence of large mud intrusions can be associated with tectonics (Figure 13A, 25C).

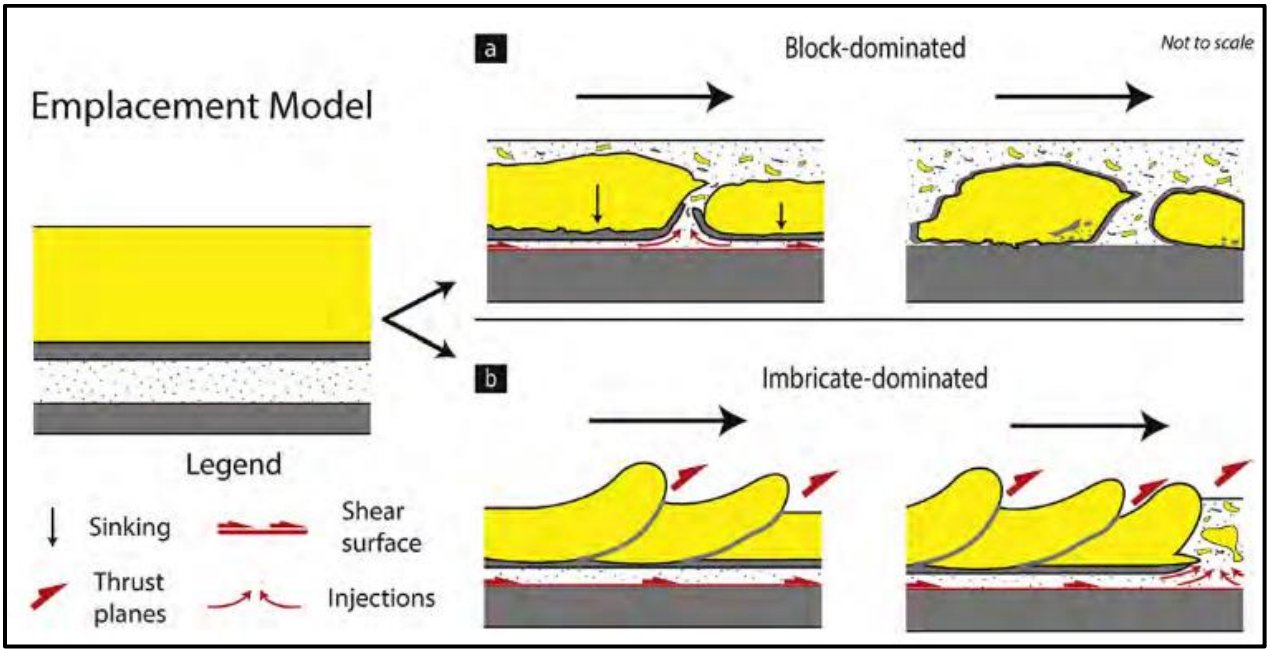

Figure 29: Figure adapted from Sobiesiak et al. (2017). The sketch illustrates the sedimentary and structural characteristics of block- and imbricate-dominated deposition. (A) In block-dominated deposition, separation between sand layers creates openings that allow the underlying material to inject upward. (B) An imbricate-dominated deposition, compression of the sand layer results in a series of thrusts, which are subsequently filled with injections or sheared material from the underlying substrate.

4.3. Megabed Profile

Several studies have documented different styles of vertical stratigraphic variation within mass transport deposits (e.g., Ogata et al., 2012; Sobiesiak et al., 2016; Fallgatter et al., 2017). These deposits form vertical sequences that can be subdivided into layers corresponding to cohesive and non-cohesive flow regimes. Deposits from this flow partitioning results in the formation of distinct stratigraphic units, often referred to as megabeds, within mass transport deposits. Megabeds have been variously described as seismites, megaturbidites, seismoturbidites, megabreccias, or mass transport deposits (Rupke, 1972; Mutti et al., 1984; Bouma, 1987; Fallgatter et al., 2017). Despite these classifications, no set criteria define what constitutes a megabed. Fallgatter et al. (2017) characterizes these deposits as exceptionally large sedimentary accumulations resulting from gravity flows, representing episodic and irregular sedimentation

events that produce significantly thicker beds than adjacent deposits. Additionally, megabed deposition is considered to involve more complex rheological behavior than the surrounding sedimentary units, reflecting variations in flow dynamics and material properties throughout their emplacement. To better understand vertical changes within the succession, the studied mass transport deposit at Agua de la Peña Creek will be referred to as a megabed**,** consistent with terminology used in previous literature. The megabed is here subdivided into three divisions (D1, D2a-b, D3; Figure 30) to assess compositional and kinematic variations within the mass transport system.

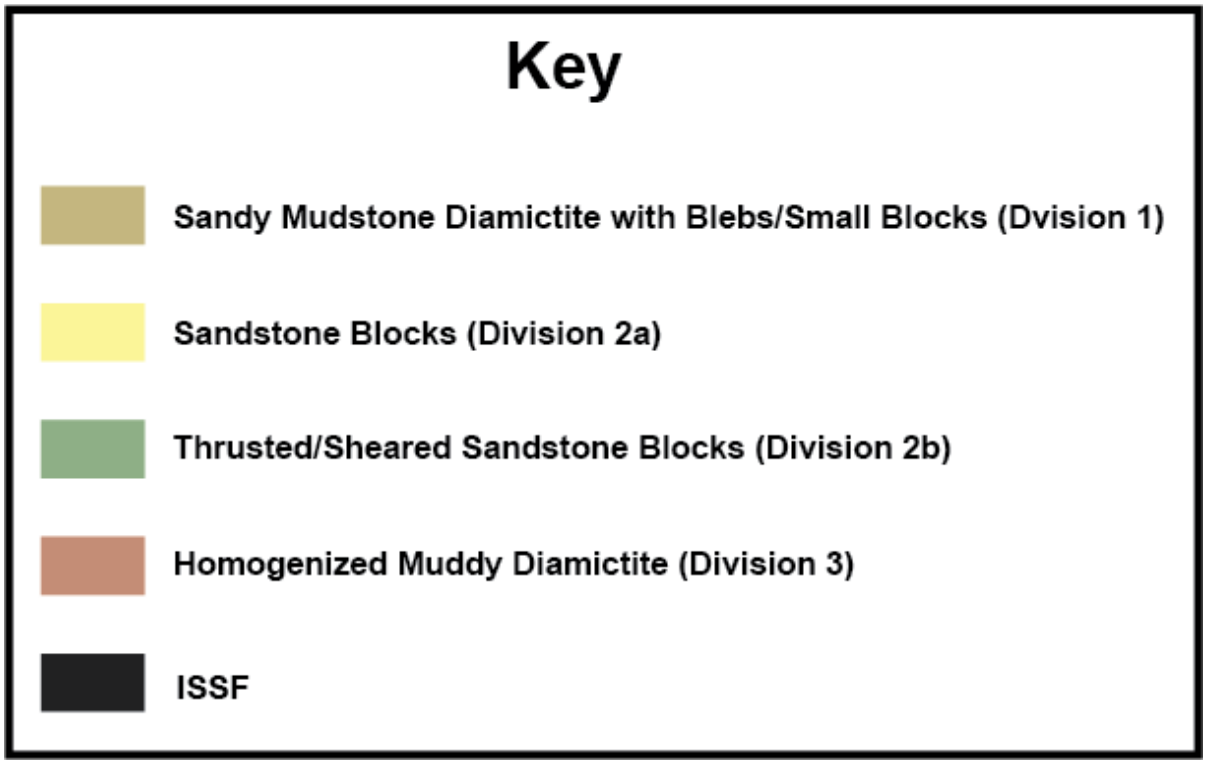

Figure 30: Key displaying the compositional and kinematic contacts between divisional units for following vertical profile figures.

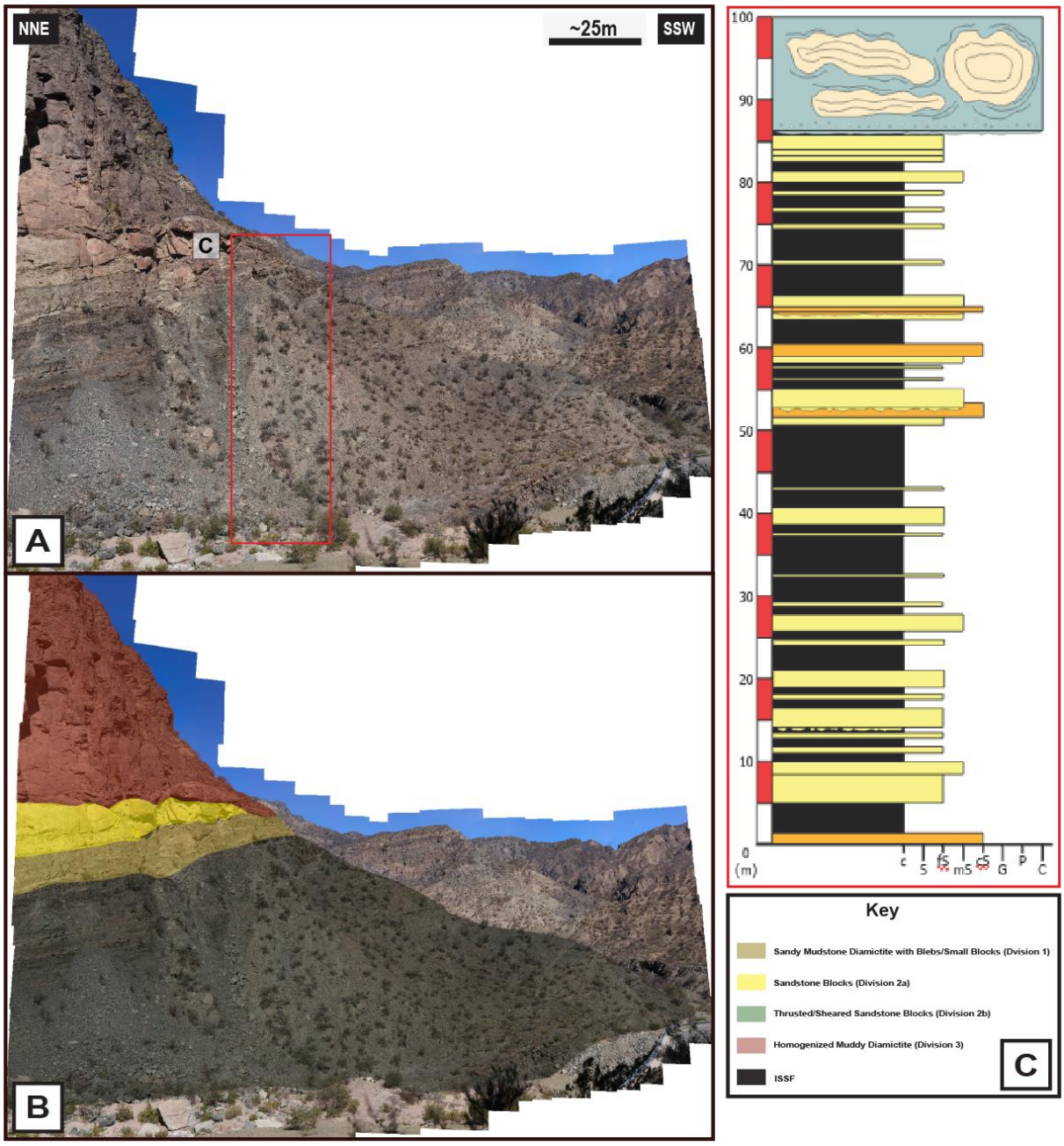

Figure 31: Section 1 locality. (A) High resolution photos of section used to observe deformation and compositional changes. (B) Outcrop annotated with divisional boundaries over the strata in this section. (C) Section 1 overlay created (see Figure 7). Key colors do not correlate with stratigraphic section.

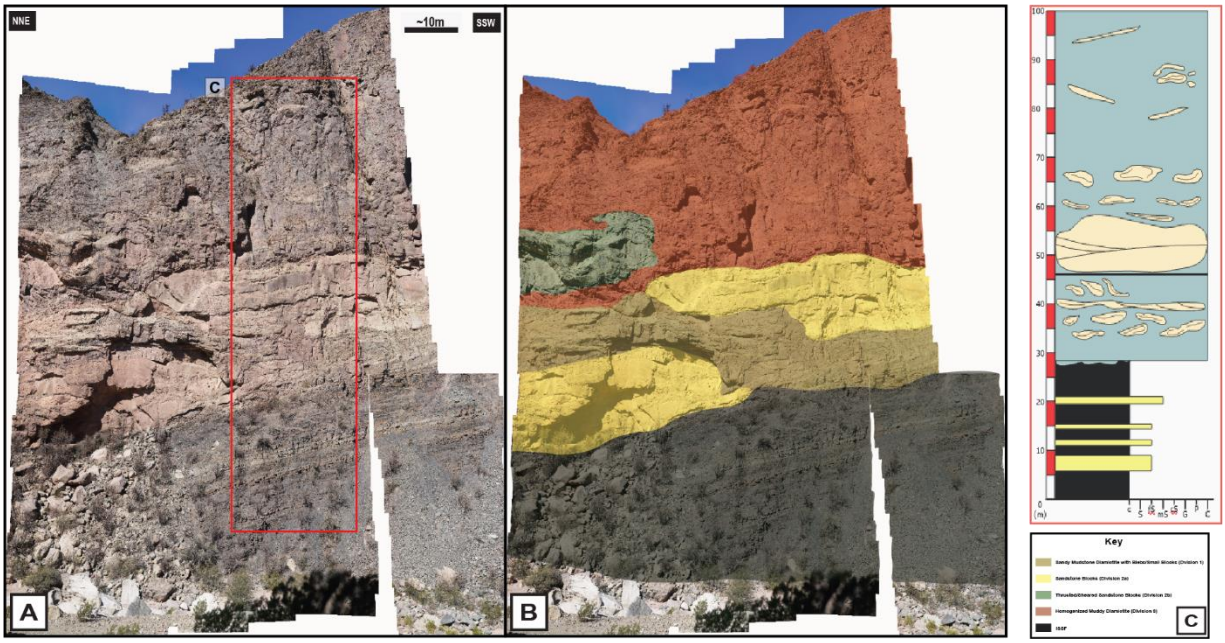

Figure 32: Section 2-3 locality, refer to Figure 30 for divisional key. (A) High resolution photos of section used to observe deformation and compositional changes. (B) Coloring of division boundaries over sections. (C) Section 3 stratigraphic section (see Figure 9). Key colors do not correlate with stratigraphic section.

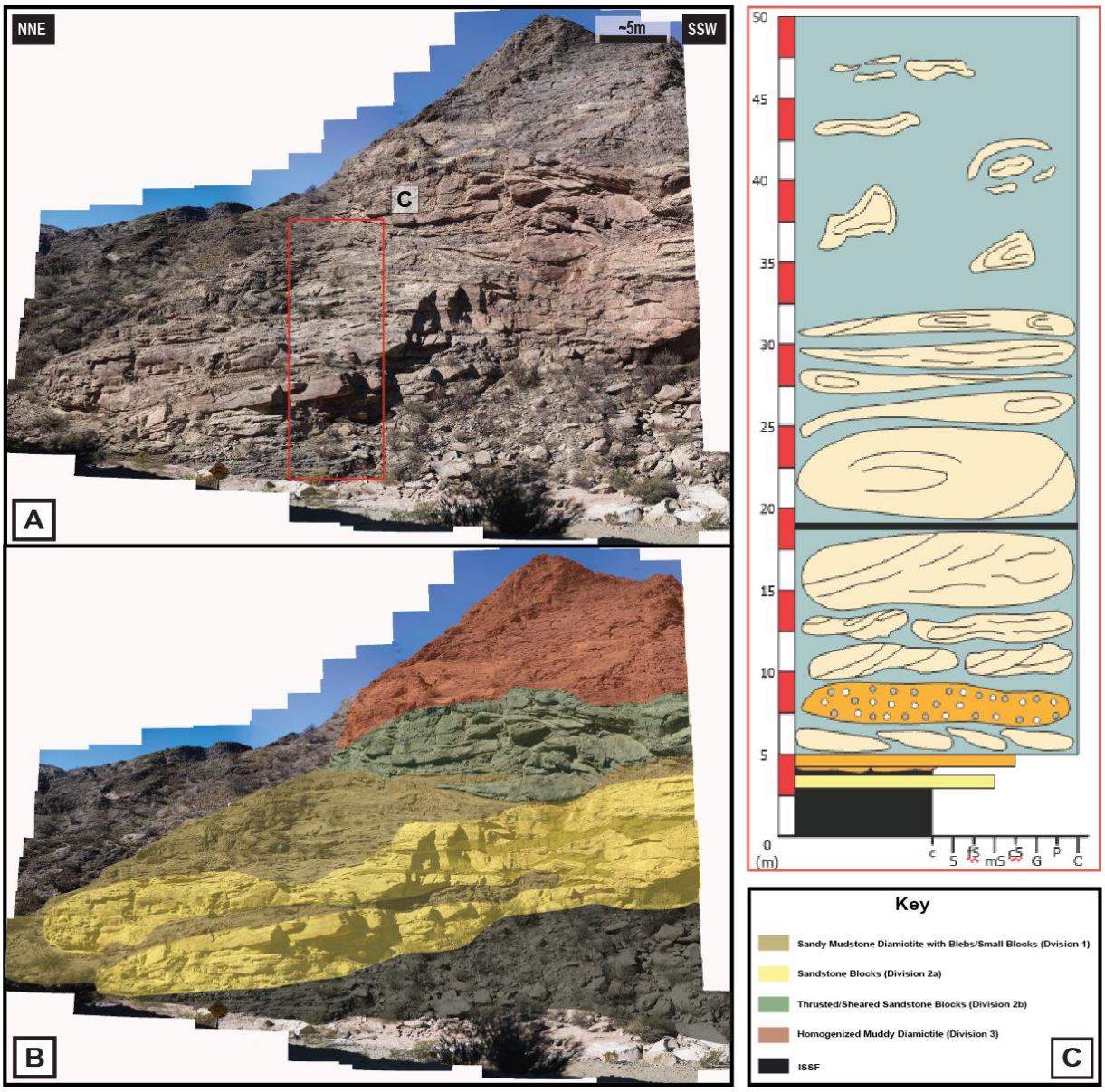

Figure 33: Section 4 locality. (A) High resolution imagery of section used to observe deformation and compositional changes. (B) Coloring of divisional boundaries over sections. (C) Section 4 stratigraphic section (see Figure 10). Key colors do not correlate with stratigraphic section.

Sandy Mudstone Diamictite with Blebs/Small Blocks (Division 1)

Division 1 (D1) overlies the BSZ near the beginning of the transect (Section 1) and displays substantial lateral and vertical variation across the outcrop. The contact between D1 and D2 is primarily sharp but has instances where there are sand/mud gradational changes. Initially,

D1 is relatively thin (5-8 m) in section 1 but thickens to the north (Section 4) up to 15 m. The matrix composition varies between mud-sand dominated compositions but predominantly consists of a sandy mudstone with dispersed intrabasinal sedimentary and igneous/metamorphic extraformational clasts (sheared diamictite).

Throughout Sections (1-2), D1 contains an assortment of small fine-medium grained sandstone blocks (1–4 m in length), as well as sand blebs and stringers (Figure 34D). Sobiesiak et al., (2016) characterizes blebs as ~5-80 cm in length, and up to 40 cm in width. They are detached bodies and indicate shear sense (Figure 14). Stringers are thin streaks of sand, < 5 cm thick, and between 2-3 m long. North towards Section 3, D1 is no longer in contact with the BSZ and is observed overlaying/overriding D2 (Figure 36A). A gradual sandy transition occurs laterally (~20-30 m) within the matrix as a contact between the two divisions. Over D2, a large deformation zone (20-25 m thick) contains small thrust sets (3-5 m thick) and lateral injections (10-15 m) into the underlying division (D2) occur (Figure 37 A-B). Other preserved structures include rollover blocks (~10 m in length & ~15 m thick) and elongated sandstone bodies 5-10 m in length & 2-3 m thick (Figure 36B-D).

Transitioning to Section 4, D1 separates into upper and lower members (Figure 35A). The lower member, occurs between the block structures of D2, exhibits a thickness of 2–3 m and is characterized by a fissile, sheared texture along both its upper and lower contacts. The upper member, reaching up to 15 m in thickness, displays a predominantly gradational contact with an underlying body of D2. North of the previously depicted deformational zone (Section 3) this upper unit contains elongated sandstone blocks varying in size, with evidence of shearing and folding. A combination of folding and shearing creates an eye shaped block. Similar structures were documented by Sobiesiak et al., (2016, 2017) from Cerro Bola. The block's long axes are

larger than the short axes and include tapered tail-like structures likely formed through the shedding and wrapping of sheared material resulting in an eye-shaped geometry (Figure 35B). Additionally, certain localities exhibit injections or fluid-flow fabrics at varying scales within the matrix (Figure 35C).

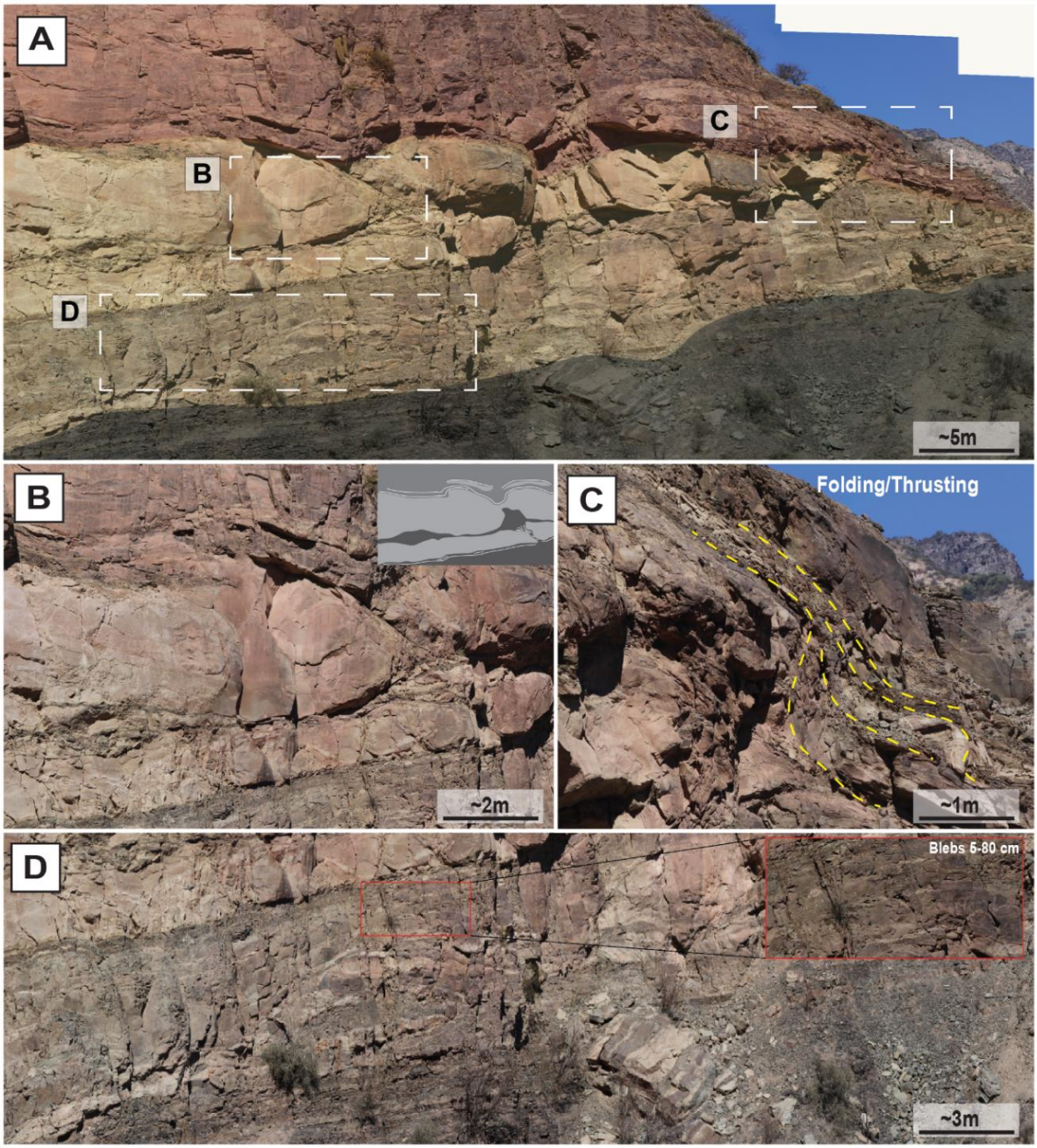

Figure 34: Section 1-2 locality, refer to Figure 30 for divisional key. (A) Contacts between D1-D2-D3. (B) D2, composed of a thick layer of interconnected fine to medium-grained sandstone blocks. Note the vertical fracturing and injection of finer material within the unit along with matrix deflection. (C) Contact between D2 and D3, where laminated mud and sand exhibit folding and thrusting around an encapsulated sandstone unit. Highly deformed sand bodies appear incorporated into the overlying mud-rich material within the transitional zone above D2. (D) D1, displaying sandstone blebs and small blocks contained within the lower mud-rich matrix.

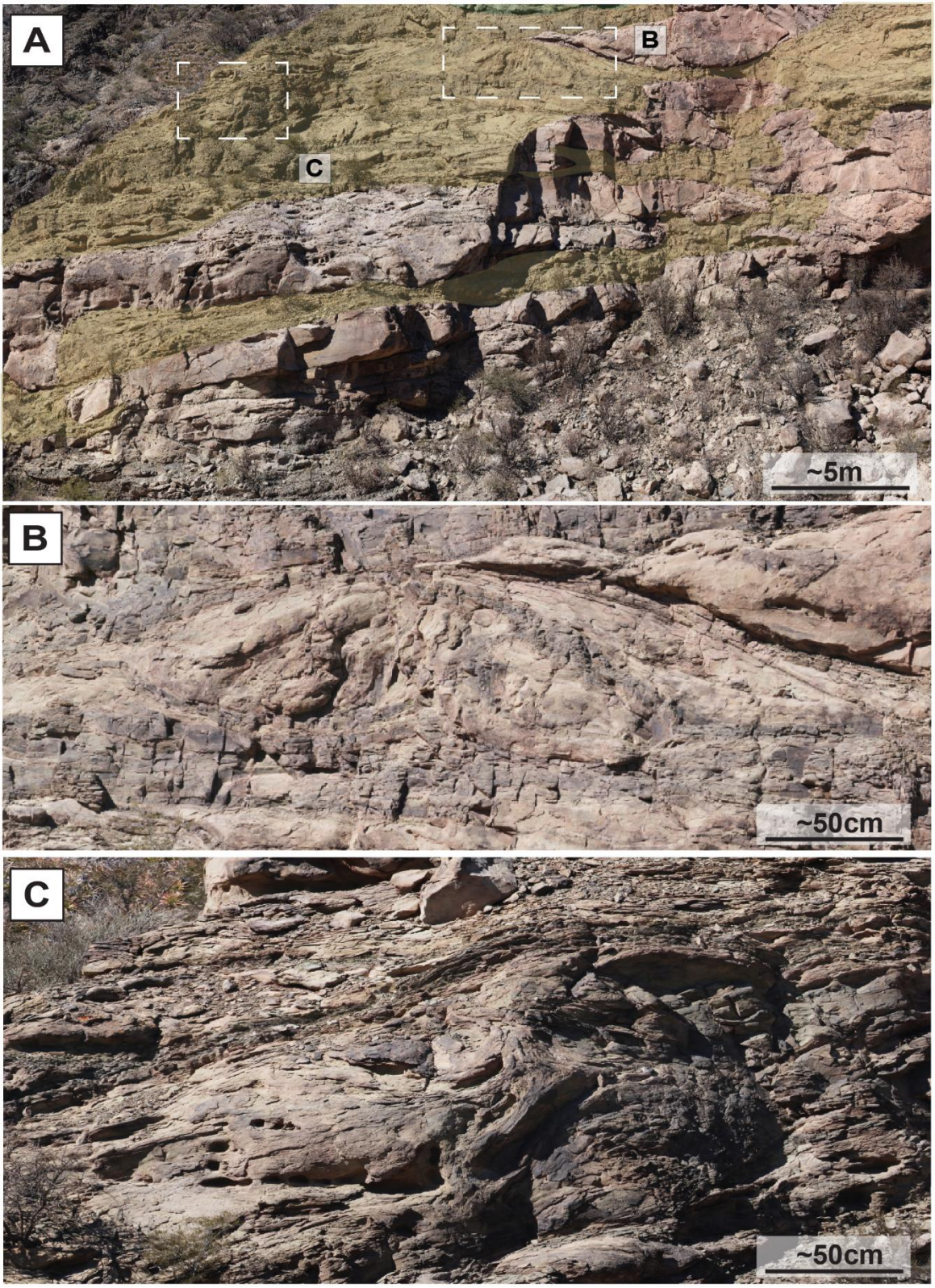

Figure 35: Section 4 locality, refer to Figure 30 for divisional key **(**A) Outlined upper and lower members of D1. (B) Eye like structure exhibiting nternal shearing and folding contained close to unit contact with sandstone block. (C) Highly deformed block with fluidized fabric forming contact with matrix of D1.

Sandstone Blocks

Division 2 (D2) ranges from approximately 3–15 m in thickness and consists of fine to medium-grained sandstone blocks varying in length from 4 to 30 m. Internal deformation within the blocks is slight to moderate throughout the transect. D2 overlays D1 sharply but transitions to a gradational contact, particularly toward the northern end of the outcrop. Across the transect, D2 is subdivided into two members: D2a, composed primarily of massive sandstone blocks and D2b, characterized by fragmented and fluidized block material.

Sections (1-3), D2a exists predominantly as a structureless sandstone block, varying 5-12 m in thickness and ~100 m in length. Intrusions of D1 matrix infiltrate into D2a laterally and vertically throughout the extent of the block (Figure 34A, 37A-B). There are small localities within blocks where water escape structures in the form of dewatering pipes and sheets occur (Figure 36E).

Between Sections 3 and 4, D2 separates into two distinct members. D2a is displaced lower within the flow along the BSZ, which forms a 15 m thickness 20–30 m long SS body. Smaller, ribboned sandstone blocks (3–4 m) with tailed structures follow the southern end of the main D2a block (Figure 36B-D). Block fracturing with matrix injections (3-4m) of D1 occur along the southern margin of D2a (Figure 34A-B). D2b exists directly above D1a and is separated by a shear zone at the top of the D1 unit. D2b preserves plastic flow fabrics to the south and transitions to a series of thrust sets that have a downdip direction in a southern direction. The smaller sandstone bodies (1-3 m in length) within the thrust sets appear stacked, compact, and fragmentated (Figure 38A-B). Additionally, the northern blocks contained within the thrust set contain boudinage tail structures that pinch out laterally towards the north. Shear fabrics and fissile matrix texture also occur along the contacts of these bodies (Figure 40A-C).

Transitioning to Section 4, D2b pinches out laterally, while D2a separates into two distinct units, with the lower unit continuing in direct contact with the BSZ. Both units exceed 50 m in length and have a maximum thickness greater than 5 m. The upper unit is predominantly massive but contains horizontal, oblique, and vertical matrix intrusions from D1, along with plastic flow fabrics. This D2a unit extends across the transect until it dips into the subsurface, where previously described fluidization structures above the BSZ in Section 4 occur (refer to Figure 25A-E). The lower unit comprises stacked sandstone blocks (1–3 m thick) that thin laterally to the north (Figure 39A). Within this unit, larger conglomeratic bodies (1–3 m thick, 2–3 m in length) exhibit both sharp and gradational contacts (Figure 41A-B). Clasts range from granule to cobble-size and consist of igneous, metamorphic, and intrabasinal sedimentary lithologies, consistent with previous observations. Additionally, both units contain localized occurrences of faint trough crossbedding (Figure 39B-C).

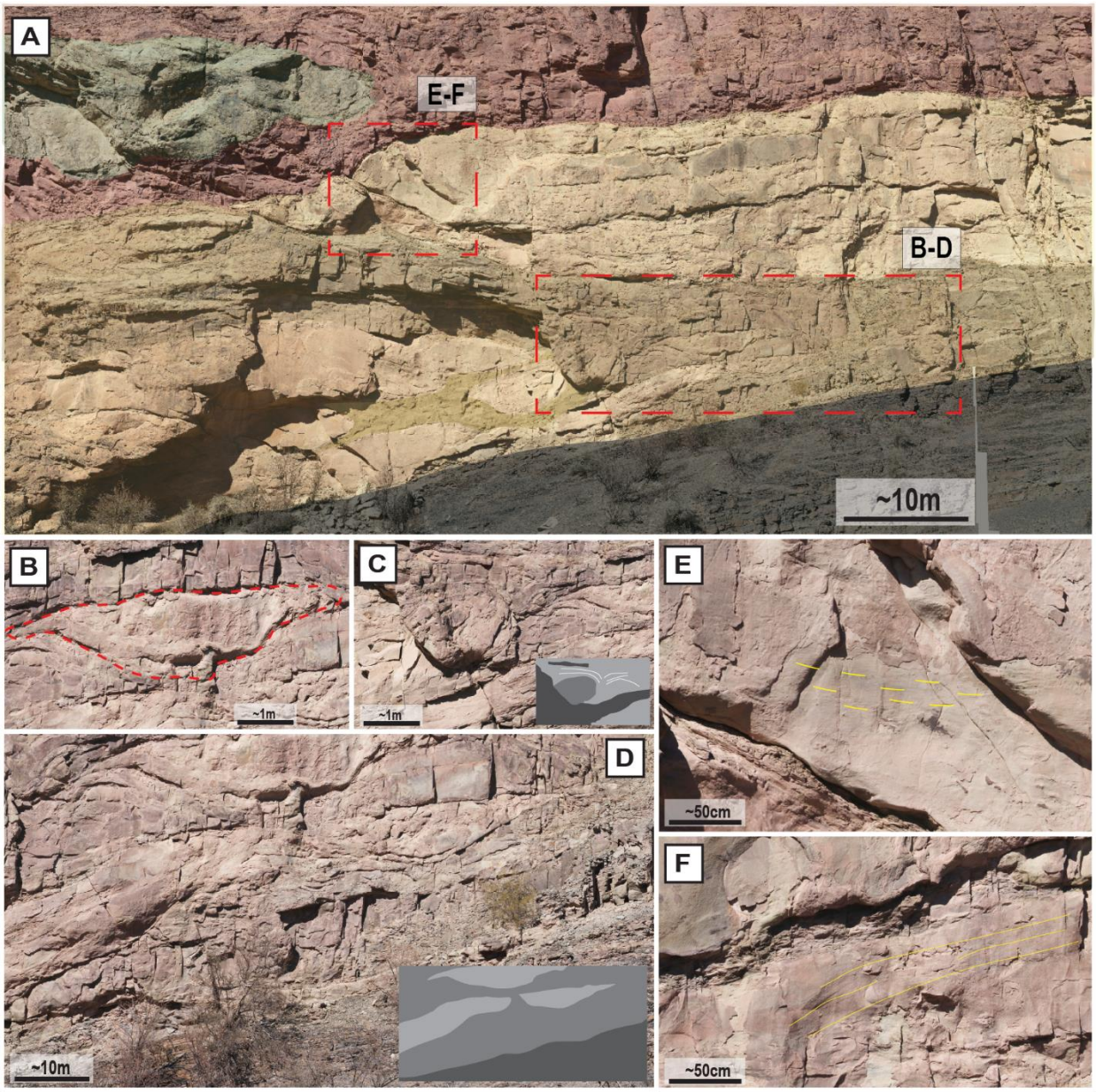

Figure 36: Section 3 locality, refer to Figure 30 for divisional key. Section 3 is largely composed of D2a, being massive sandstone blocks. **(**A) Close-up view of the transition between all three divisions (D1-D3) in the lower part of the section. (B) Sigmoidal shaped sandstone body enclosed within the matrix of D1. (C) Rollover structure with associated matrix deflection near the base of D2. (D) Tailed sandstone structures interconnected with lower body of D2. (E) Dewatering pipes near both the lower and upper sandstone boundaries; note the shear surface directly beneath the sandstone body. (F) Faintly preserved crossbedding within a localized portion of D2.

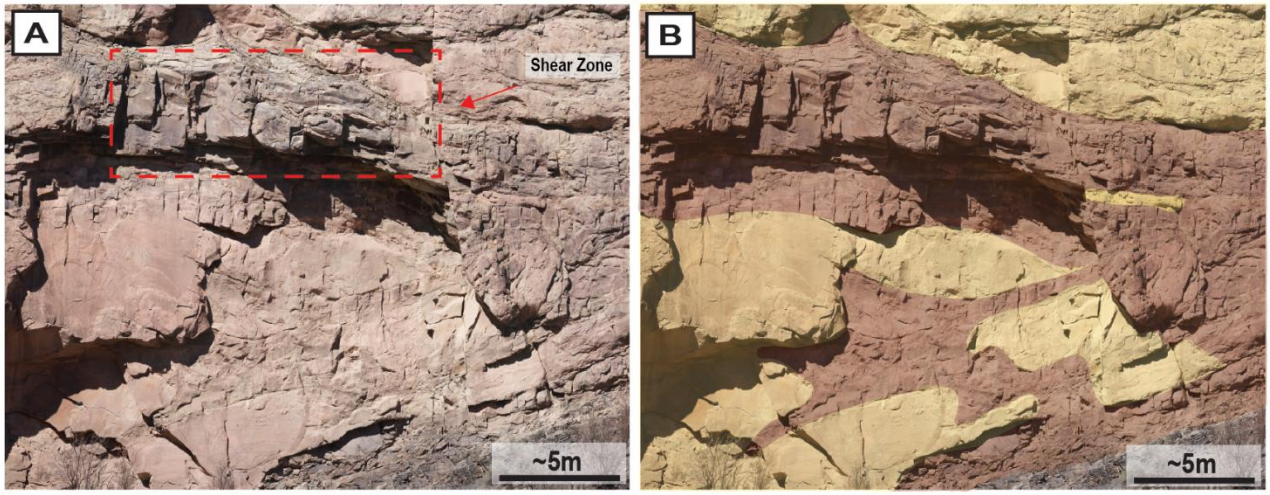

Figure 37: Section 3 locality, refer to Figure 30 for divisional key. (a) Lower block of D2 showing injections and matrix infiltration from D1. Note the shear zone above the block, where layer deflection wraps around the block (b) Enhanced image highlighting matrix infiltration across the sandstone body.

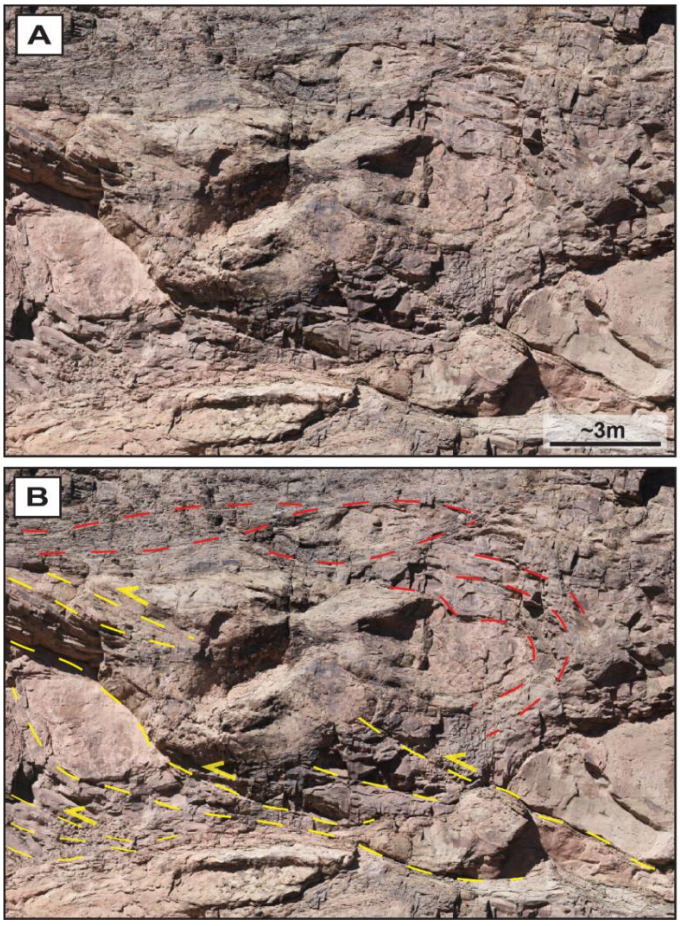

Figure 38: Section 3 locality D2b, characterized by fragmented and fluidized block material. (A) D2b showing different appearance of fluidized structure near the center of the image, transitioning to brittlely deformed thrusted material towards the north. (B) Matrix deflection outlined in red and thrust sets with a downdip direction to the south indicated in yellow.

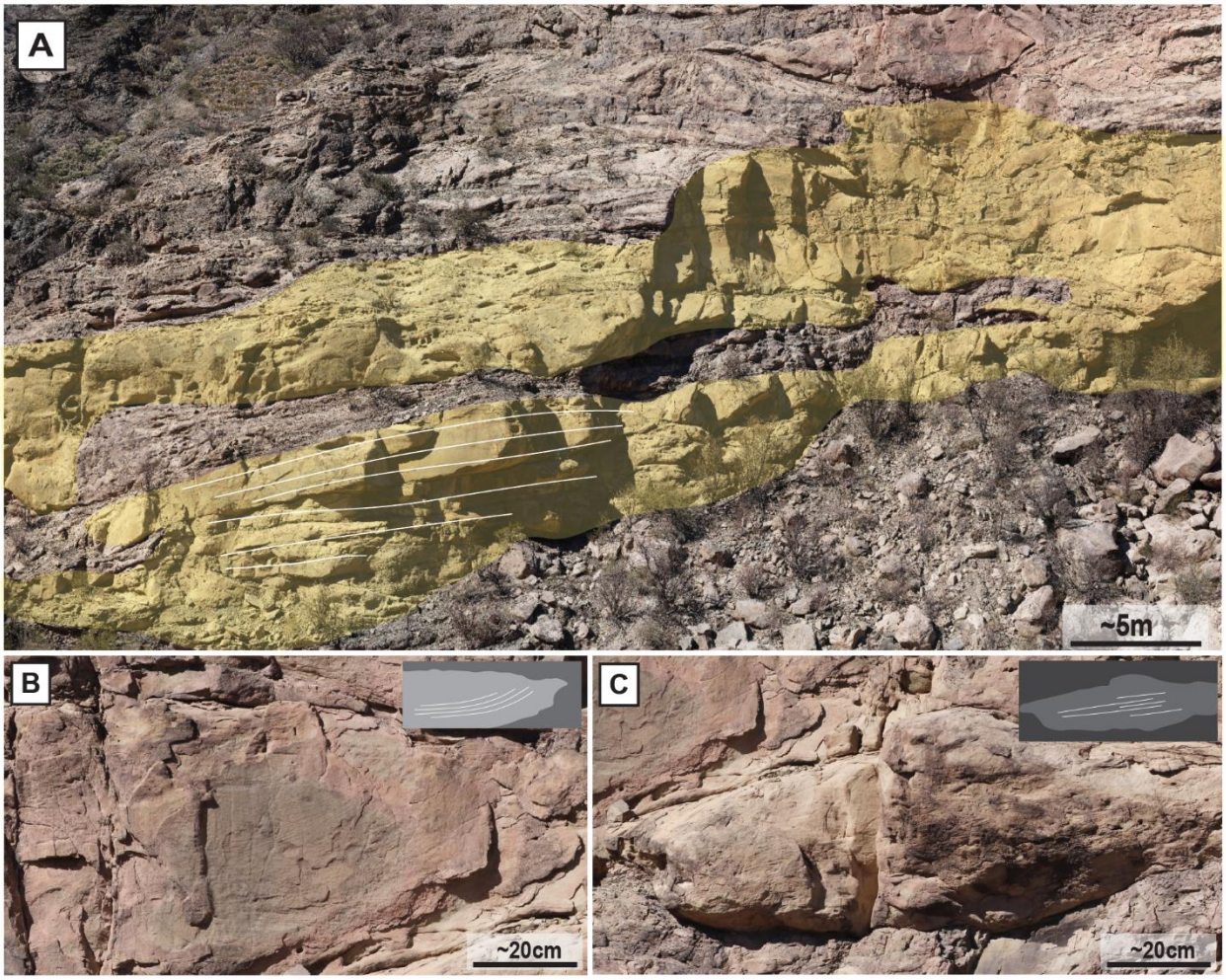

Figure 39: Section 4 locality, refer to Figure 30 for divisional key. **(**A) Outlined upper and lower members of D2a. Lower interval features lightly deformed blocks that thin laterally across the deposit with potential crossbedding. (B-C) Faint crossbedding preserved within small, undeformed blocks.

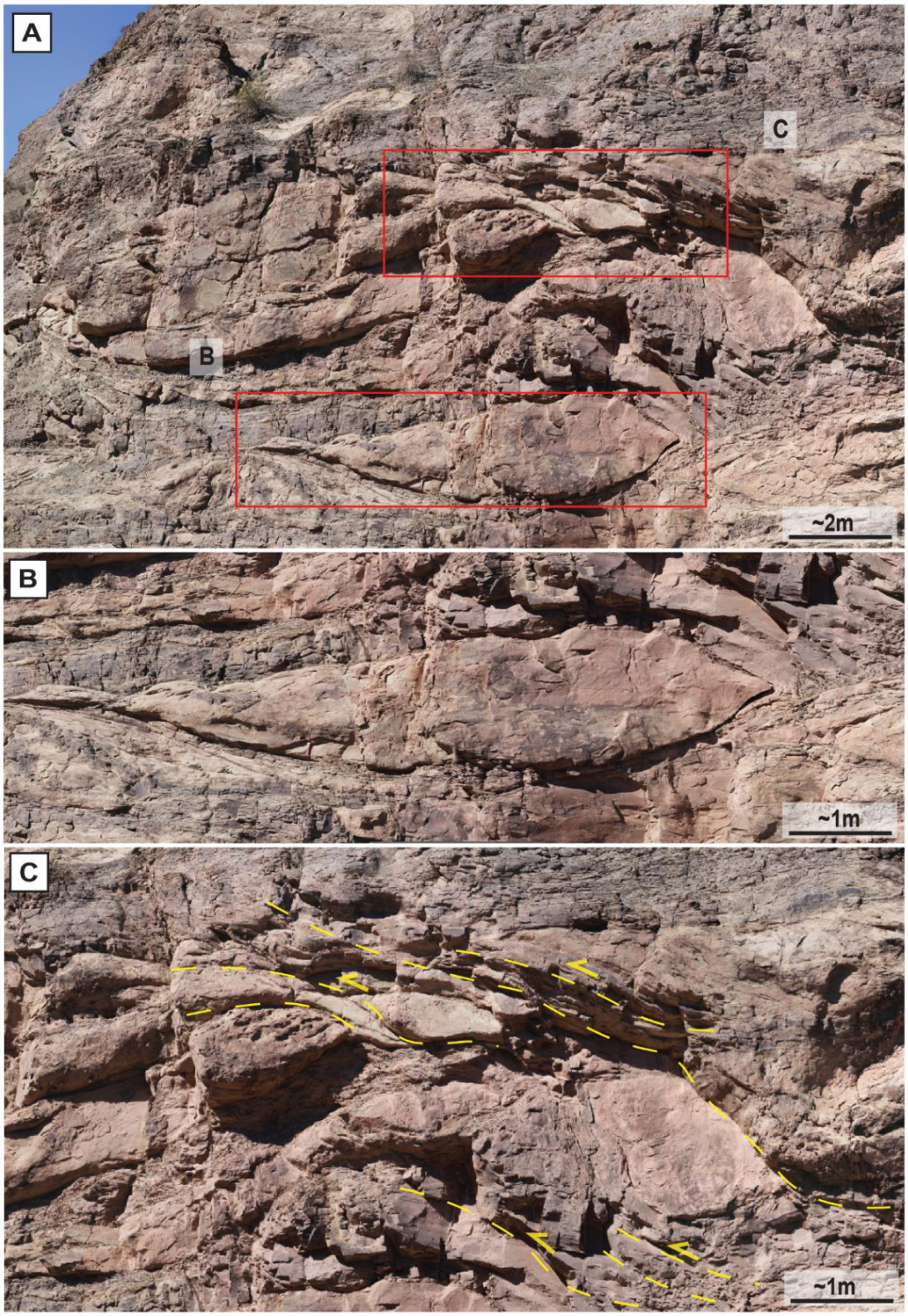

Figure 40: Section 3-4 locality (A) Final extent of D2b between stratigraphic sections. (B) Elongated sandstone bodies displaying boudinage tail structures laterally thinning toward the northern end of the flow. (C) Continuation of thrust zone showing partitioned thrusts with brecciated matrix intrusions.

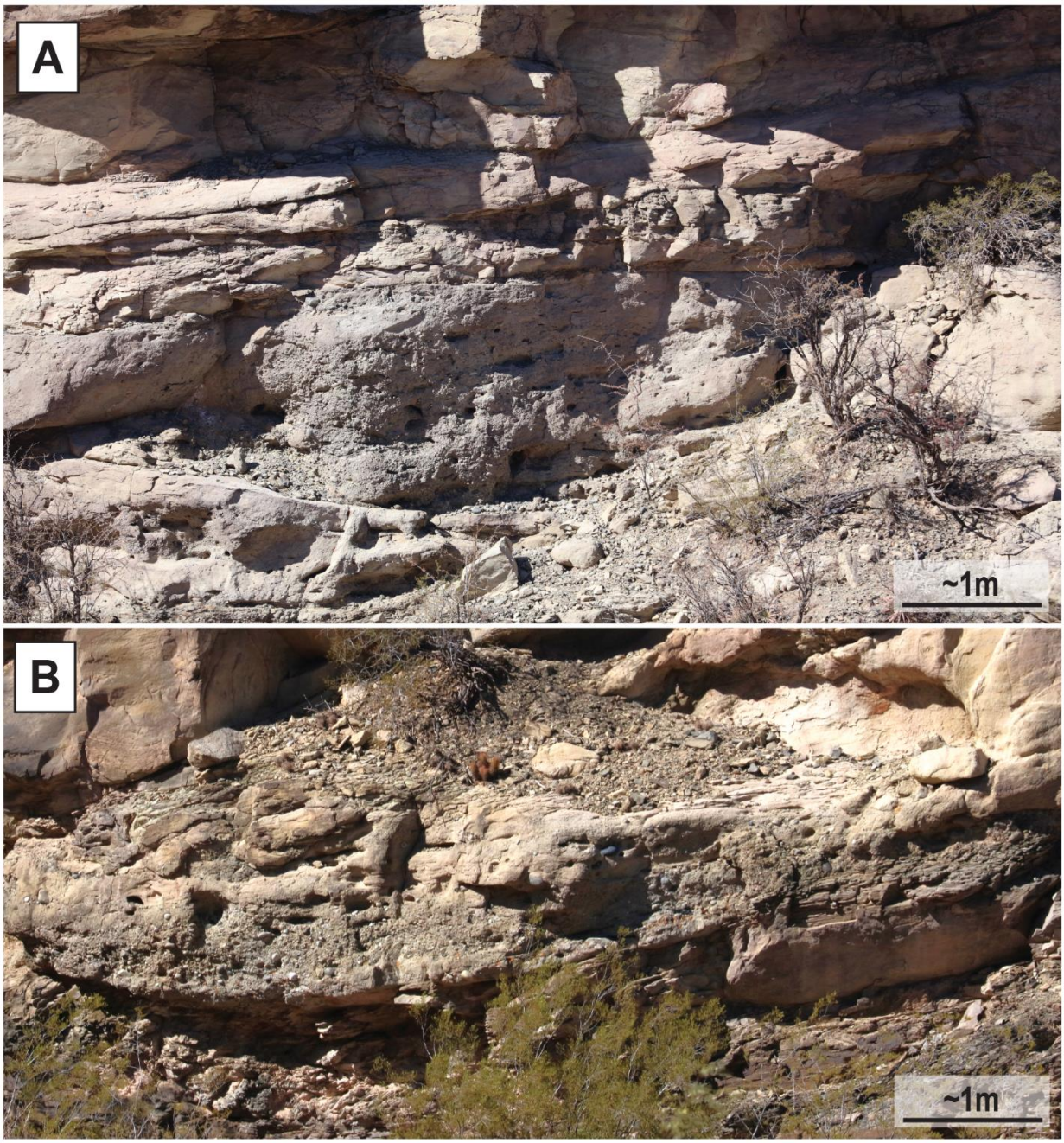

Figure 41: (A-B) Large sandy conglomerate bodies (5-10 m) observed above the BSZ (Section 4). Conglomerate primarily consists of intrabasinal sedimentary fragments and extraformational igneous and metamorphic clasts.

Homogenized Muddy Diamictite

Division 3 (D3) is the thickest divisional component, ranging from 10 to 50 m thick across the outcrop. It consists of a homogenized sandy mud matrix and forms a predominantly sharp, though occasionally gradational, contact overlying D2a and D2b. The matrix near the D2

contact commonly wraps around and deflects creating shear patterns along block boundaries (Figure 42A-B). The matrix appears fissile and includes localized areas with heterogeneously banded sand-mud patterns (Figure 44C). Within the upper half of D3, concretions are present, varying in both frequency and size. These concretions resemble those described in Cerro Bola by Sobiesiak et al. (2016), which are dark, sub-rounded, silica-cemented, and often nucleated around pebble-sized lonestones (Figure 43, 44C). Scattered throughout the D3 matrix, highly deformed blocks (~2–3 m in length, ~1–2 m thick) occur in low abundance. These blocks display rotational fabrics, internal folding, shear indicators, and tail structures (Figure 42B, 44A-B).

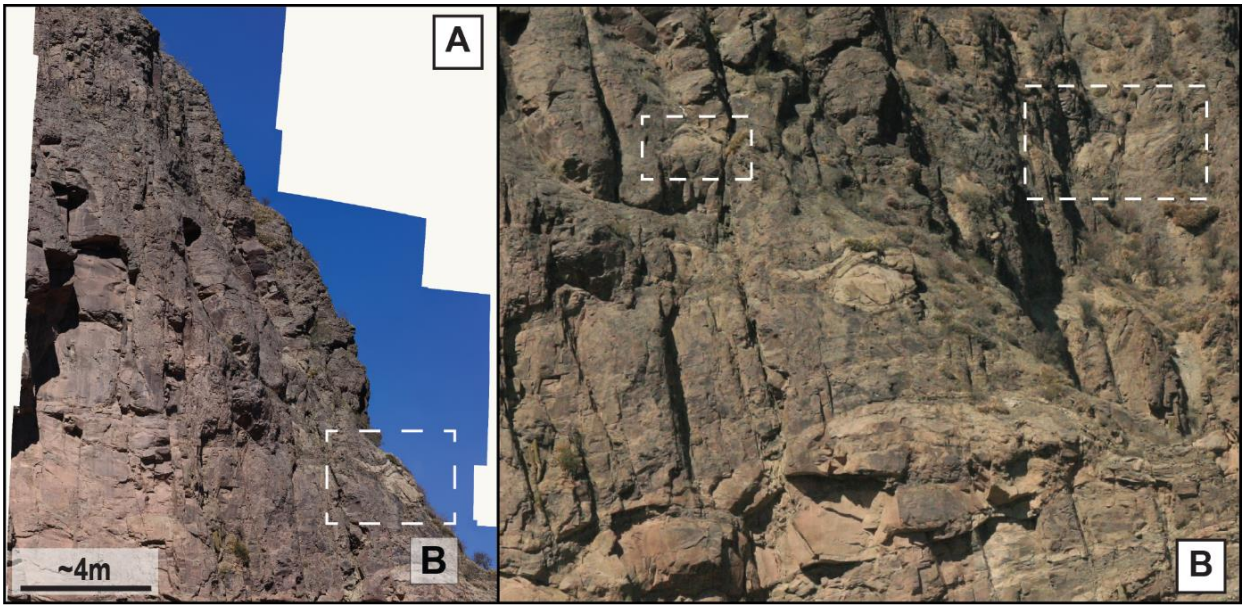

Figure 42: Section 1 locality (A) Base of D3, showing a shift from sand to mud-rich material over a short distance near the contact boundary. (B) Deformed blocks within the D3 succession. Note the eye-shaped block with tail-like features in the center of the image.

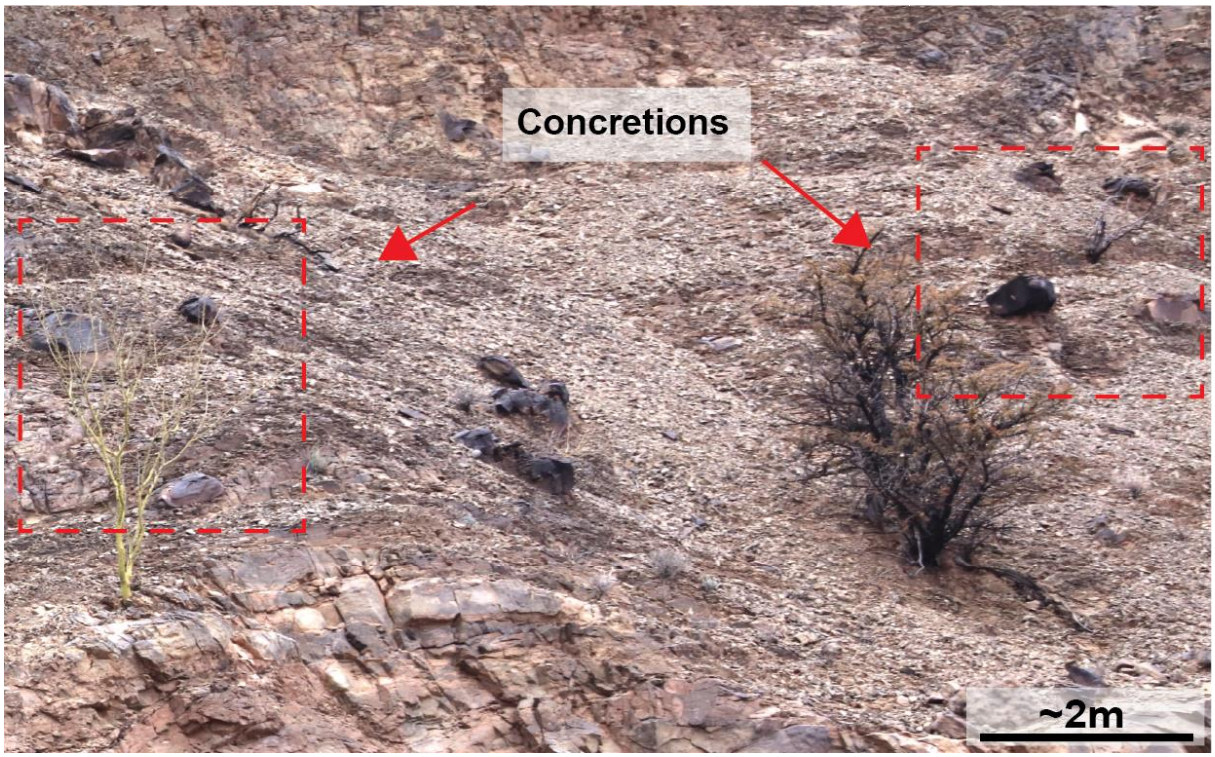

Figure 43: Concretions contained within the upper part of D3. Note the size and dark color of the present concretions.

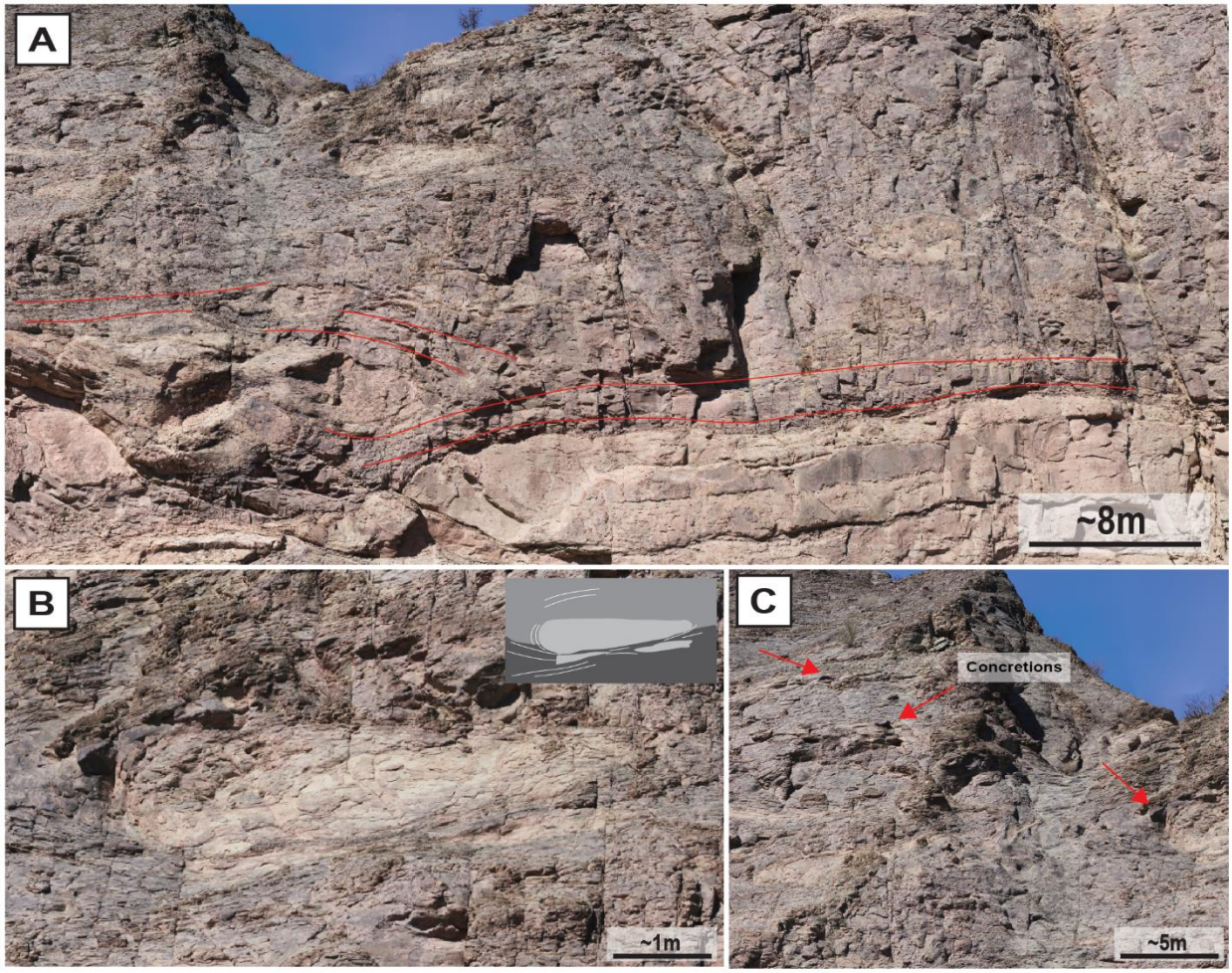

Figure 44: Section 2-3 locality (A) Overview of D3, highlighting intrusions and matrix wrapping/deflection along the boundaries of adjacent divisions. (B) Internally rotating block within the deposit, with evidence of both internal and external shearing along its perimeter. (C) Matrix exhibiting sandstone streaking and swirling near the upper part of the unit creates a rotation-like fabric. Rounded dark concretions occur within the upper part of unit.

Megabed Profile Interpretation

Previous studies of MTDs (e.g., Ogata et al., 2012; Sobiesiak et al., 2016; Fallgatter et al., 2017; Cardona et al., 2020; Rodrigues et al., 2020) report deformational change above BSZs as being gradual, with deformed blocks situated along the bottom of the flow progressing to highly deformed, homogenized matrix within the upper levels of mass transport deposits. This MTD generally aligns with previous studies on increasing vertical deformational change, but the transition appears more abrupt rather than gradational. The contacts between divisions remain mostly sharp due to the presence of large, slightly deformed blocks that have undergone minimal

disaggregation during flow transport. Some studies suggest the existence of blocks with such large sizes are linked to seismic activity resulting in slope failure as a source of deposition (e.g. Fossen, 2010; Alves & Elliot, 2014; Quirk et al., 2012; Alves, 2012, 2015). Reasoning for the coherent, undeformed nature of these blocks could result from a combination of proposed characteristics.

1. **Short transport distance from a headwall scarp area within extensional flow regime:** Large displaced blocks can be fairly common within a close proximity of the headwall regions of an MTD (Figure 45). These blocks form around the boundary of these escarpments and are a result from younger failure following a larger mass-wasting event (Bull et al., 2009; Alves, 2015). Poorly displaced blocks are a product of a more local failure of subsequent flow and do not progress to the dynamic level of the main slide (Kvalstad et al., 2005). Furthermore, the headwall is associated with an extensional morphodomain containing deformation in the form of normal faulting and boudinage (Cardona et al., 2020). A lack of compressional force may play a role in the coherency of the block material.
2. **Shear stress associated with block proximity of BSZ:** The BSZ is predominantly thin and erosive. While signs of strain are present, the stress near this locality may not have been sufficient to disrupt large volumes of entrained blocks higher within the flow. Basal zones are often linked to a more coherent flow where upper flow domains are subject to more chaotic flow resulting in more disaggregation (Ogata et al., 2012; Fallgatter et al., 2017; Cardona et al., 2020; Rodrigues et al., 2020).
3. **Lower flow stress regimes:** Compressional and extensional domains created through variation of seafloor topography and interaction of material entrained within flow can

cause disaggregation of blocks (Kvalstad et al., 2005; Bull et al., 2009; Alves & Cartwright, 2010; Alves & Lourenço, 2010; Alves et al., 2012, 2015). Limited exposure to extensional and compressional forces throughout a localized flow path could preserve the coherent blocks within the flow.

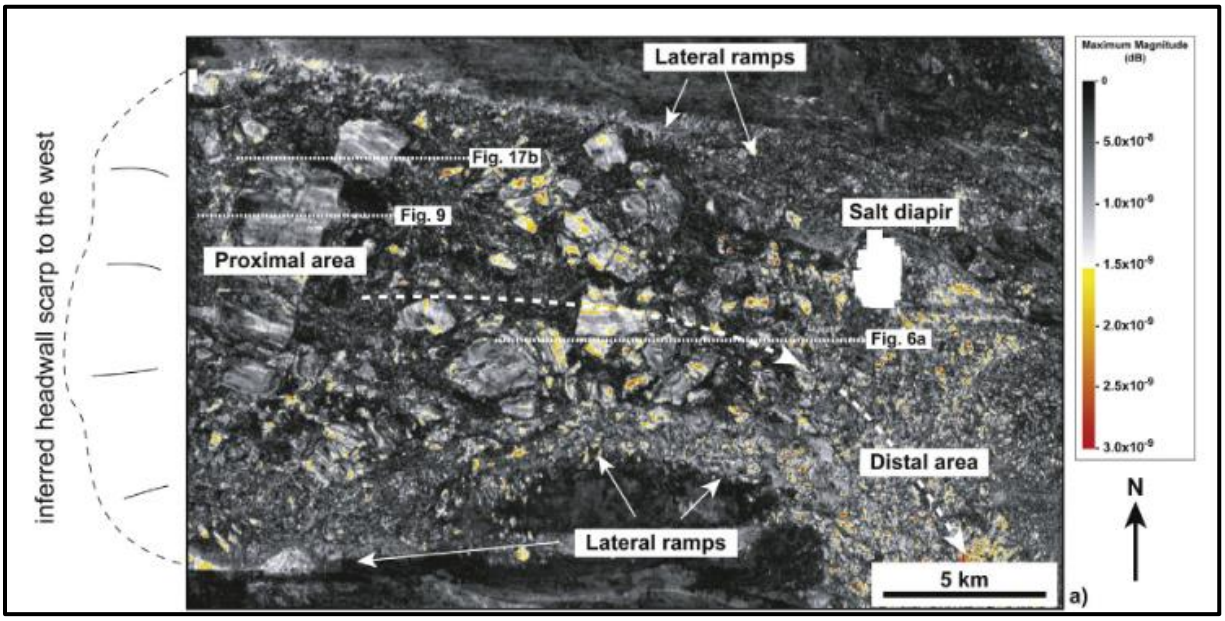

Figure 45: 3D seismic image shows mass transport collapse with respective distance from headwall/escarpment. Note how larger blocks are concentrated closer to the inferred headwall. Originally from Chang et al., (1992), modified by Alves, (2010).

Kinematically, the studied flow is interpreted to exhibit a surging behavior. Surging flows typically display sharp contacts, evidenced differences in velocity between units, erosional surfaces, and shear zones related to block settling and pulsating force (Middleton, 1966; Martinsen, 1994; Mulder & Alexander, 2001; Bull et al., 2009). De Blasio et al. (2006) describe how blocks within mass transport deposits can decelerate due to erosive flow drag and interaction with the seafloor. Block deceleration within the deposit occurs through matrix thrusting and shear deflection around D2 contacts (Figure 38A-B, 40A-C, 44A). This study suggests that coherent blocks within D2a settled as a result of flow drag or basal erosion, while

the surrounding matrix components of D1 and D3 continued moving, leading to the observed matrix deflection and thrust development along block contacts. Additionally, the thrusted blocks observed in D2b are likely the product of material thrusted over deposited stationary blocks as seen near Section 3.

Multiple types of deformation occur across the studied outcrop, with particularly complex features between Sections 3 and 4. This study suggests that a compressional domain developed due to a grounded block (Figure 41A-B), which acted as an obstacle, causing flow material to ramp over it. Similar ramp-related deformation has been documented in other studies (e.g., Bull et al., 2009; Lackey et al., 2018; Lucente, 2003; Sobiesiak et al., 2017), where high deformational variability and abundant kinematic indicators were observed. Above the contact with the grounded block, D1 exhibits thrusting and shearing between the D2a and D2b members (Figure 36A, 37A-B). Likewise, the D2b member displays evidence of compressional strain, including thrust faulting, fragmentation, and brecciation (Figure 38A-B, 40A-C). These observations suggest that D2b existed as a suspended block within the flow and was thrust over the grounded block simultaneously with the D1 interval. The thrust sets preserved within the two intervals display a down-dip direction to the south, indicating flow direction to the north.

Another notable aspect of block degeneration is contained within D2a (Sections 3–4), where the infiltration of D1 matrix disrupts block structure and leads to fragmentation (Figure 37A-B, 39A). Separation and fragmentation occur at varying scales and are proposed to result from a combination of two processes.

1. **Interaction with the BSZ:** Due to the high stress conditions and unique characteristics of the BSZ, several mechanisms may contribute to block

fragmentation. a) The BSZ experiences significant stress and it typically diminishes throughout the vertical profile (Cardona et al., 2020; Rodrigues et al., 2020), potentially creating differential stress zones that promote block separation. b) Direct collision of blocks with the BSZ may generate localized penetrative stress, leading to fragmentation (Alves & Lourenço, 2010). c) Interaction between sliding blocks and seafloor topography can induce disruptive stress, further contributing to block disaggregation. d) In water-saturated conditions, drag forces exerted on sliding blocks may create differential velocity gradients. The lower portion of a block, in direct contact with the BSZ, experiences greater resistance and slows down, while the upper portion remains relatively unaffected. This velocity contrast could generate a drag fault, leading to block separation.

2. **Divisional flow collision:** Grounded blocks deposited prior to final flow emplacement can act as obstacles, influencing subsequent flow dynamics. While ongoing flow typically diverts around these blocks, this study suggests that direct flow-block interactions can lead to disaggregation and separation, particularly when the blocks are internally fluidized. Figure (37A-B) illustrates how the D1 matrix both circumvents and fragments the D2b blocks, with lateral injections occurring as a result of flow collision.
3. **Divisional velocity contrasts:** Velocity contrasts within the different divisions can generate significant internal strain (Alsop & Holdsworth, 1993, 2007; De Blasio et al., 2006; Sobiesiak et al., 2017), leading to block disaggregation. As faster-moving material overtakes slower-moving zones, differential motion promotes deformation along block margins, fracturing, and internal deformation. These processes are

especially pronounced along shear zones and at the boundaries between coherent and more ductile or fragmented domains.

Determining the source environment of sediment entrained or protoliths within mass transport deposits is often challenging due to the degree of disaggregation. Previous studies in the Agua de la Peña and Cerro Bola localities suggest that some entrained blocks originated from fluviodeltaic sandstones, as inferred from erosional features, petrographic analyses, and sandstone body geometries (e.g., Sobiesiak et al., 2017; Spalletti et al., 2023). Figure 39A, illustrates previously described stacked sandstone bodies that laterally pinch out within the succession. These bodies may correspond to partial clinoforms associated with deltaic deposition. Clinoforms are sedimentary packages that prograde into a basin over time. They thin and fine in the basinward direction (Coe et al., 2005; Catuneanu, 2022; Anell, 2024). They may exhibit a topset-foreset-bottomset structure, are composed of thinly bedded material, and develop at various scales due to prograding sediment supply from dilute underflows and turbidity currents (Sohn, 1997; Porębski & Steel, 2003; Dixon et al., 2013; Steel et al., 2013; Anell, 2024). The observed crossbedding contained internal within these sandstone bodies (Figure 39B-C) may represent relict foresets or bedforms preserved within the clinoforms. Although uncommon, Moscardelli & Wood (2008) describe how foresets within mass transport deposits are frequently disrupted, exhibiting lateral truncation, fluidization, or rotation due to post-depositional deformation.

5). Hm to km-scale Lateral Variation

Several outcrop studies have examined vertical variations in deformation within stratigraphic successions. However, field investigations into the lateral variability of composition

and deformation in mass transport deposits (MTDs) remain limited due to the scarcity of continuous exposure. Seismic surveys and digital elevation models have been used to document lateral changes over large distances (e.g., McAdoo et al., 2000; Moscardelli et al., 2006; Bull et al., 2009; Alves, 2015; Lackey et al., 2018; Valdez Buso et al., 2024; Caradonna et al., 2025), but they lack the resolution needed to capture small-scale deformation features and are often restricted to submerged marine environments. At Agua de la Peña Creek, previous studies (e.g. Milana et al., 2010; Sobiesiak et al., 2017; Busco et al., 2019) and the kinematic indicators preserved within this deposit assume a flow direction/paleoslope to the NNW-NNE The extensive oblique exposure due to creek incision provides a unique opportunity to examine both localized and broad changes within the sediment gravity flow.

Localized Lateral Changes (100s m scale)

Compensational Stacking

DESCRIPTION: At locality B6, multiple fine- to medium-grained sandstone blocks (~5–15 m wide, ~3–10 m in height) are stacked lateral next to and on top of one another, separated by thin intervals of matrix that vertically partition the succession. The matrix consists of a sandy mudstone and is deflected in various directions around the margins of the sandstone blocks. Fissile shear textures and foliation are observed within these deflected zones. Matrix-filled gaps between blocks range from approximately 0.10 to 0.25 m in thickness (Figure 46A).

INTERPRETATION: Compensational stacking describes the tendency of flow-event deposits to preferentially fill topographic lows, reducing relief in areas where localized accommodation is present. This process has been attributed to the continuous or periodic reorganization of sediment transport systems to minimize potential energy associated with

elevation gradients (Mutti & Normark, 1987; Stow & Johansson, 2000; Straub et al., 2009). In the context of mass transport deposits, this study links compensational stacking to the emplacement of flow matrix between decelerating blocks during deposition (Locality B6). The denser block material settles first, forming topographic highs within the evolving mass transport depositional structure. While more fluidized, less viscous matrix continues to flow, filling topographic lows and wrapping around previously emplaced blocks, leading to localized deflection. As accommodation space is progressively filled, the differential deposition of blocks at varying rates results in a distinct stacking sequence. Variations in matrix deflection along block margins suggest differences in the timing of block emplacement, showing differences in depositional timing within a singular flow. (Figure 46A-B).

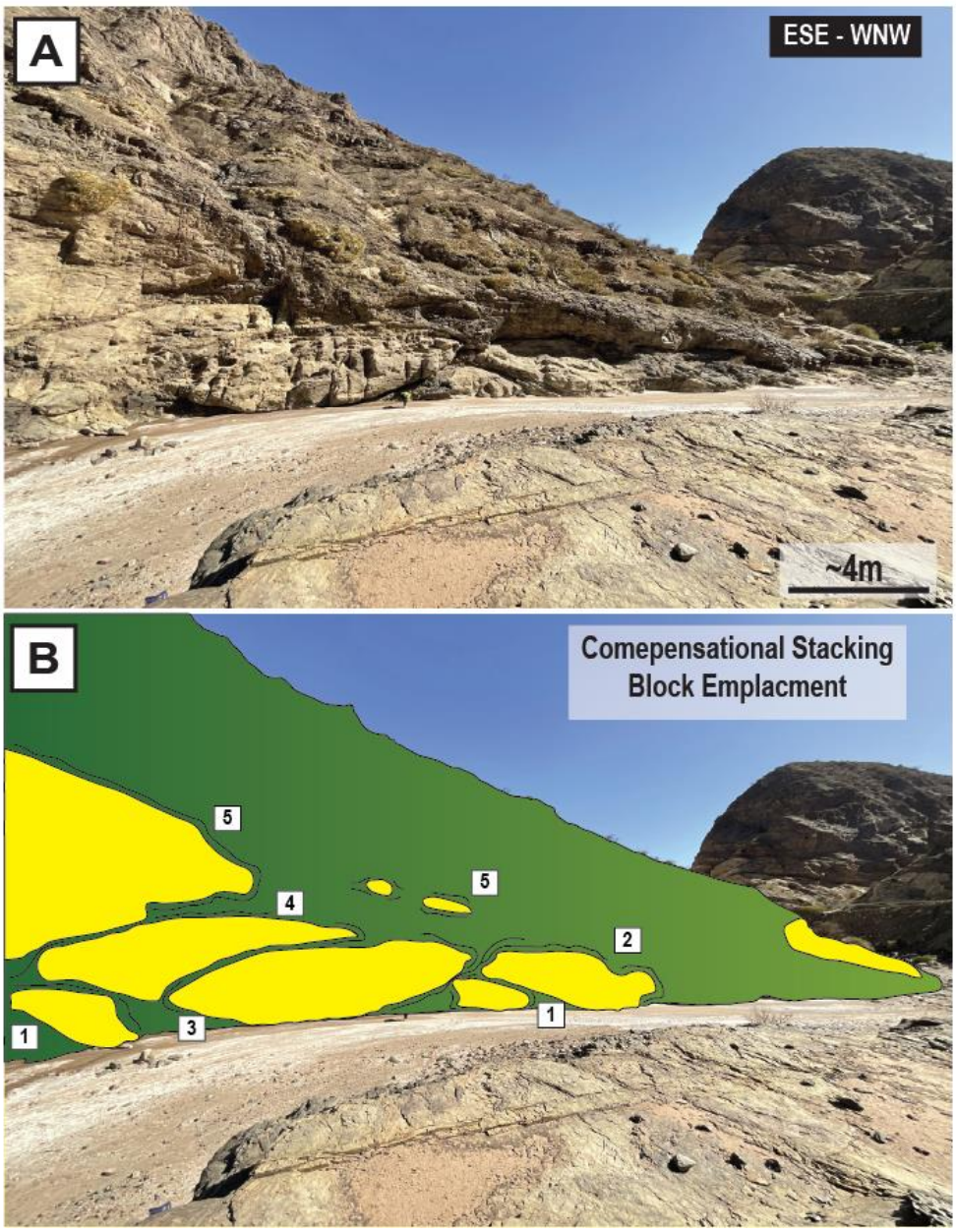

Figure 46: (A) Image of several large blocks exhibiting compensational stacking. Note variations in matrix deflection along block contacts, where underlying relief influences the geometry and thickness of overlying units. Blocks are offset laterally, with finer-grained matrix infilling topographic lows between adjacent blocks. (B) Cartoon depicting compensational stacking to help define block boundaries.

Block Deflection

DESCRIPTION: Locality B7 exposes a 35-40-m-thick interval of moderately deformed, fine- to medium-grained sandstone blocks (3–5 m in length, 2–4 m in height) suspended within a sandy-mud matrix. Many blocks exhibit marginal shearing and tapered tails, with several tails

fully detached from their parent blocks. These detached fragments remain aligned with the shear orientation extending from the block ends. In some cases, matrix infiltration has entered into the blocks, producing a split or segmented appearance. Internal folding is also present within certain blocks. Additionally, matrix pockets between blocks locally display pronounced thrust structures and shearing fabrics throughout the exposure.

INTERPRETATION: As blocks undergo rotation during downslope transport, they generate zones of differential stress that influence the rheological behavior of the surrounding sediment matrix (Locality B7). The resulting shearing and displacement induce localized strain, leading to the development of deformed fabrics, shear bands, matrix thrusting, and disrupted bedding within the matrix. When blocks rotate at varying rates or in different directions, complex strain patterns emerge, often producing localized folding, stretching, or injection of finer-grained matrix into adjacent void spaces (Figure 47A-B). Previous studies have documented block-induced matrix deformation, highlighting significance in MTD dynamics (Ogata et al., 2012; Alves, 2015; Buso et al., 2019; Rodrigues et al., 2020).

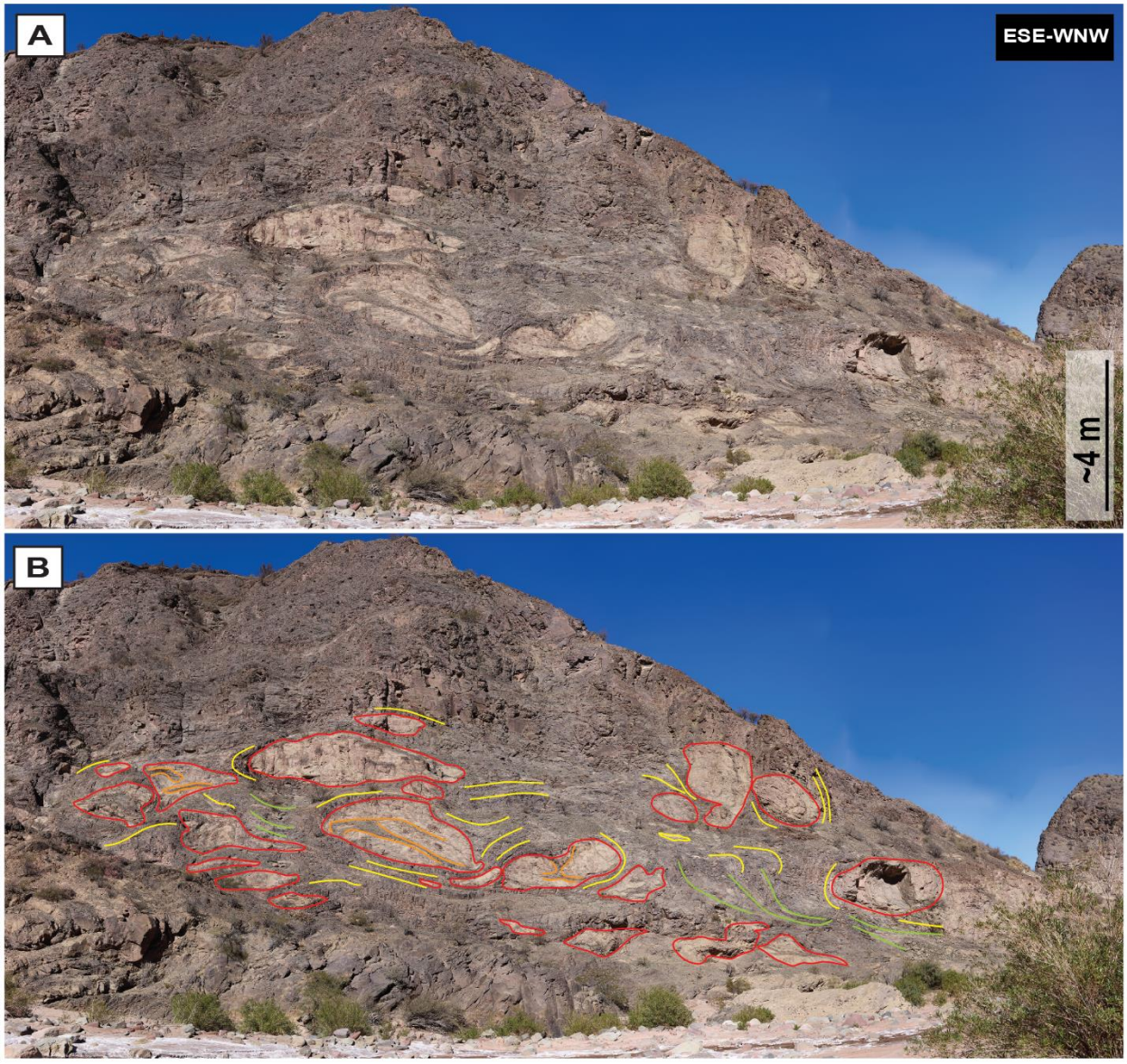

Figure 47: (A) Outcrop photo at site B7. (B) Highly deformed blocks (red) exhibit internal shear fabrics and deflection of surrounding matrix material (yellow), likely resulting from rotational deformation during transport. Internal shearing within blocks (orange) and thrusts in the matrix (green) are also present. The orientation of thrust structures indicates a downdip transport direction toward the west, suggesting an overall easterly-directed flow.

Spiral Fold/Easterly Flow Direction

DESCIPTION: Locality B8 exposes a series of elongate sandstone blocks (> 100 m in length and > 15 m in thickness) embedded within the mass transport deposit. One prominent block displays a cylindrical fold at one end (Figure 48A). The fold is large-scale and situated at the lateral margin of the block, and the surrounding beds appear wrapped around it. Thrust faults

are also present, with several developing on the downslope-facing side of the fold. The downdip directions of these thrusts yield a westerly direction and truncate the internal bedding extending large lengths (~ 15 m) across the block.

INTERPRETATION: The cylindrical fold observed at B8 closely resembles structures described by Allsop & Marco (2013), where cylindrical folds evolve into spiral folds during progressive downslope deformation. In such cases, steep extensional faults in the upper limb of the fold rotate and flatten around the hinge as the fold migrates downslope, creating a spiral geometry. The wrapping of beds around the sandstone block at B8 is interpreted as the result of this process. Although the spiral geometry is not fully developed at this locality, the orientation of the fold hinges—maintaining a high angle to bedding and slope-parallel movement—suggests downslope-directed transport. The associated thrusts likely formed as overlying strata were forced over the fold hinge. Together, the spiral-like folding and thrust orientations indicate that flow at this site shifted toward an easterly direction during emplacement.

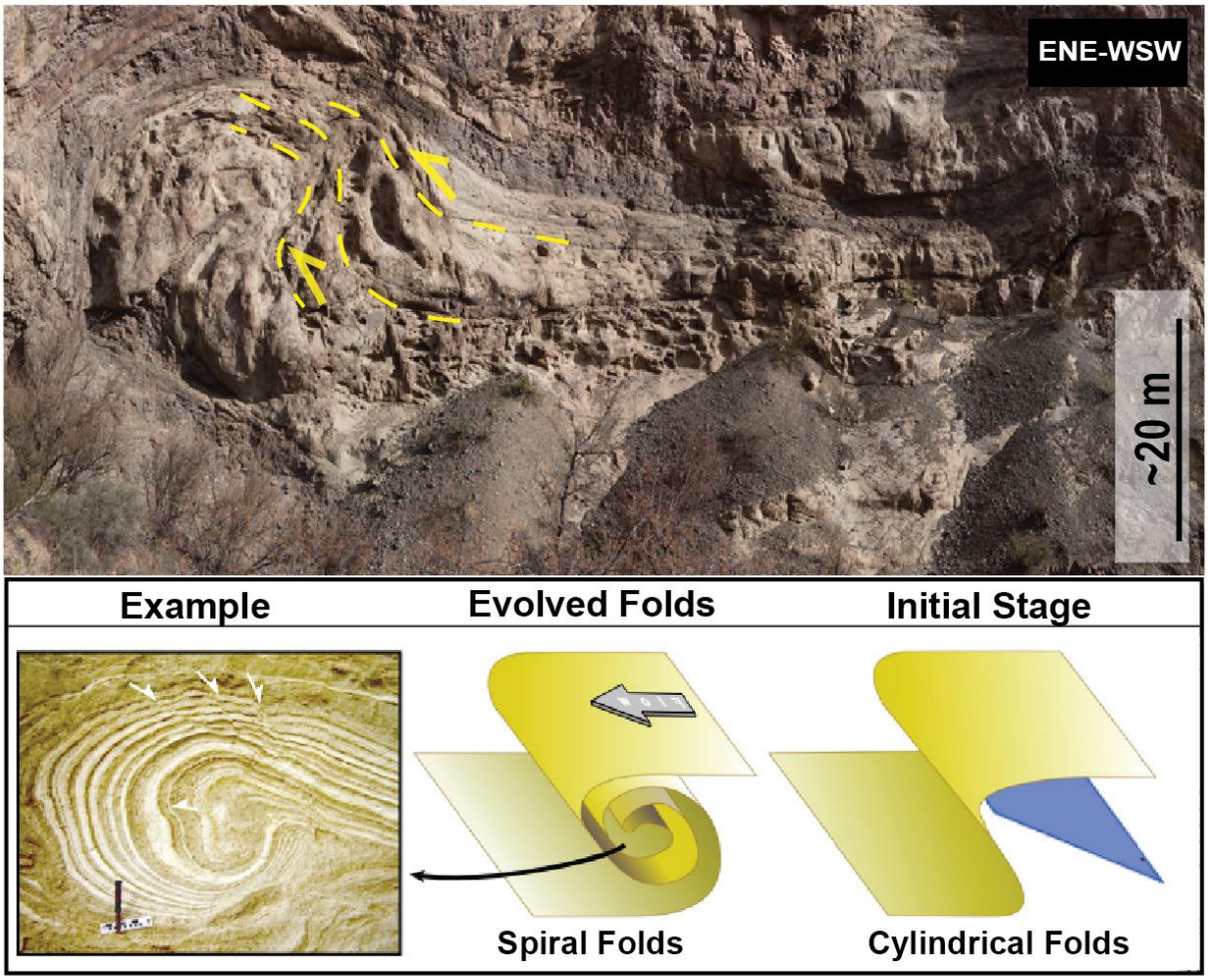

Figure 48: (A) Exposure of a cylindrical fold at site B8. (B) Illustration of a rolling fold hinge model, where a cylindrical fold transitions into a spiral fold. The spiral fold in Agua de la Peña consists of a block that contains thrusts on the back side of the fold. These thrusts suggest a change to an easterly flow direction. Adapted from Allsop & Marco (2013).

Broad Lateral Variability (km-scale)

DESCRIPTION: To investigate changes in block abundance and deformation over larger distances, this study investigated a 1 km long transect cut at a low-angle oblique (SSE-NNW) to the interpreted flow direction of the MTD. The contact along the SW face is erosional, with a significant presence of blocks located just above the BSZ. The matrix there consists of sandy-mudstone with dispersed clasts but transitions to a muddy-sandstone in areas with high block deformation and abundance. Oblique variation across the southern face occurs in block size,

abundance, placement, and deformation. To facilitate comparison, a table with rough estimates of these characteristics across corresponding localities in (Figure 52A, 53A-C, 54A) was created. Table 1 indicates that block abundance and deformation vary along the low-angle oblique transect of the mass transport deposit. Both block concentration and deformation are highest at the northwestern end of the transect in Locality A1, then decrease notably at Locality A2. Beyond A2, both observed block deformation and abundance increase again through Localities A3 to A5, with elevated values sustained toward the southeastern extent of the transect.

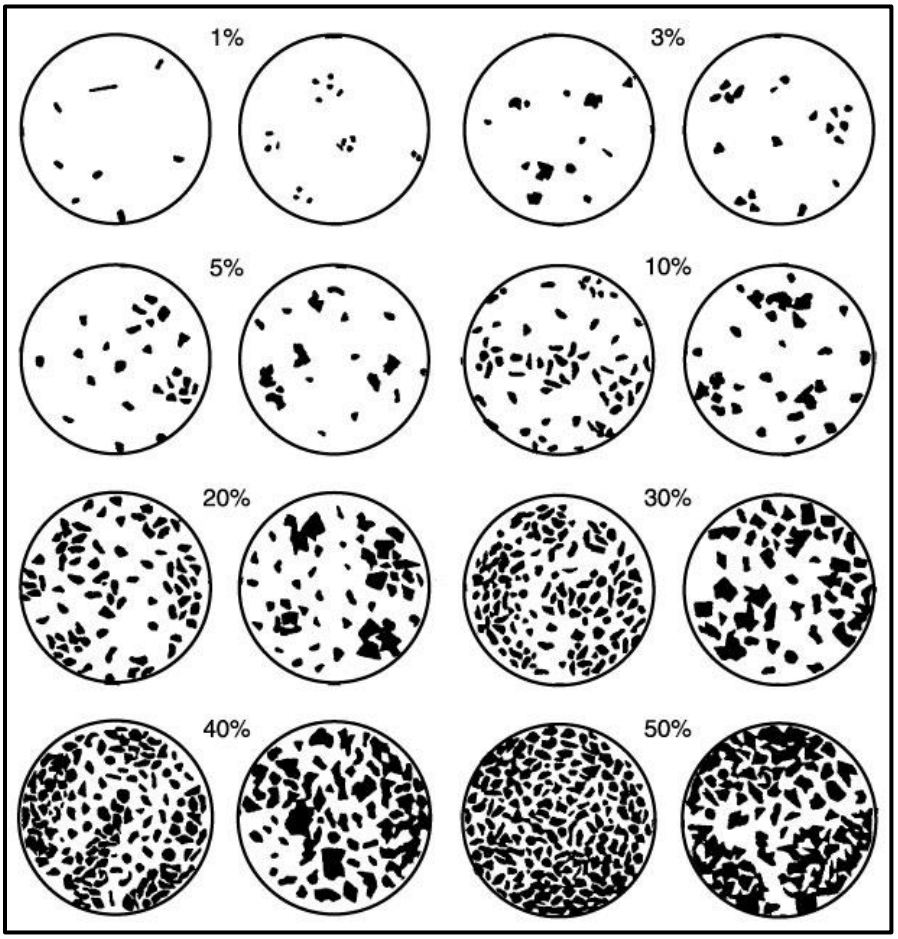

Figure 49: Grain comparison chart used to perceive visual percentages associated with block/matrix ratio within each locality of the outcrop. Block abundance and matrix volume were both derived from this table. Figure taken from (Terry and Chilingar, 1955).

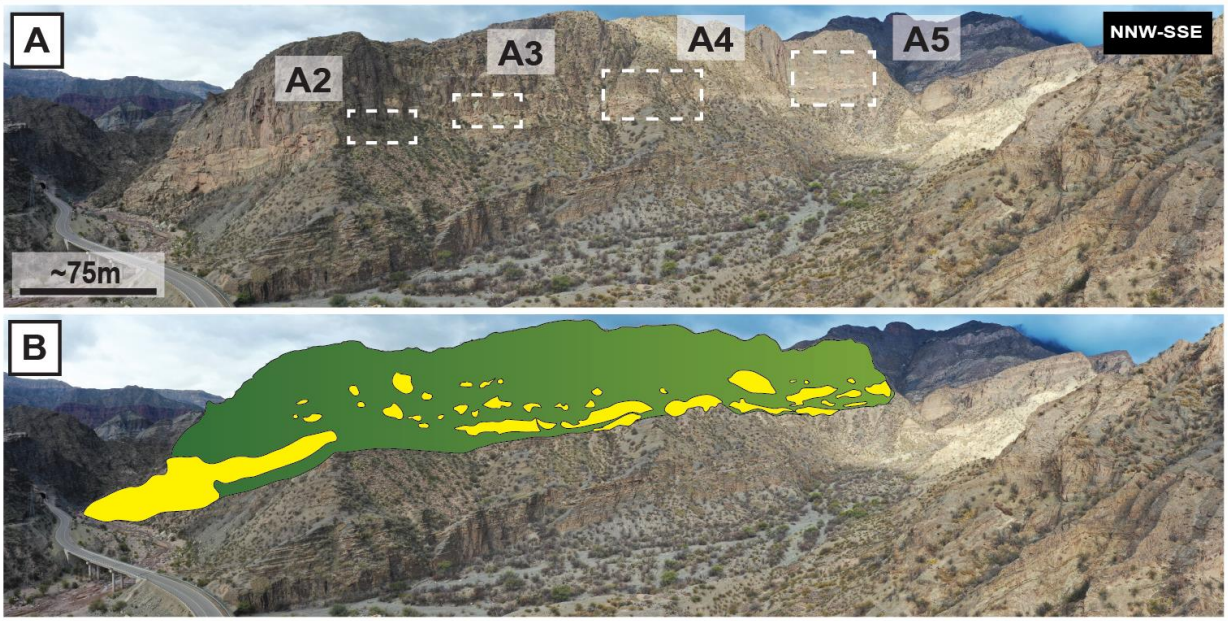

Figure 50: (a-b) Image of oblique transect used to show location for each locality and understand changing block abundance within the studied MTD. Note how there are fluctuating concentrations and heights above the BSZ of blocks across the deposit.

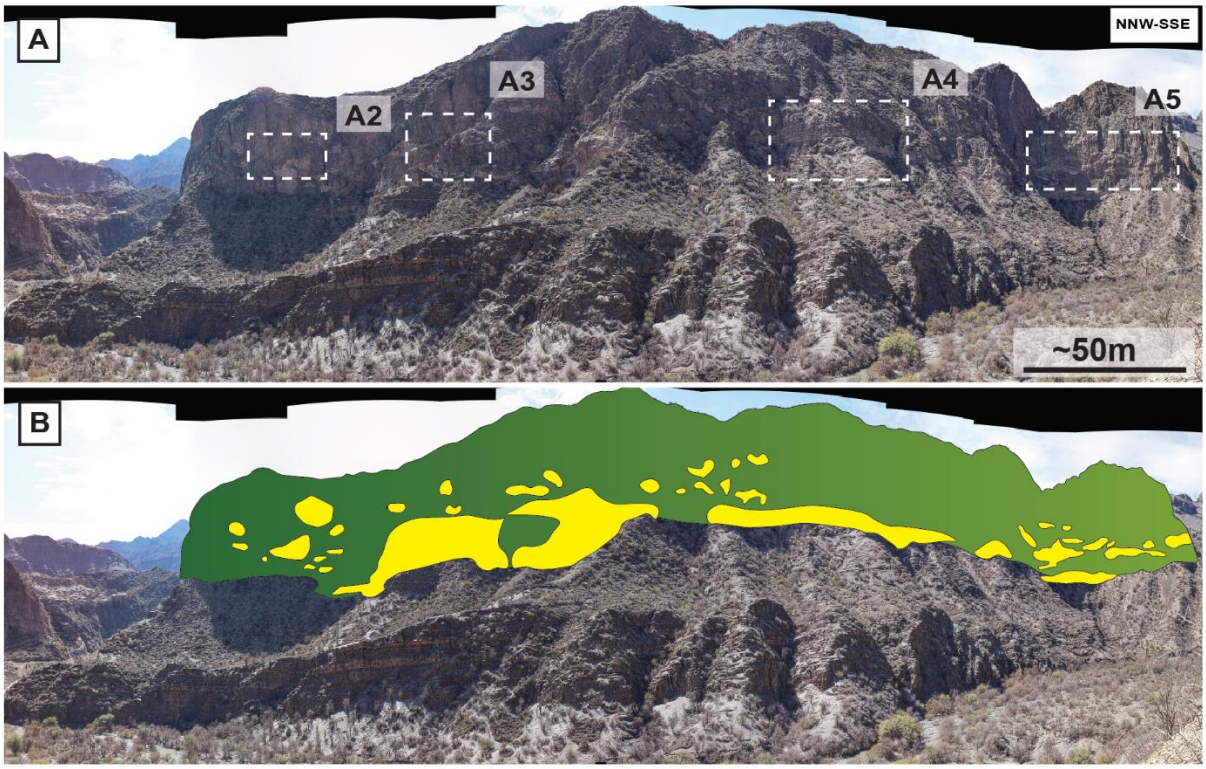

Figure 51: (a-b) Second imagery set of imagery displaying oblique transect used to show location for each locality and understand changing block abundance within the studied MTD.

Table 1: *Table shows rough estimates for changing characteristics at each locality across the face of the studied exposure. Table created from analyzing characteristics in (Figure 50A, 51B)*

Locality/ Figure	Avg. Block Size (m)	Block Deformation	Block Abundance %
A1/52A	W ~15 H ~ 4	High	~ 15-25%
A2/53A	W ~5 H ~ 2	Low	~ 5-15%
A3/53B	W ~ 6 H ~ 3	Moderate	~ 10-20%
A4/53C	W ~ 3 H ~ 3	Low - High	~ 10-20%
A5/45A	W ~ 10 H ~ 3	High	~ 10-15%

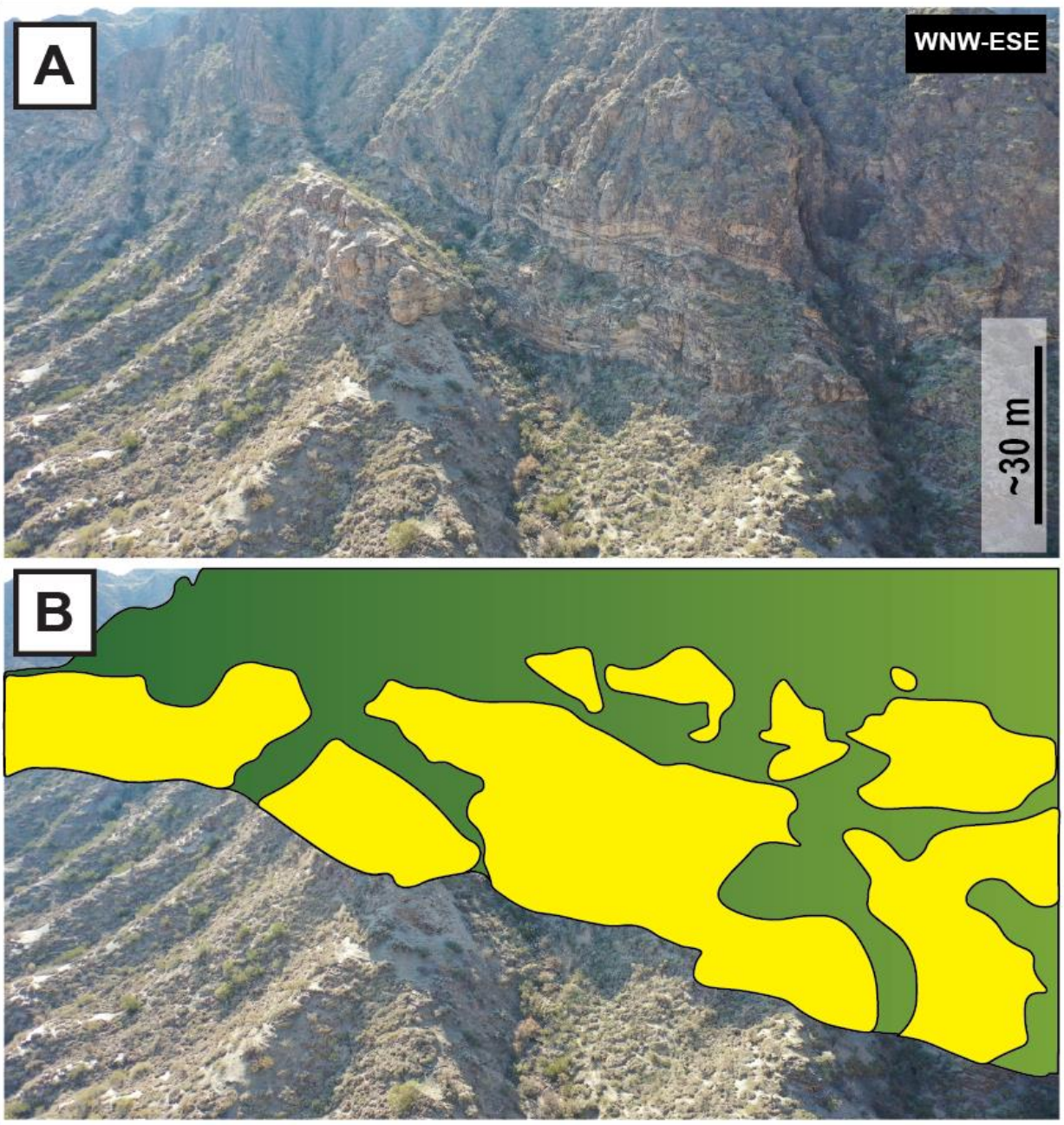

Figure 52: Locality A1 (location also shown in Figure 1). (A) The deposit exhibits a higher concentration of blocks, many of which appear stretched, with matrix infiltration producing a banded appearance within individual blocks. (B) Blocky units appear laterally extensive and interconnected, spanning significant distances across the outcrop.

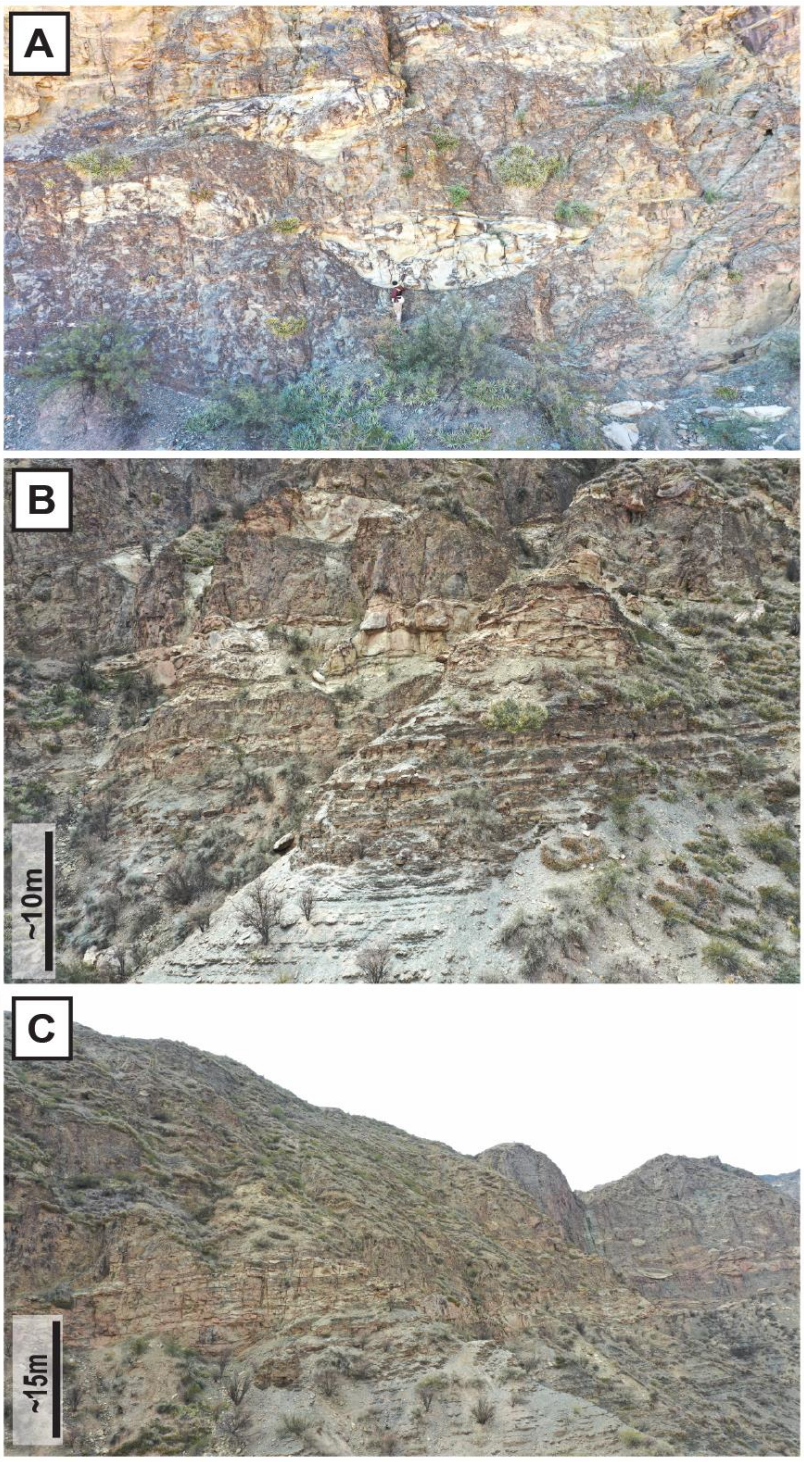

Figure 53: Locality A2-A4. (A) Locality A2, blocks occur at low concentrations and exhibit light amounts of deformation within the deposit. (B) Locality A3, block concentration increases, with many blocks displaying extensional deformation and limited intrusion of the surrounding matrix. (C) Locality A4, block density is highest, particularly along the lower portion of the MTD; however, deformation appears comparatively subdued in this interval.

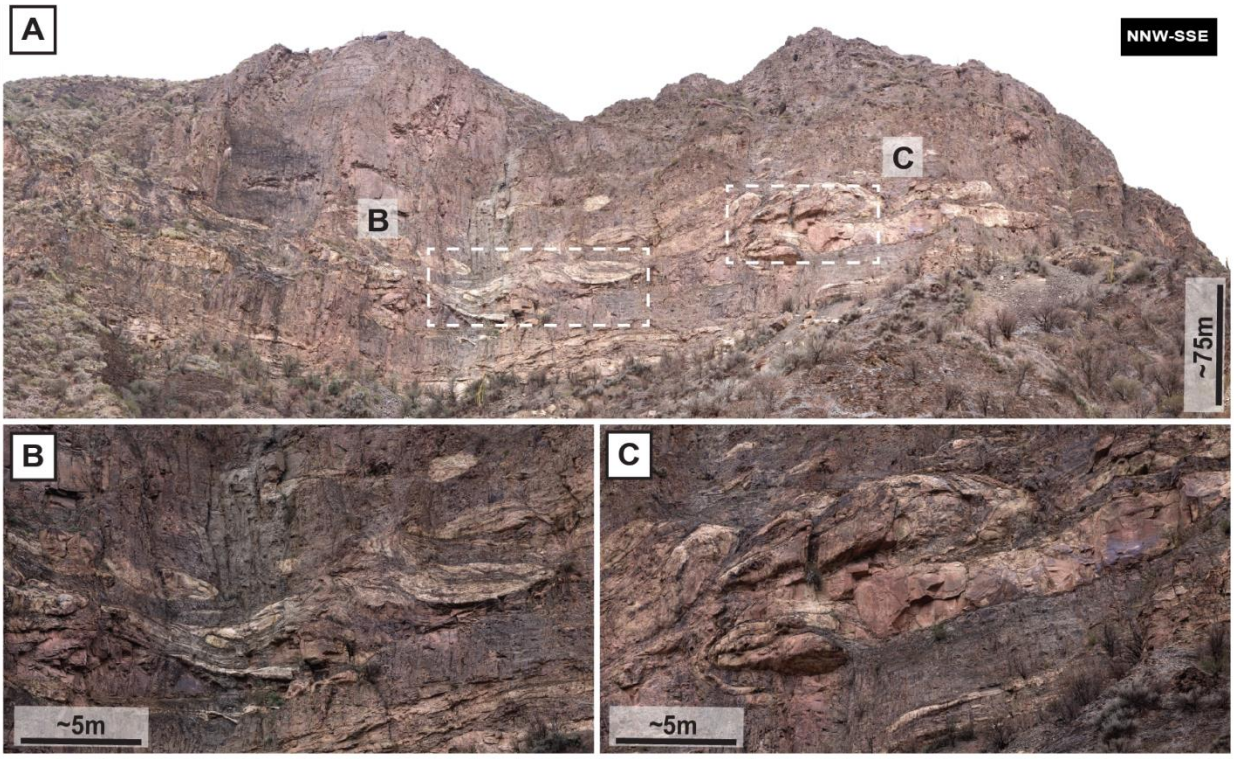

Figure 54: Locality A5. a) Vertical exposure of lightly to highly deformed blocks, moderately abundant and stacked at varying heights within the mass transport deposit MTD. (b) Zone of intense shearing and folding, illustrating a sharp transition between areas of strong and weak deformation. (c) Blocks are extensively sheared, folded, and disaggregated, with original structures barely preserved. Fluidization fabrics are evident as heterogeneous, banded zones of reworked block material.

INTERPRETATION: Over a broader scale, changes in block abundance and deformation are suggested to be potentially driven by a combination of four mechanisms within this study: (1) lobe deflection, which results in the shifting and stacking of different flow lobes, (2) energy dissipation through flow distribution, (3) proximity to the headwall/transport distance, (4) inclusion of eroded substrate.

Previous studies in other MTD's have documented the formation of depositional mass transport lobes across basin floors (e.g., Bull et al., 2009; Cardona et al., 2020; Jamil et al., 2021). Similar to compensational stacking observed at smaller scales, mass transport lobes are thought to migrate adjacent to previously emplaced lobes, which create topographic highs during

the same or earlier events. This process parallels lobe progradation in fluvial and deltaic settings, where river avulsion leads to the abandonment of older delta lobes and the development of new, active lobes due to localized over-sedimentation (Coe et al., 2005; Jerolmack & Swenson, 2007; Ganti et al., 2016; Gao, 2019; Catuneanu, 2022). Likewise, sedimentation within mass transport deposits can generate localized high relief, deflecting subsequent flows around existing lobes. Such shifts in lobe emplacement may induce lateral variability within the mass transport system and the variability in the abundance of blocks both laterally and vertically. A similar phenomenon was observed by Blair (1987), where dam failure triggered subaerial debris flows and unconfined fluvial discharge that produced successive shifting lobes with distinct compositional, structural, and sedimentary characteristics during a single depositional event.

Laboratory studies on the transition from confined to unconfined turbidity currents provide valuable insights into how flow expansion influences the development of distal turbidite structures. Lüthi (1981) found that as turbidity currents expanded freely, they exhibited progressive decreases in velocity and grain size, along with a distinct sequence of sedimentary structures that changed with increasing distance from the nodal point at which they became unconfined. This sequencing was linked to a reduction in flow energy, similar to the sedimentary divisions described by Bouma (1962). Additionally, as turbidity currents disperse, energy diminishes more rapidly along the distal regions of the flow, while remaining relatively elevated in the central portion of the unconfined system. This pattern indicates that the velocity characteristics of turbidity currents during lateral and distal transitions resemble those of mass transport processes. As a mass transport flows into an unconfined setting, velocity decreases both laterally and distally, potentially generating variations in block abundance and the degree of deformation.

Mass-flow disaggregation is commonly attributed to sediment mixing during downslope transport—a process closely linked to flow transformation and widely explored in previous studies (Morgenstern, 1967; Fisher, 1983; Haughton et al., 2003; Mutti et al., 2006; Strachan, 2008; Talling et al., 2012). The general idea is that increased transport distance allows more time for internal deformation and sediment reworking, resulting in progressive disaggregation and homogenization. This creates a continuum of deformation, ranging from relatively coherent blocks to highly disaggregated material through flow transformation. (Dasgupta, 2003; Strachan, 2008; Ogata et al., 2012; Rodrigues et al., 2021). Additionally, turbulent density flows typically exhibit preferential settling, where coarser grains settle out first as flow energy declines (Bouma, 1962; Mulder & Alexander, 2001; Talling et al., 2012; Pickering & Hiscott, 2016). Although MTDs occur under laminar flows, a similar process likely applies—denser and more massive blocks tend to settle earlier as the flow decelerates. The distribution of these blocks is therefore often linked to their distance from the initial failure zone. Proximal regions near the headwall escarpment commonly preserve larger, less-deformed blocks that settled early in the transport history, while more distal areas are typically characterized by increased disaggregation and smaller, more homogenized clasts (Bull et al., 2009; Rodrigues et al., 2021). This trend is supported by 3D seismic imagery presented (Figure 45), which shows larger, coherent blocks concentrated closer to the escarpment, transitioning basinward into smaller blocks and more disrupted, matrix-supported material. Proximity to the headwall may be a factor in the differences of block abundance and deformation observed within the oblique transect (Alves, 2015).

Erosion of the underlying substrate during mass transport can significantly influence the matrix content within the flow (e.g. Bull et al., 2009; Ogata et al., 2012; Sobiesiak et al., 2018;

Cardona et al., 2020; Rodrigues et al., 2021). As the moving mass scours and entrains material from the substrate, flow incorporates additional fine-grained sediments, increasing the overall matrix proportion. This entrainment alters flow properties and also could affect the capacity to transport and preserve intact blocks. Areas with more intense substrate erosion are therefore often characterized by a higher matrix-to-block ratio, reflecting the interaction between the flow and its basal surface. Additionally, Rodríguez-López et al. (2007) interpret that lateral facies variations beneath seismites can influence both the composition and style of overlying soft-sediment deformation. This relationship may be analogous to how erosionally incorporated substrates beneath MTD's can influence variations in composition and deformation across the deposit.

6). Local Contribution to Flow Direction

Milana et al. (2010) and Busco et al. (2019) propose a complex paleoslope with a NNE/NNW transport direction, based on kinematic indicators from MTD flows at Cerro Bola. This locality, approximately 40 kilometers to the northwest, contains mass transport deposits and turbidite sequences similar to those at Agua de la Peña Creek. Additionally, a localized flow direction to the NE has been described through fold facing patterns, opposite axial plane dip directions, and an LNS dominated flow model within study location (see Sobiesiak et al., 2017).

Structural measurements within the studied mass transport deposit were collected to better constrain localized flow directions and infer the associated paleoslope orientation. Fold hinges collected (n = 6) indicate a mean vector of 084.7° ± 55.4°. Once axial-plane directional data are rotated perpendicularly to give a northly facing direction 354.7°, measurements indicate the transport of the MTD towards the NNW. Thrusts were measured by matrix and blocks

ramped over preexisting material within the MTD in two sections. The down-dip direction of these thrusts provide values that are opposite to the direction to sediment transport (e.g. Strachan & Alsop, 2006; Isbell et al., 2010). Thrust down-dip directions were measured at (n = 20) and a difference of 90° occurs across the two measurement locations. A western thrust set measures a flow direction of 008.3° ± 32.2°, indicating a northerly flow direction (Figure 55B, 56A, C). 200 meters away, the eastern down-drip directions suggest a westerly flow direction of 288.9° ± 33.4° (Figure 55B, 56A-B). It's proposed that difference in flow direction within thrusts could arise from post-depositional adjustment (creep or faulting), changes in localized topography, lateral changes in lobe flow direction, or thrusts generated through major block deflection. Therefore, the structural measurements from the western locality suggest a paleoflow direction to the NNW-NNE.

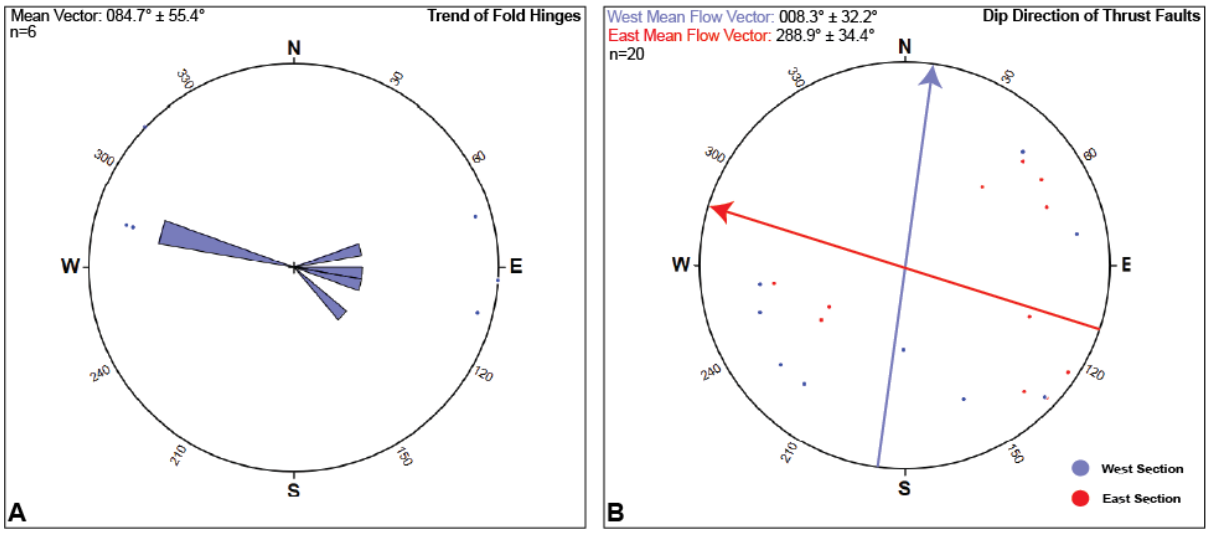

Figure 55: (A) Shows the direction of fold hinges collected. Field observations in addition to facing directions perpendicular to hinge measurements suggest a paleo-flow to the north. (B) Indicates the mean direction of measured thrusting. Thrusting was divided into West & East geographic locations to observe how flow direction changes laterally.

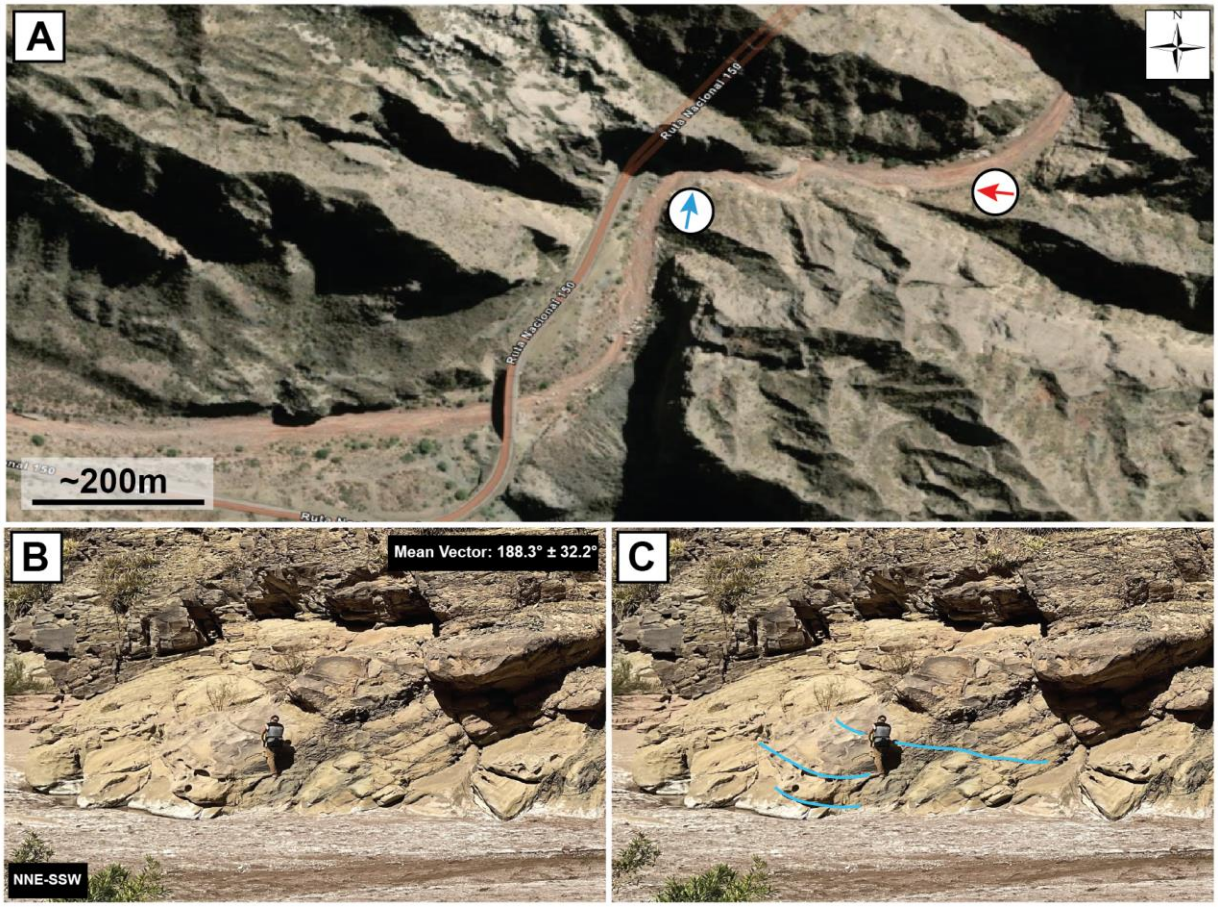

Figure 56: (A) Depicts the location of flow directions with the mean vector for each thrust set shown with an arrow. (B-C) Western section of thrusts with a southernly downdip direction.

7). Absence of Glacial Signature within Studied Mass Transport

Indications of glacially transported or altered material may be recognized through the presence of striated, polished, or faceted clasts and are sometimes incorporated within mass transport deposits (Krüger, 1984; Benn and Evans, 2010; Vesely et al., 2018; Isbell et al., 2021). Dropstone structures are often indicative of ice-rafted sediments deposited from melting ice in glacially influenced settings (e.g., Schermerhorn, 1974; Powell, 1984; Benn & Evans, 2010; Cowan et al., 2012; Fedorchuk et al., 2019). Dropstones, ranging in size from sand to boulders, typically deform underlying sediment upon deposition through mechanisms such as bending,

penetration, and upward rucking (Thomas and Connell, 1985; Bennett et al., 1996; Moxness et al., 2018; Isbell et al., 2024). At Agua de la Peña Creek, studies (e.g., Valdez Buso et al., 2019; Colombi et al., 2018, 2025; Spalletti et al., 2023) have documented glacially influenced material, particularly dropstones, within ponded turbidite intervals between MTD events lower in the Guandacol/Tuminico formation. Some of these studies (c.f. Valdez Buso et al., 2019; Spalletti et al., 2023) also report the presence of dropstone-like features within different MTD intervals. However, in the section examined in this study, the exotic clasts observed within the MTD succession do not exhibit preserved glacial signature, such as striated surfaces or dropstone penetration structures. Instead, the structures associated with these outsized clasts appear to result from flow kinematics and shearing, forming quarter structures (Figure 11A-B). Valdez Buso et al. (2019) suggested that some outsized clasts within the MTDs may represent resedimented dropstones derived from an original glacially influenced protolith. While this remains a possibility, the absence of glacially derived striated fabrics within these clasts renders the glacial origin of the protolith ambiguous. Therefore, no direct evidence for glacial or ice-rafted influence in the section studied here.

8). Discussion

8.1. Depositional Environment

Identifying lithofacies and interpreting their depositional environments are essential for constructing representations of paleoenvironmental and paleoclimatic conditions. Beneath the studied MTD, sequences of turbidite deposition characterized by interbedded shale and sandstone reflect deposition within a deep-water setting (Hampton, 1972; Mulder & Alexander, 2001; Posamentier & Walker, 2006; Pickering, 2016). The observed vertical and lateral

variations in turbidite thickness suggest dynamic depositional controls, potentially driven by lobe switching, basin subsidence, and/or base-level fluctuation. However, no shallow water indicators were observed within this study. The localized paleoflow/paleoslope direction is oriented toward the NNW–NNE through structural measurements. This inferred flow direction is broadly consistent with regional structural and sedimentological trends reported in previous studies (Milana et al., 2010; Sobiesiak et al., 2017; Buso et al., 2019). Additionally, Colombi et al. (2018; 2025) and Spalletti et al. (2019) briefly describe deltaic features within the studied mass-transport deposit in the region. This interpretation is consistent with crossbedding and laterally pinching sand bodies observed in this study (Figure 39), suggest that the studied MTD may have sourced from a deltaic environment.

8.2. MTD BSZ

Above the turbidite succession, at the base of the MTD deformation primarily occurs through erosion creating a thin layer of brecciated and sheared shale at the BSZ (Figure 57; Section 1-4). Near Section 1, deformation is observed in a discontinuous no-slip fashion (see Figure 17B; Sobiesiak et al., 2018). The substrate remains relatively undeformed at the contact but deforms downward with penetrating stress into softer substrate. Continuing across the basal surface, sporadic sandy-conglomeratic units within the BSZ are interpreted as evidence for early-stage high-density turbidity flows. Previous studies suggest (e.g. Fallgatter et al., 2017; Buso et al., 2019) the presence of conglomerate/gravel that may have acted as a blanketing layer of lubrication, facilitating mass movement and enhancing downslope mobility through elevated pore water pressure and reduced friction as the overlying flow interacted with deposits on the seafloor. Additionally, in the direction of flow, fluidization structures in Section 4 suggests a shift from dominantly erosional deformation to liquefaction-driven processes (Lowe, 2006; Ogata et

al., 2014; Sobesiak et al., 2018, Oyanyan et al., 2020; Jamil et al., 2021). The conversion to a more fluidized environment potentially reflects a combination of four main factors: (1) an increased presence of sandy conglomerate/gravel; (2) block separation and fragmentation; (3) fluid escape triggered by block loading; and (4) post-seismic activity affecting the region.

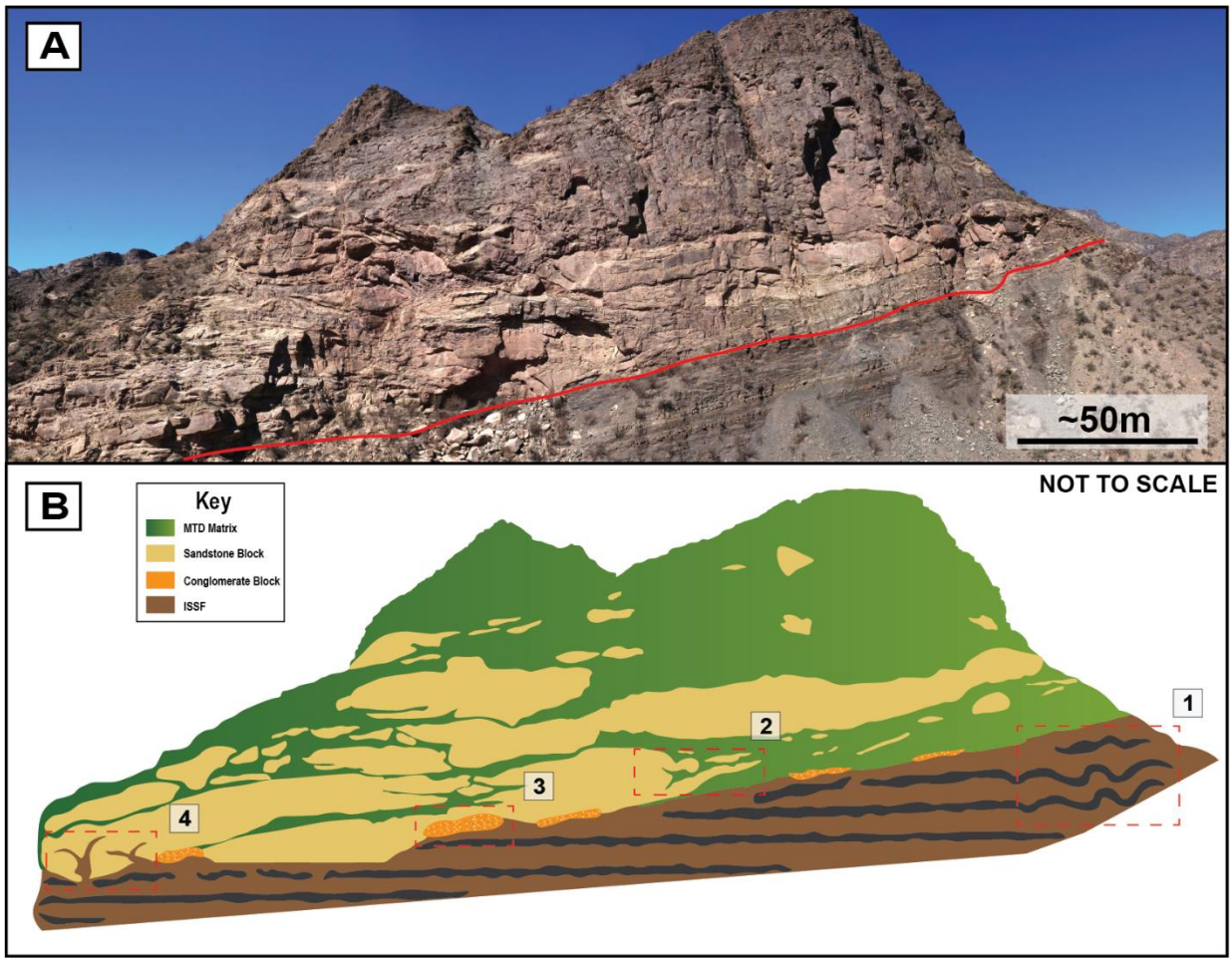

Figure 57: A) Overview of the outcrop with drawn in contact between MTD and substrate. (B) Cartoon version of the BSZ and its transformation across the outcrop. [1] Discontinuous no-slip deformation with penetrating strain. [2] Matrix infiltration into block in contact with the BSZ. [3] Conglomeratic units sporadically placed across the contact of the BSZ. [4] Fluidization structures observed above may have originated within the BSZ, seen as injections that crosscut blocks suspended within the flow.

8.3. Megabed Vertical Profile

Internal structure within the vertical profile of the mass transport deposit reveals distinct transitions in deformation style. Boundaries between intact blocks and the surrounding matrix

exhibit a vertical increase in deformation intensity but change sharply rather than gradationally, contrasting with patterns observed in other studies (Ogata et al., 2012; Sobiesiak et al., 2016; Fallgatter et al., 2017; Cardona et al., 2020; Rodrigues et al., 2020). Kinematically, the studied flow is interpreted to record a surging-like behavior freezing from the bottom upward regarding depositional timing. Material lower within the flow decelerated first, evidenced by matrix deflection and wrapping structures, as well as thrust development around block margins. The northern blocks of D2a (Sections 3–4) were likely deposited early, reflecting their greater size and density relative to later materials. Following D2a emplacement, subsequent surges involving the D1 matrix and smaller D2b blocks overtopped and flowed around the grounded D2a blocks, producing extensive thrusting, shearing, and fracturing within the previously deposited material. After the continued surging and emplacement of D1 and D2b, the final depositional phase of D2a occurred across Sections 1–2. Deposition was then capped by the emplacement of D3, representing the overflow of finer-grained material over the previously emplaced divisions (Figure 58).

The presence of large blocks contained within the vertical profile may be a result of three main factors. (1) The proximity to the headwall scarp results in large blocks that do not progress to the dynamic level of the main slide due to the lack of compressional forces in the extensional morphodomain (Alves et al., 2015). (2-3) Interaction with the BSZ and seafloor topography can induce block fragmentation through localized stress and differential velocity gradients (Ogata et al., 2012; Rodrigues et al., 2020). Furthermore, large block degeneration is observed in areas where the infiltration of matrix material disrupts block cohesion, leading to fragmentation at varying scales. This process may be enhanced by collision with grounded blocks or direct flow-

block interactions which can result in disaggregation, particularly when blocks are internally fluidized or there are variations in velocity throughout the flow.

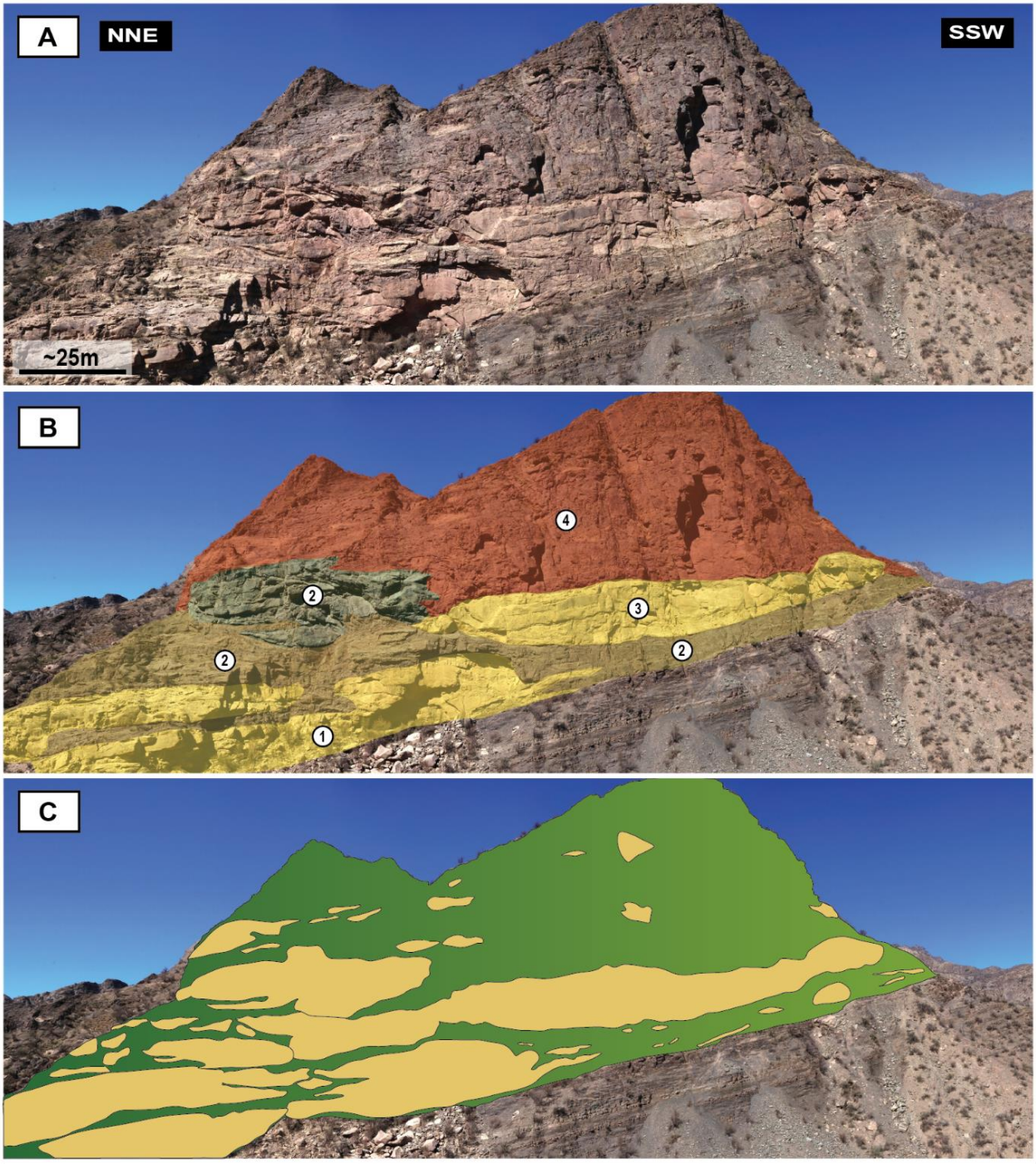

Figure 58: (A) Overview of outcrop for vertical profile. (B) Vertical profile showing the extent of described divisions and relative timing of their deposition. Refer to Figure 30 for divisional key. (C) Major sandstone block concentration within the vertical profile of the studied outcrop.

8.4. MTD Broad Variability Interpretation

Lateral variations in deformation style and block abundance along the low-angle oblique transect further reflect dynamic changes in flow behavior during transport. As shown in Table 1 & Figures 50-51, deformation and block concentration increase progressively from the southeastern end of the transect (Locality A5) through Localities A4 and A3, decline sharply at Locality A2, and reach their highest levels at the northwestern extent at Locality A1. These patterns could be a result of a combination of lobe stacking, confined to unconfined energy dissipation, proximity to the headwall, and substrate erosional key controls on the observed lateral variability. Lobe deflection could cause localized stacking of successive flow units, concentrating deformation and block emplacement in certain areas while bypassing others, similar to patterns described in basin-floor lobe systems (Bull et al., 2009; Cardona et al., 2020; Jamil et al., 2021). Energy dissipation associated with unconfined flow expansion likely contributed to local decreases in flow competence. Proximity to the initial failure escarpment could have influenced block size and preservation; larger, less-deformed blocks were preferentially deposited near the headwall, whereas more distal areas experienced increased internal shearing and block disaggregation with transport, consistent with trends reported by Alves et al. (2015) and Rodrigues et al. (2021). Finally, substrate erosion may influence both the matrix concentration and the degree of deformation within the deposit (Bull et al., 2009; Fallgatter et al., 2017; Sobiesiak et al., 2018). The potential combination of these processes generated a complex lateral pattern of block abundance and deformation preserved across the studied transect.

8.5. Glacial Influence

Indicators of glacial proximal-distal transport in the form of dropstone structures, have been documented in turbidite intervals at Agua de la Peña Creek (Valdez Buso et al., 2019; Colombi et al., 2018, 2025; Spalletti et al., 2023). Although some studies report dropstone-like features within MTDs, the exotic clasts observed in this studied MTD do not show preserved dropstones. Instead, their associated fabrics, including quarter and rotational structures (Figure 11A-B), are interpreted as products of flow kinematics and shearing. While it is possible these clasts originated from a glacially influenced protolith (Valdez Buso et al., 2019), no direct evidence of glacial or ice-rafted influence is preserved within the studied section.

9). Conclusion/Summary

This study was conducted in Agua De La Peña, San Juan, Argentina, using stratigraphic logging, structural measurements, and drone imagery analysis to investigate the morphology, deformation, and kinematics within a Late Paleozoic MTD. The main findings are:

- Multiple turbidite successions underlay the studied mass transport deposit. The vertical and lateral variations in turbidite cycle thickness could reflect a combination of depositional controls**,** including lobe switching, sea-level, and basin subsidence/uplift, which collectively influenced sediment distribution patterns over time.
- Structural and kinematic indicators, including folding and thrusting, suggest a localized flow direction toward the NNW-NNE. This aligns with regional and local studies by Milana et al. (2010), Sobiesiak et al. (2017), and Buso et al. (2019), further refining the interpretation of the paleoslope and paleoflow associated with the MTD.

- The BSZ across the outcrop is predominantly erosional; however, the increasing presence of fluidization structures in Section 4 suggests a progressive shift from frictional, erosive shearing to liquefaction-driven deformation, likely controlled by factors such as block separation, substrate fluid escape, and/or seismic activity. The change in features laterally along the BSZ suggest that a mosaic of conditions occur along the base of MTDs depending on substrate conditions, flow kinematics, topography on the sea floor and possibly due to other causes.
- The sporadic sandy conglomerate/gravel deposits at the BSZ may indicate an early-stage high-density turbidite or grain flow, potentially acting as a lubricant for mass movement, reinforcing the role of fluid overpressure in enhancing mobility and reducing friction within the basal shear zone.
- The abrupt transitions between deformed blocks and homogenized matrix within the studied MTD contrasts with the gradual deformation observed in other studies and suggests a surging flow across the deposit.
- The preservation of large, coherent blocks in the lower flow domains may result from a combination of factors such as short transport distance, shear stress proximity to the BSZ, and limited exposure to compressional or extensional stress
- Fragmentation of blocks within the deposit is influenced by interactions with the BSZ and divisional flow collision, where mechanisms like differential velocity gradients, stress from the BSZ, and flow-block interaction contribute to disaggregation and the disruption of coherent block structures.
- Broad lateral variability in the MTD is primarily driven by four key processes: lobe deflection, which results in shifting and stacking of flow lobes, unconfined flow energy

dissipation, where velocity reduction influences deformational structures and sediment distribution, distance from the head wall scarp, and substrate erosion.

- This study finds no direct evidence of glacial activity within the studied mass transport deposit but rather outsized clasts exhibit quarter structures as a result of flow shearing.

References:

Allmendinger, R. W., Cardozo, N., & Fisher, D. M. (2011). Structural geology algorithms: Vectors and tensors. Cambridge University Press. http://www.geo.cornell.edu/geology/faculty/RWA/programs/stereonet.html

Allen, J.R.L., (1982). Sedimentary Structures: Their Character and Physical Basis.

Alonso-Muruaga, P. J., Limarino, C. O., Spalletti, L. A., & Colombo Piñol, F. (2018). Depositional settings and evolution of a fjord system during the carboniferous glaciation in northwest Argentina. *Sedimentary Geology*, *369*, 28–45. https://doi.org/10.1016/j.sedgeo.2018.03.002

Alsop, G.I., Holdsworth, R.E., (1993). The distribution, geometry and kinematic significance of Caledonian buckle folds in the western Moine Nappe, northwestern Scotland. Geol. Mag. 130, 353. http://dx.doi.org/10.1017/S0016756800020033.

Alsop, G.I., Holdsworth, R.E., 2004. Shear zone folds: records of flow perturbation or structural inheritance. In: Alsop, G.I., Holdsworth, R.E., MccaffreY, K.J.W., Hand, M.

Alsop, G.I., Holdsworth, R.E., (2007). Flow perturbation folding in shear zones. Geol. Soc. Lond. 272, 75e101. http://dx.doi.org/10.1144/GSL.SP.2007.272.01.06. Spec Publ.

Alsop, G. I., & Marco, S. (2012). A large-scale radial pattern of seismogenic slumping towards the Dead Sea Basin. *Journal of the Geological Society*, *169*(1), 99–110. https://doi.org/10.1144/0016-76492011-032

Alsop, G. I., Weinberger, R., Marco, S., & Levi, T. (2019). Folding during soft-sediment deformation. *Geological Society, London, Special Publications*, *487*(1), 81–104. https://doi.org/10.1144/sp487.1

Alsop, G. I., Marco, S., Weinberger, R., & Levi, T. (2024). Slide stacking: A new mechanism to repeat stratigraphic sequences during gravity-driven extension. *Journal of Structural Geology*, *185*, 105184. https://doi.org/10.1016/j.jsg.2024.105184

Alves, T. M., & Cartwright, J. A. (2010). The effect of mass transport deposits on the younger slope morphology, offshore Brazil. https://eurekamag.com/research/037/178/037178806.php

Alves, T. M., & Lourenço, S. D. N. (2010). Geomorphologic features related to gravitational collapse: Submarine landsliding to lateral spreading on a late miocene–quaternary slope

(Se Crete, Eastern Mediterranean). *Geomorphology*, *123*(1–2), 13–33. https://doi.org/10.1016/j.geomorph.2010.04.030

Alves, T. M. (2010). 3D seismic examples of differential compaction in mass-transport deposits and their effect on post-failure strata. *Marine Geology, 271*, 212–224.

Alves, T.M., (2012). Scale-relationships and geometry of normal faults reactivated during gravitational gliding of Albian rafts (Espírito Santo Basin, SE Brazil). Earth Planet. Sci. Lett. 331e2, 80e96. http://dx.doi.org/10.1016/j.epsl.2012.03.014.

Alves, T. M. (2015). Submarine slide blocks and associated soft sediment deformation in deep-water basins: A review. Marine and Petroleum Geology, 67, 262–285. https://doi.org/10.1016/j. marpetgeo.2015.05.010

Armitage, D. A., B. W. Romans, J. A. Covault, and S. A. Graham. (2009). The influence of mass-transport deposit surface topography on the evolution of turbidite architecture: The Sierra Contreras, Tres Pasos Formation (Cretaceous), Southern Chile: Journal of Sedimentary Research, v. 79, no. 5, p. 287–301, doi:10.2110/jsr .2009.035.

Andreis, R. R., Leguizamón, R., & Archangelsky, S. (1986). El paleovalle de Malanzán: nuevos criterios para la estratigrafía del Neopaleozoico de la Sierra de Los Llanos, La Rioja, República Argentina. *Boletín de la Academia Nacional de Ciencias*, *57*(1-2), 3-119.

Aquino, C. D., Milana, J. P., & Faccini, U. F. (2014). New glacial evidences at the Talacasto Paleofjord (Paganzo Basin, W-argentina) and its implications for the paleogeography of the gondwana margin. *Journal of South American Earth Sciences*, *56*, 278–300. https://doi.org/10.1016/j.jsames.2014.09.001

Anell, I. (2024). The quintessential S-shape in sedimentology: A review on the formation and controls of Clinoform Shape. *Earth-Science Reviews*, *254*, 104821. https://doi.org/10.1016/j.earscirev.2024.104821

Arnott, R.W., C., (2010) Deep-marine sediments and sedimentary systems, in: James, N.P., dalrymple, R.W. (Eds.), Facies Models 4. Geological Association of Canada, St. John's , Newfoundland, pp. 295-322.

Astini, R. A., Benedetto, J. L., & Vaccari, N. E. (1995). The early Paleozoic evolution of the Argentine Precordillera as a Laurentian rifted, drifted, and collided terrane: A geodynamic model. Geological Society of America Bulletin, 107, 253–273.

Badalini, G., B. C. Kneller, and C. D. Winker. (2000). Architecture and processes in the Late Pleistocene BrazosTrinity turbidite system, Gulf of Mexico continental slope, in P.

Weimer, R. M. Slatt, J. Coleman, N. C. Rosen, H. Nelson, A. H. Bouma, M. J. Styzen, and D. T. Lawrence, eds., Deep-water reservoirs of the world: Gulf Coast Section SEPM 20th Annual Research Conference, Houston, Texas, December 3–6, 2000, CDROM, p. 16–33.

Bea, R.G., (1971). How sea floor slides affect offshore structures. Oil Gas J. 69, 88–92.

Bagnold, R.A. (1962). Auto-suspension of transported sediment: turbidity currents. Proc. Roy. Soc. London, A265, 315±319.

Benn, D., Evans, D. J. A., & Mould, A. (2010). *Glaciers and glaciation*. Arnold, London, U.K. 802 pp.

Bennett, M.R., Doyle, P., Mather, A.E., 1996. Dropstones; their origin and significance. Palaeogeogr. Palaeoclimatol. Palaeoecol. 121 (3–4), 331–339.

Bennett, M. R. (2001). The morphology, structural evolution and significance of Push Moraines. *Earth-Science Reviews*, *53*(3–4), 197–236. https://doi.org/10.1016/s0012-8252(00)00039-8

Blair, C.T. (1987). Sedimentary processes, vertical stratification sequences, and geomorphology of the Roaring River Alluvial fan, Rocky Mountain National Park, Colorado. *SEPM Journal of Sedimentary Research*, *Vol. 57*. https://doi.org/10.1306/212f8a8a-2b24-11d7-8648000102c1865d

Bouma, A.H. (1962). Sedimentology of Some Flysch Deposits: a Graphic Approach to Facies Interpretation. Elsevier, Amsterdam.

Bouma, A.H. (1987). Megaturbidite: An acceptable term? GeoMar. Lett., 7, 63–67.

Brandt, D., Ernesto, M., Rocha-Campos, A. C., & Dos Santos, P. R. (2009). Paleomagnetism of the Santa Fé Group, central Brazil: Implications for the late Paleozoic apparent polar wander path for South America. *Journal of Geophysical Research: Solid Earth*, *114*(B2), 2008JB005735. https://doi.org/10.1029/2008JB005735

Boggs Jr., S., 2006. Principles of Sedimentology and Stratigraphy. Fourth Edition. Pearson Prentice Hall, USA, Pp. 676.

Borgomano, J.R.F., (2000). The Upper Cretaceous carbonates of the Gargano-Murge region, southern Italy: a model of platform-to-basin transition. Am. Assoc. Pet. Geol. Bull. 84, 1561e1588.

Buatois, L. A., & Mangano, M. G. (1995). Post glacial lacustrine event sedimentation in an ancient mountain setting: Carboniferous Lake Malanzan (western Argentina). *Journal of Paleolimnology*, *14*(1), 1–22. https://doi.org/10.1007/bf00682591

Bull, S., Cartwright, J., & Huuse, M. (2009). A review of kinematic indicators from mass-transport complexes using 3D seismic data. *Marine and Petroleum Geology*, *26*(7), 1132–1151. https://doi.org/10.1016/j.marpetgeo.2008.09.011

Buso, V. V., Milana, J. P., Sobiesiak, M. S., & Kneller, B. (2019). The carboniferous MTD complex at La Peña Canyon, Paganzo Basin (San Juan, Argentina). *Geophysical Monograph Series*, 105–116. https://doi.org/10.1002/9781119500513.ch7

Butler, R.W.H., Eggenhuisen, J.T., Haughton, P., McCaffrey, W.D., (2016). Interpreting syndepositional sediment remobilization and deformation beneath submarine gravity flows; a kinematic boundary layer approach. J. Geol. Soc. (Lond.) 173, 46–58. https://doi.org/10.1144/jgs2014-150.

Cardona, S., Wood, L. J., Dugan, B., Jobe, Z., & Strachan, L. J. (2020). Characterization of the rapanui mass-transport deposit and the basal shear zone: Mount Messenger Formation, Taranaki Basin, New Zealand. *Sedimentology*, *67*(4), 2111–2148. https://doi.org/10.1111/sed.12697

Caradonna, M. C., Del Ben, A., Pini, G. A., Geletti, R., & Frisicchio, V. (2025). Recent mass transport deposits in the Gulf of Cagliari. *Marine Geology*, *483*, 107515. https://doi.org/10.1016/j.margeo.2025.107515

Catuneanu, O. (2022). Data in sequence stratigraphy. *Principles of Sequence Stratigraphy*, 23–92. https://doi.org/10.1016/b978-0-444-53353-1.00006-7

Chang, H.K., Kowsmann, R.O., Figueiredo, A.M.F., Bender, A.A., (1992). Tectonics and stratigraphy of the East Brazil Rift System: an overview. Tectonophysics 213, 97–138.

Coe, A. L., Bosence, D. W. J., Church, K. D., Flint, S. S., Howell, J. A., & Wilson, R. C. L. (2005). *The sedimentary record of sea-level change*. Open University ; Cambridge University Press.

Colgan, P. (1999). *Glacial Processes Past and Present* (D. M. Mickelson & J. W. Attig, Eds.). Geological Society of America.

Colombi, C. E., Limarino, C. O., & Césari, S. N. (2018). La Sucesión Carbonífera De La Quebrada Agua De La Peña (Sierra De Valle Fértil): Ambientes Sedimentarios, Contenido Fosilífero E Importancia Estratigráfica. *Latin American Journal of Sedimentology and Basin Analysis*, *25*(1), 19–53.

Colombi, C., Alonso Muruaga, P., Kusick, A., Isbell, J., Fedorchuk, N., Alarcon, C., & Limarino, C. (2025). *Glacial and Postglacial Sedimentation in a Late Paleozoic Tectonically Active Mountain Front, Agua De La Peña Area, West Argentina*, 1–48.

Cook, A. C., & Johnson, K. R. (1970). Early Joint Formation in sediments. *Geological Magazine*, *107*(4), 361–368. https://doi.org/10.1017/s0016756800056223

Cowan, E.A., Powell, R.D. (1990). In: Dowdeswell, J.A., Scourse, J.D. (Eds.), Suspended Sediment Transport and Deposition of Cyclically Interlaminated Sediment in a Temperate Glacial Fjord, Alaska, U.S.A. 53. Geological Society Special Publication, pp. 75–89.

Cowan, E.A., Christoffersen, P., Powell, R.D., (2012). Sedimentological signature of a deform-1129 able bed preserved beneath an ice stream in a late Pleistocene glacial sequence, Ross 1130 Sea, Antarctica. Journal of Sedimentary Research 82, 270–282.

Croot, D.G. (1988). Morphological, structural and mechanical analysis of neoglacial icepushed ridges in Iceland. In: Croot, D.G. (Ed.), Glaciotectonics: Forms and Processes. A. A. Balkema, Rotterdam, pp. 33–47.

Crowell, J.C., Frakes, L.A., (1970). Ancient Gondwana glaciations. In: S.H. Haughton (Ed.), Proceedings and Papers of the Second Gondwana Symposium, South Africa. CSIR, Pretoria, pp. 469-476.

Cuerda, A.J., Cingolani, C.A., Varela, R., Schauer, O.C., 1979. Depósitos carbónicos en la 700 vertiente occidental de la Sierra de Valle Fértil, provincia de San Juan. Revista de la Asociación 701 Geológica Argentina 34, 100–107.

Dakin, N., Pickering, K.T., Mohrig, D., Bayliss, N.J., (2013). Channel-like features created by erosive submarine debris flows: field evidence from the Middle Eocene Ainsa Basin, Spanish Pyrenees. Mar. Petrol. Geol. 41, 62–71. https://doi.org/10.1016/j. marpetgeo.2012.07.007.

Dasgupta, P. (2003). Sediment gravity flow-the conceptual problems. Earth Sci. Rev. 62, 265–281. https://doi.org/10.1016/S0012-8252(02)00160-5.

De Blasio, F.V., Elverhøi, A., (2011). Properties of mass-transport deposits as inferred from dynamic modeling of subaqueous mass wasting: a short review. Mass-transport Depos. Deep. Settings 499–508.

De Blasio, F.V.F.V., Elverhøi, A., Issler, D., Harbitz, C.B., Bryn, P., Lien, R., (2005). On the dynamics of subaqueous clay rich gravity mass flows—the giant Storegga slide, Norway. Mar. Petrol. Geol. 22, 179–186. https://doi.org/10.1016/j.marpetgeo.2004. 10.014.

De Blasio, F. V., Engvik, L. E., & Elverhøi, A. (2006). Sliding of outrunner blocks from submarine landslides. *Geophysical Research Letters*, *33*(6). https://doi.org/10.1029/2005gl025165

De Lima Rodrigues, M. C., Trzaskos, B., Alsop, G. I., & Vesely, F. F. (2020). Making a homogenite: An outcrop perspective into the evolution of deformation within mass-transport deposits. *Marine and Petroleum Geology*, *112*, 104033. https://doi.org/10.1016/j.marpetgeo.2019.104033

Desjardins, P. R., Buatois, L. A., Limarino, C. O., & Cisterna, G. A. (2009). Latest carboniferous–earliest Permian transgressive deposits in the Paganzo Basin of western argentina: Lithofacies and sequence stratigraphy of a coastal-plain to Bay Succession. *Journal of South American Earth Sciences*, *28*(1), 40–53. https://doi.org/10.1016/j.jsames.2008.10.003

Dietz, R.S., (1963). Wave-base, marine profile of equilibrium, and wave-built terraces: A critical appraisal: Geological Society of America Bulletin, v. 74, p. 971–990, doi:10.1130/0016 -7606(1963)74[971:WMPOEA]2.0.CO;2.

Dixon, J.F., Steel, R.J., Olariu, C., (2013). A model for cutting and healing of deltaic mouth bars at the shelf edge: mechanism for basin-margin accretion. J. Sediment. Res. 83 (3), 284–299.

Dott, R.H. (1963) Dynamics of subaqueous gravity depositional processes. AAPG Bull., 47, 104–128.

Dott, R.H., Jr., and Bourgeois, J., (1982). Hummocky stratification; significance of its variable bedding sequences: Geological Society of America Bulletin, v. 93, p. 663–680, doi:10.1130/0

Duke, W.L., Arnott, R.W.C., and Cheel, R.J., (1991). Shelf sandstones and hummocky cross stratification—New insights on a stormy debate: Geology, v. 19, p. 625–628, doi:10.1130/0091 -7613(1991)0192.3.CO;2.

Dowdeswell, J.A., Canals, M., Jakobsson, M., Todd, B.J., Dowdeswell, E.K., Hogan, K.A., (2016). Atlas of Submarine Glacial Landforms: Modern, Quaternary and Ancient. Geological Society of London.

Dykstra, M., Kneller, B., Milana, J.P. (2006). Deglacial and postglacial sedimentary Architecture in a deeply incised paleovalley-paleofjord; the late Carboniferous (Pennsylvanian) Jejenes Formation, San Juan, Argentina. Geological Society of America Bulletin 118, 913–937.

Dykstra, M., Garyfalou, K., Kertznus, V., Kneller, B., Milana, J. P., Molinaro, M., Szuman, M., & Thompson, P. (2011). Mass-transport deposits: Combining outcrop studies and seismic forward modeling to understand lithofacies distributions, deformation, and their seismic stratigraphic expression. *Mass-Transport Deposits in Deepwater Settings*, 293–310. https://doi.org/10.2110/sepmsp.096.293

Emmerich, A., Zamparellu, Bechsta€dt, T., Zühlke, R., 2005. The reefal margin and slope of a Middle Triassic carbonate platform: the Latermar (Dolomites, Italy). Facies 50, 573e614.

Evans, D. J. A. (2018). *Till: A glacial process sedimentology*. John Wiley & Sons Ltd.

Eyles, N., (1993). Earth's glacial record and its tectonic setting. Earth-Science Reviews 35, 1-248.

Fairweather, L. (2014). Mechanisms of supra-MTD topography generation and the interaction of turbidity currents with such deposits, (Unpublished PhD thesis). Aberdeen, Scotland: University of Aberdeen.

Fallgatter, C., Kneller, B., Paim, P.S.G., Milana, J.P. (2017). Transformation, partitioning and flow-deposit interactions during the run-out of megaflows. Sedimentology 64, 359. https://doi.org/10.1111/sed.12307.

Farrell, S.G. (1984). A dislocation model applied to slump structures, Ainsa Basin, South Central Pyrenees. J. Struct. Geol. 6, 727–736.

Fedorchuk, N. D., Isbell, J. L., Griffis, N. P., Vesely, F. F., Rosa, E. L. M., Montãnez, I. P., Mundil, R., Yin, Q.-Z., Iannuzzi, R., Roesler, G., & Pauls, K. N. (2019). Carboniferous glaciotectonized sediments in the southernmost Paraná Basin, Brazil: Ice marginal dynamics and Paleoclimate Indicators. *Sedimentary Geology*, *389*, 54–72. https://doi.org/10.1016/j.sedgeo.2019.05.006

Fernández Seveso, F., and Tankard, A.J. (1995). Tectonics and stratigraphy of the Late Paleozoic Paganzo Basin of Western Argentina and its Regional Implications, in Tankard, A.J., Suarez, S., and Welsink, H.J., eds., Petroleum Basins of South America, Volume 62: AAPG Memoir, AAPG, p. 285-301.

Fielding, C. R., Frank, T. D., and Isbell, J. L. (2008a). The late Paleozoic ice age--A review of current understanding and synthesis of global climate patterns, in Fielding, C. R., Frank, T. D., and Isbell, J. L., eds., Resolving the Late Paleozoic Ice Age in Time and Space:: Boulder, CO, Geological Society of America Special Publication., p. 343-354.

Fielding, C.R., Frank, T.D., Birgenheier, L.P., Rygel, M.C., Jones, A.T., Roberts, J., (2008b). Stratigraphic imprint of the late Palaeozoic ice age in eastern Australia: a record of alternating glacial and nonglacial climate regime. Journal of the Geological Society, London 165, 129-140.

Fielding, C.R., Frank, T.D., Isbell, J.L., (2008c). The late Paleozoic ice age—A review of current understanding and synthesis of global climate patterns. Geological Society of America Special Papers 441, 343-354.

Fielding, C.R., Frank, T.D., Birgenheier, L.P., (2022). A revised, late Palaeozoic glacial time-space framework for eastern Australia, and comparisons with other regions and events. Earth Science Reviews 104263.

Fisher, R., 1983. Flow transformations in sediment gravity flows. Geology 11, 273–274. https://doi.org/10.1130/0091-7613(1983)11.

Flores, G., 1959. Evidence of slump phenomena (olisthostromes) in areas of hydrocarbon exploration in Sicily. Proc. 5th World Petr. Congr. Sect. 1, New York, pp. 259–275.

Fossen, H., (2010). Structural Geology. Cambridge University Press, Cambridge, 480 pp.

Fossen, H., (2016). Structural Geology, second ed. Cambridge University Press, pp. 510p.

Fossen, H., & Cavalcante, G. C. G. (2017). Shear zones – A review. *Earth-Science Reviews, 171*, 434–455.

Frakes, L. A., Francis, J. E., and Syktus, J. I. (1992). Climate modes of the Phanerozoic, Cambridge, Cambridge University Press, 274 p.

Gao, W., Shao, D., Wang, Z. B., Nardin, W., Rajput, P., Yang, W., Sun, T., & Cui, B. (2019). Long-term cumulative effects of intra-annual variability of Unsteady River Discharge on the progradation of Delta lobes: A modeling perspective. *Journal of Geophysical Research: Earth Surface*, *124*(4), 960–973. https://doi.org/10.1029/2017jf004584

Ganti, V., Chu, Z., Lamb, M. P., Nittrouer, J. A., & Parker, G. (2014). Testing morphodynamic controls on the location and frequency of river avulsions on fans versus deltas: Huanghe (Yellow River), China. Geophysical Research Letters, 41, 7882–7890. https://doi.org/ 10.1002/2014GL061918

Gastaldo, R.A., DiMichele, W.A., Pfefferkorn, H.W. (1996). Out of the icehouse into the greenhouse: a late Paleozoic analogue for modern global vegetational change. GSA Today, v. 10, p. 1-7.

Gee, M.J.R., Gawthorpe, R.L., Friedmann, S.J., (2006). Triggering and evolution of a giant landslide, offshore Angola revealed by 3D seismic stratigraphy and geomorphology. Journal of Sedimentary Research 76, 9–19.

González, C. (1982). Pavimento glaciario en el Carbónico de la Precordillera. Revista de la Asociación Geológica Argentina 36, 262–266.

Goscombe, B. D., Passchier, C. W., & Hand, M. (2004). Boudinage classification: End-member Boudin types and modified Boudin structures. *Journal of Structural Geology*, *26*(4), 739–763. https://doi.org/10.1016/j.jsg.2003.08.015

Greene, H. G., L. Y. Murai, P. Watts, N. A. Maher, M. A. Fisher, C. E. Paull, and P. Eichhubl. (2006). Submarine landslides in the Santa Barbara Channel as potential tsunami sources: Natural Hazards and Earth System Sciences, v. 6, p. 63–88, doi:10.5194/nhess-6-63-2006.

Grobe, H., Diekmann, B., & Hillenbrand, C.-D. (2012). In *The memory of the polar oceans* (pp. 37–45). essay, British Antarctic Survey.

Gulbranson, E. L., Montañez, I. P., Schmitz, M. D., Limarino, C. O., Isbell, J.L., Marenssi, S. A., Crowley, J. L., (2010). High-precision U–Pb calibration of Carboniferous glaciation and climate history, Paganzo Group, NW Argentina. Geological Society of America Bulletin 122,1480–1498.

Hambrey, M.J., Glasser, N.F., (2012). Discriminating glacier thermal and dynamic regimes in the sedimentary record. Sedimentary Geology 251, 1-33. doi:10.1016/j.sedgeo.2012.01.008

Hampton, M.A. (1972). The role of subaqueous debris flow in generating turbidity currents. J. Sed. Petrol., 42, 775–793.

Hampton, M.A., Lee, H.J., Locat, J., (1996). Submarine landslides. Rev. Geophys. 34, 33–59. https://doi.org/10.1029/95RG03287.

Hansen, E. (1971). Strain Facies. Springer, Berlin.

Haughton, P.D.W., Barker, S.P., McCaffrey, W.D., 2003. 'Linked' debrites in sand-rich turbidite systems – origin and significance. Sedimentology 50, 459–482.

Henry, L.C., Isbell, J.L., Limarino, C.O., (2008). Carboniferous glacigenic deposits of the proto-Precordillera of west-central Argentina, In: Fielding, C.R., Frank, T.D., Isbell, J.L. (Eds.), Resolving the Late Paleozoic Ice Age in Time and Space:. Geological Society of America Special Publication., Boulder, CO, pp. 131-142.

Henry, L. C., Isbell, J. L., & Limarino, C. O. (2014). The late paleozoic el imperial formation, western Argentina: Glacial to post-glacial transition and stratigraphic correlations with arc-related basins in southwestern Gondwana. *Gondwana Research*, *25*(4), 1380–1395. https://doi.org/10.1016/j.gr.2012.08.023

Hölzel, M., Grasemann, B., & Wagreich, M. (2006). Numerical modelling of clast rotation during soft-sediment deformation: A case study in miocene delta deposits. *International Journal of Earth Sciences*, *95*(5), 921–928. https://doi.org/10.1007/s00531-006-0070-1

Huuse, M., Le Heron, D.P., Dixon, R., Redfern, J., Moscariello, A., Craig, J., (2012). Glaciogenic reservoirs and hydrocarbon systems: an introduction. In: Huuse, M., Redfern, J., Le Heron, D.P., Dixon, R., Moscariello, A., Craig, J. (Eds.), Glaciogenic Reservoirs and Hydrocarbon Systems. 368. Geological Society, London, Special Publications, pp. 1–28.

Ineson, J. (1985). Submarine glide blocks from the Lower Cretaceous of the Antarctic Peninsula. *Sedimentology*, *32*(5), 659–670. https://doi.org/10.1111/j.1365-3091.1985.tb00480.x

Isbell, J.L., Miller, M.F., Wolfe, K.L., and Lenaker, P.A., (2003) Timing of late Paleozoic glaciation in Gondwana: Was glaciation responsible for the development of northern hemisphere cyclothems?, in Chan, M.A., and Archer, A.W., eds., Extreme Depositional Environments: Mega End Members in Geologic Time: Geological Society of America Special Paper 370, p. 5–24.

Isbell, J.L., Fraiser, M.L., Henry, L.C., (2008). Examining the complexity of environmental change during the late Paleozoic and early Mesozoic: Palaios, v. 23, no. 5-6, p. 267-269.

Isbell, J. L. (2010). Environmental and paleogeographic implications of glaciotectonic deformation of glaciomarine deposits within Permian strata of the Metschel tillite, Southern Victoria Land, Antarctica. *Late Paleozoic Glacial Events and Postglacial Transgressions in Gondwana*. https://doi.org/10.1130/2010.2468(03)

Isbell, J. L., Henry, L. C., Gulbranson, E. L., Limarino, C. O., Fraiser, M. L., Koch, Z. J., Ciccioli, P. L., and Dineen, A. A., (2012). Glacial paradoxes during the late Paleozoic ice age: Evaluating the equilibrium line altitude as a control on glaciation: Gondwana Research, v. 22, no. 1, p. 1-19.

Isbell, J. L., Vesely, F. F., Rosa, E. L. M., Pauls, K. N., Fedorchuk, N. D., Ives, L. R. W., McNall, N. B., Litwin, S. A., Borucki, M. K., Malone, J. E., & Kusick, A. R. (2021). Evaluation of physical and chemical proxies used to interpret past glaciations with a focus on the Late Paleozoic Ice Age. *Earth-Science Reviews*, *221*, 103756. https://doi.org/10.1016/j.earscirev.2021.103756

Ives, L.R.W., Isbell, J.L., 2021. A lithofacies analysis of a South Polar glaciation in the Early Permian: Pagoda Formation, Shackleton Glacier region, Antarctica. Journal of Sedimentary Research 91, 611-635.

Jamil, M., Siddiqui, N. A., Umar, M., Usman, M., Ahmed, N., Rahman, A. H., & Zaidi, F. K. (2021). Aseismic and seismic impact on development of soft-sediment deformation structures in deep-marine sand-Shaly Crocker fan in Sabah, NW Borneo. *Journal of King Saud University - Science*, *33*(6), 101522. https://doi.org/10.1016/j.jksus.2021.101522

Jerolmack, D. J., & Swenson, J. B. (2007). Scaling relationships and evolution of distributary networks on wave-influenced deltas. Geophysical Research Letters, 34, L23402. https://doi.org/10.1029/2007GL031823

Kneller, B. C. (1995). Beyond the turbidite paradigm: physical models for deposition of turbidites and their implications for reservoir potential. In: Characterization of Deep Marine Systems (Eds A.J. Hartley and D.J. Prosser), Geol. Soc. Spec. Publ., 94, 31–49.

Kneller, B., Dykstra, M., Fairweather, L., & Milana, J. P. (2016). Mass-transport and slope accommodation: Implications for turbidite sandstone reservoirs. AAPG Bulletin, 100, 213–235.

Kvalstad, T.J., Andresen, L., Forsberg, C.F., Berg, K., Bryn, P., Wangen, M., (2005). The Storegga Slide: evaluation of triggering sources and slide mechanics. Mar. Pet. Geol. 22, 245e256.

Lackey, J., Moore, G., & Strasser, M. (2018). Three-dimensional mapping and kinematic characterization of mass transport deposits along the outer Kumano Basin and Nankai accretionary wedge, Southwest Japan. *Progress in Earth and Planetary Science*, *5*(1). https://doi.org/10.1186/s40645-018-0223-4

Lawson, D.E. (1979a). Sedimentological analysis of the western terminus region of the Matanuska Glacier, Alaska. CRREL Report 79-9, Hanover, NH.

Lawson, D.E. (1981a). Distinguishing characteristics of diamictons at the margin of the Matanuska Glacier, Alaska. Annals of Glaciology 2, 78–84.

Lawson, D.E. (1989). Glacigenic resedimentation: classification concepts and application to mass movement processes and deposits. In: Goldthwait, R.P., Matsch, C.L. (Eds.), Genetic Classification of Glacigenic Deposits. Balkema, Rotterdam, pp. 147–169.

Lewis, K.B., (1971). Slumping on a continental slope inclined at 1–4 . Sedimentology 16, 97–110.

Limarino, C., & Gutierrez, P. (1990). Diamictites in the Agua Colorada Formation (northwestern Argentina): New evidence of carboniferous glaciation in South America. *Journal of South American Earth Sciences*, *3*(1), 9–20. https://doi.org/10.1016/0895-9811(90)90014-r

Limarino, C. O., Césari, S. N., Net, L. I., Marenssi, S. A., Gutierrez, R. P., & Tripaldi, A. (2002). The upper carboniferous postglacial transgression in the Paganzo and Río Blanco Basins (northwestern Argentina): Facies and stratigraphic significance. *Journal of South American Earth Sciences*, *15*(4), 445–460. https://doi.org/10.1016/s0895-9811(02)00048-2

Limarino, C.O., Tripaldi, A., Marenssi, S., Fauqué, L., (2006). Tectonic, sea-level, and climatic controls on Late Paleozoic sedimentation in the western basins of Argentina. Journal of South American Earth Sciences 33, 305-226.

Limarino, C. O., Césari, S. N., Spalletti, L. A., Taboada, A. C., Isbell, J. L., Geuna, S., & Gulbranson, E. L. (2014). A paleoclimatic review of southern South America during the late Paleozoic: A record from Icehouse to extreme greenhouse conditions. *Gondwana Research*, *25*(4), 1396–1421. https://doi.org/10.1016/j.gr.2012.12.022

Limarino, C. O., & López-Gamundí, O. R. (2021). Late Paleozoic basins of South America: Insights and progress in the last decade. *Journal of South American Earth Sciences*, *107*, 103150. https://doi.org/10.1016/j.jsames.2020.103150

López-Gamundí, O.R., Espejo, I.S., Conaghan, P.J., Powell, C.M., Veevers, J.J., 1994. Southern South America. Memoir - Geological Society of America 184, 281-329.

López-Gamundí, O.R.. (1997). Glacial-postglacial transition in the late Paleozoicbasins of southern South America, in Martini, I.P., ed., Late Glacial andPostglacial Environmental Changes, Quaternary, Carboniferous–Permianand Proterozoic: Oxford, UK, Oxford University Press, p. 147–168.
(12) (PDF) Introduction: Late Paleozoic glacial events and postglacial transgressions in Gondwana

López Gamundí, O.R. (1989). Postglacial transgressions in late paleozoic basins of Western Argentina: a record of glacioeustatic sea level rise. Palaeogeography, Palaeoclimatology, Palaeoecology 71, 257–270. (López-Gamundí, O.R., 1997)

López-Gamundí, O. R., & Buatois, L. A. (2010). Introduction: Late Paleozoic glacial events and postglacial transgressions in Gondwana. *Late Paleozoic Glacial Events and Postglacial Transgressions in Gondwana*. https://doi.org/10.1130/2010.2468(00)

López-Gamundí, O., Limarino, C. O., Isbell, J. L., Pauls, K., Césari, S. N., & Alonso-Muruaga, P. J. (2021). The late paleozoic ice age along the southwestern margin of Gondwana:

Facies models, age constraints, correlation and sequence stratigraphic framework. *Journal of South American Earth Sciences*, *107*, 103056. https://doi.org/10.1016/j.jsames.2020.103056

Lowe, D., & LoPiccolo, R. (1974). The characteristics and origins of Dish and pillar structures. *SEPM Journal of Sedimentary Research*, *Vol. 44*. https://doi.org/10.1306/74d72a68-2b21-11d7-8648000102c1865d

Lowe, D.R. (1982). Sediment gravity flows II: depositional models with special reference to the deposits of high density turbidity currents. J. Sed. Petrol., 52, 279–297.

Lowe, D. R. (2006). Water escape structures in coarse-grained sediments. *Deep-Water Turbidite Systems*, 114–114. https://doi.org/10.1002/9781444304473.ch10

Lucente, C. C. (2003). Anatomy and emplacement mechanism of a large submarine slide within a miocene foredeep in the Northern Apennines, Italy: A field perspective. *American Journal of Science*, *303*(7), 565–602. https://doi.org/10.2475/ajs.303.7.565

Malone, J. R., Malone, J. E., Isbell, J. L., Malone, D. H., Craddock, J. P., & Pauls, K. N. (2024). Unmixing detrital Zircon U-PB ages reveals tectonic and climatic depositional influences on the Carboniferous Ansilta Formation, Calingasta-Uspallata Basin, Western Argentina. *Geoscience Frontiers*, *15*(4), 101807. https://doi.org/10.1016/j.gsf.2024.101807

Malone, J. E., Malone, J. R., Isbell, J. L., & Malone, D. H. (2023). Unmixing sediment sources of the Carboniferous Ansilta Formation of the calingasta-uspallata basin, Western Argentina. *Geological Society of America Abstracts with Programs*. https://doi.org/10.1130/abs/2023am-395883

Malone, J.R., Malone, J.E., Isbell, J.L., Malone, D.H., Craddock, J.P., Pauls, K.N., 2024. Unmixing detrital zircon U-Pb ages reveals tectonic and climatic depositional influences on the Carboniferous Ansilta Formation, Calingasta-Uspallata Basin, Western Argentina. Geoscience Frontiers, 101807.

Marenssi, S. A., Tripaldi, A., Limarino, C. O., & Caselli, A. T. (2005). Facies and architecture of a carboniferous grounding-line system from the Guandacol Formation, Paganzo Basin, northwestern Argentina. *Gondwana Research*, *8*(2), 187–202. https://doi.org/10.1016/s1342-937x(05)71117-5

Martinsen, O. (1994). Mass movements. *The Geological Deformation of Sediments*, 127–165. https://doi.org/10.1007/978-94-011-0731-0_5

Martinsen, O. J., & Bakken, B. (1990). Extensional and compressional zones in slumps and slides in the namurian of county clare, Ireland. *Journal of the Geological Society*, *147*(1), 153–164. https://doi.org/10.1144/gsjgs.147.1.0153 (Martinsen & Bakken, 1990)

Maltman, A.J., Bolton, A., (2003). How sediments become mobilized. Subsurface. Sediment Mobilization 216, 9–20. https://doi.org/10.1144/GSL.SP.2003.216.01.02.

McNall, Natalie Beatrice, "Sedimentological and Geochemical Analysis of Deep-Water Deposits in the Mojón De Hierro Formation at Arroyo Garrido, Tepuel-Genoa Basin, Patagonia, Argentina" (2019). *Theses and Dissertations*. 2226.

Meiburg, E., & Kneller, B. (2010). Turbidity currents and their deposits. *Annual Review of Fluid Mechanics*, *42*(1), 135–156. https://doi.org/10.1146/annurev-fluid-121108-145618

Micallef, A., Masson, D. G., Berndt, C., & Stow, D. A. V. (2007). Morphology and mechanics of submarine spreading: A case study from the Storegga Slide. *Journal of Geophysical Research: Earth Surface, 112*.

Middleton, G.V. (1966). Experiments on density and turbidity currents. I. Motion of the head. Can. J. Earth Sci., 3, 523±546.

Middleton, G.V. and Hampton, M.A. (1976). Subaqueous sediment transport and deposition by sediment gravity flows. In: Marine Sediment Transport and Environmental Management (Eds Stanley, D.J. and Swift, D.J.P.), p. 197218. Wiley, New York.

Milana, J. P., Kneller, B., & Dykstra, M. (2010). Mass-transport deposits and turbidites, syn-to-post-glacial carboniferous basins of Western Argentina. *ISC 2010F Guid*, 01-88.

Mohrig, D., Ellis, C., Parker, G., Whipple, K. X., & Hondzo, M. (1998). Hydroplaning of subaqueous debris flows. *Geological Society of America Bulletin, 110*, 387–394.

Montañez, I.P., Tabor, N.J., Niemeier, D., DiMichele, W.A., Frank, T.D., Fielding, C.R., Isbell, J.L., Birgenheir, L.P., Rygel, M.C. (2007). CO2-forced climate and vegetative instability during late Paleozoic deglaciation: Science 315, 87–91.

Montañez, I.P., Poulsen, C.J. (2013). The late Paleozoic ice age: An evolving paradigm: Annual Review of Earth and Planetary Sciences, v. 41, p. 24.1-24.

Montañez, I.P., McElwain, J.C., Poulsen, C.J., White, J.D., DiMichele, W.A., Wilson, J.P., Griggs, G., Hren, M.T., (2016). Climate, pCO2 and terrestrial carbon cycle linkages during late Palaeozoic glacial-interglacial cycles. Nature Geoscience 9, 824-828.

Moretti, M., Alfaro, P., Caselles, O., Canas, J.A., (1999). Modelling seismites with a digital shaking table. Tectonophysics, 304, Pp. 369–383.

Moretti, M., & Sabato, L. (2007). Recognition of trigger mechanisms for soft-sediment deformation in the pleistocene lacustrine deposits of the Sant'arcangelo Basin (Southern Italy): Seismic shock vs. overloading. *Sedimentary Geology*, *196*(1–4), 31–45. https://doi.org/10.1016/j.sedgeo.2006.05.012

Morgenstern, N.R. 1967. Submarine slumping and the initiation of turbidity currents. In: Richards, A.F. (Ed.). Marine Geotechnique. University of Illinois Press, Champaign, IL, pp. 189–220.

Moscardelli, L., Wood, L., Mann, P., (2006). Mass-transport complexes and associated processes in the offshore area of Trinidad and Venezuela. AAPG Bulletin 90, 1059–1088.

Moxness, L. D., Isbell, J. L., Pauls, K. N., Limarino, C. O., & Schencman, J. (2018). Sedimentology of the mid-carboniferous fill of the Olta Paleovalley, eastern paganzo basin, Argentina: Implications for glaciation and controls on diachronous deglaciation in western Gondwana during the Late Paleozoic Ice Age. *Journal of South American Earth Sciences*, *84*, 127–148. https://doi.org/10.1016/j.jsames.2018.03.015

Mulder, T., & Alexander, J. (2001). The physical character of subaqueous sedimentary density flows and their deposits. *Sedimentology*, *48*(2), 269–299. https://doi.org/10.1046/j.1365-3091.2001.00360.x

Mutti, E., & Ricci Lucchi, F., (1972). Le torbiditi dell'Appennino settentrionale: introduzioni all'analisi de facies: Società Geologica Italiana Memorie, v. 11, p. 161–199.

Mutti, E., Ricci Lucchi, F., Seguret, M. and Zanzucchi, G. (1984). Seismoturbidites: a new group of resedimented deposits. Mar. Geol., 55, 103–116.

Mutti, E., & Normark, W. R. (1987). Comparing examples of modern and ancient turbidite systems: Problems and concepts. In J. K. Leggett & G. G. Zuffa (Eds.), *Marine clastic sedimentology: Concepts and case studies* (pp. 1–38). Graham and Trotman.

Mutti, E., Carminatti, M., Moreira, J.L.P., Grassi, A.A. (2006). Chaotic deposits: examples from the Brazilian offshore and from outcrop studies in the Spanish Pyrenees and Northern Apennines, Italy. A.A.P.G. Annual Meeting, April 9–12, Houston, Texas.

Naves de Lima Rodrigues, M. C., Trzaskos, B., Alsop, G. I., Farias Vesely, F., Mottin, T. E., & Buzatto Schemiko, D. C. (2021). Statistical analysis of structures commonly used to

determine palaeoslopes from within mass transport deposits. *Journal of Structural Geology*, *151*, 104421. https://doi.org/10.1016/j.jsg.2021.104421

Nemec, W. (1990). Aspects of sediment movement on steep delta slopes. In: Colella, A., Prior, D. (Eds.), Coarse-Grained Deltas. International Association of Sedimentologists, Special Publication 10, pp. 29 – 73.

Nichols, R.L., (1961). Characteristics of beaches formed in polar climates. Am. J. Sci. 259 (9), 694–708.

Nichols, R. J. (1995). The liquefaction and remobilization of sandy sediments. In A. J. Hartley & D. J. Prosser (Eds.), *Characterization of deep marine clastic systems* (pp. 63–76). Geological Society, London, Special Publications, 94.

Nichols, G. (2023). *Sedimentology and Stratigraphy*. Wiley.

Ogata, K., Mutti, E., Pini, G. A., & Tinterri, R. (2012). Mass transport-related stratal disruption within sedimentary mélanges: Examples from the northern Apennines (Italy) and south-central Pyrenees (Spain). *Tectonophysics*, *568–569*, 185–199. https://doi.org/10.1016/j.tecto.2011.08.021

Ogata, K., Mountjoy, J.J., Pini, G.A., Festa, A., Tinterri, R., (2014). Shear zone liquefaction in mass transport deposit emplacement: a multi-scale integration of seismic reflection and outcrop data. Mar. Geol. 356, 50–64. https://doi.org/10.1016/j.margeo.2014. 05.001.

Omosanya, K.O., Alves, T.M., (2013). Ramps and flats of mass-transport deposits (MTDs) as markers of seafloor strain on the flanks of rising diapirs (Espírito Santo Basin, SE Brazil). Mar. Geol. 340, 82–97. https://doi.org/10.1016/j.margeo.2013.04.013.

Owen, G. (1987). Deformation processes in unconsolidated sands. In M. E. Jones & R. M. F. Preston (Eds.), *Special Publications, Geological Society, London* (Vol. 29, pp. 11–24).

Oyanyan, R. O. (2020). Soft-sediment deformation structures and granulometric properties distribution in Ajali sandstone ridges, western Afikpo Basin, Uturu, Nigeria. *Earth Science Malaysia*, *5*(2), 77–85. https://doi.org/10.26480/esmy.02.2021.77.85

Pauley, J.C. (1995). Sandstone megabeds from the Tertiary of the North Sea. In: Characterization of Deep Marine Clastic Systems (Eds A.J. Hartley and D.J. Prosser), vol. 94, pp. 103–114. SEPM Special Publications, London.

Pauls, K.N., Isbell, J.L., McHenry, L.J., Limarino, C.O., Moxness, L.D., CSchencman, L.J., (2019). A paleoclimatic reconstruction of the Carboniferous-Permian paleovalley fill in the

eastern Paganzo Basin: Insights into glacial extent and deglaciation of southwestern Gondwana. Journal of South American Earth Sciences 95, 14.

Pauls, Kathryn N. (2020) "Late Paleozoic Climatic Reconstruction of Western Argentina: Glacial Extent and Deglaciation of Southwestern Gondwana" *Theses and Dissertations*. 2576.

Pauls, K. N., Isbell, J. L., Limarino, C. O., Alonso-Murauga, P. J., Malone, D. H., Schencman, L. J., Colombi, C. E., & Moxness, L. D. (2021). Constraining late Paleozoic ice extent in the Paganzo Basin of western argentina: Provenance of the lower paganzo group strata. *Journal of South American Earth Sciences*, *106*, 102899. https://doi.org/10.1016/j.jsames.2020.102899

Peters, S. E., & Loss, D. P. (2012). Storm and fair-weather wave base: A relevant distinction? *Geology*, *40*(6), 511–514. https://doi.org/10.1130/g32791.1

Pickering, K.T., Corregidor, J., (2005) Mass-transport complexes (MTCs) and tectonic control on basin-floor submarine fans, middle Eocene, south Spanish Pyrenees. Journal of Sedimentary Research 75, 761-783.

Pickering, K. T., & Hiscott, R. N. (2016). *Deep-marine systems: Processes, deposits, environments, tectonics and sedimentation*. John Wiley & Sons Inc.

Posarnentier, H. W., & Allen, G. P. (1999). Fundamental concepts of sequence stratigraphy. *Siliciclastic Sequence Stratigraphy*, 9–51. https://doi.org/10.2110/csp.99.07.0009

Posamentier, H. W., & Kolla, V. (2003). Seismic geomorphology and stratigraphy of depositional elements in deep-water settings. *Journal of Sedimentary Research, 73*, 367–388.

Posamentier, H. W., & Walker, R. G. (2006). Deep-water turbidites and submarine fans. *Facies Models Revisited*, 399–520. https://doi.org/10.2110/pec.06.84.0399 Posamentier, H.W. & Martinsen, O.O.J. (2011). The character and genesis of submarine mass-transport deposits: Insights from outcrop and 3D seismic data. In Shipp, R.C., Weimer, P., Posamentier, H.W. (Eds.), Mass-transport deposits in deepwater settings, SEPM.

Porębski, S.J., Steel, R.J., (2003). Shelf-margin deltas: their stratigraphic significance and relation to Deepwater sands. Earth-Science Reviews 62 (3–4), 283–326.

Powell, R. D. (1984). Glacimarine processes and inductive lithofacies modelling of Ice Shelf and Tidewater Glacier sediments based on quaternary examples. *Marine Geology*, *57*(1–4), 1–52. https://doi.org/10.1016/0025-3227(84)90194-4

Quirk, D.G., Schødt, N., Lassen, B., Ings, S.J., Hsu, D., Hirsch, K.K., Von Nicolai, Ch, (2012). Salt tectonics on passive margins: examples from Santos, Campos and Kwanza basins. Geological Society London, Special Publications, 363, pp. 207e244.

Ramos, V. A. (1988). The tectonics of the Central Andes; 30° to 33° S latitude. *Geological Society of America Special Papers*, 31–54. https://doi.org/10.1130/spe218-p31

Ramsay, J. G., & Huber, M. I. (1983). *The techniques of modern structural geology*. Acad. Pr.

Rodríguez-López, J. P., Meléndez, N., Soria, A. R., Liesa, C. L., & Van Loon, A. J. (Tom). (2007). Lateral variability of ancient seismites related to differences in sedimentary facies (the SYNRIFT escucha formation, mid-Cretaceous, eastern Spain). *Sedimentary Geology*, *201*(3–4), 461–484. https://doi.org/10.1016/j.sedgeo.2007.07.009

Rosa, E. L. M., & Isbell, J. L. (2021). Late Paleozoic glaciation. *Encyclopedia of Geology*, 534–545. https://doi.org/10.1016/b978-0-08-102908-4.00063-1

Rotzien, J.R., Hernández-Molina, F.J., Fonnesu, M., Thieblemont, A., (2022) Chapter 7 - Deepwater sedimentation units, in: Rotzien, J.R., Yeilding, C.A., Sears, R.A., Hernández-Molina, F.J., Catuneanu, O. (Eds.), Deepwater Sedimentary Systems. Elsevier, pp. 203-249.

Rupke, N.A. (1972). Sedimentology of very thick calcarenitemarlstone beds in a flysch succession, south-west Pyrenees. Sedimentology, 23, 43–65.

Schermerhorn, L.J.G., (1974). Late Precambrian mixites: glacial and/or nonglacial? 1384 American Journal of Science 274, 673–824.

Schwarz, H.-U. (1986). Sedimentary processes and deformational structures in intramontane periglacial lake deposits of the Andine Carboniferous (río agua de la peña, Prov. San Juan, Argentina). *Zentralblatt Für Geologie Und Paläontologie, Teil I*, *1985*(9–10), 1295–1308. https://doi.org/10.1127/zbl_geol_pal_1/1985/1986/1295

Scotese, C. R., Boucot, A. J., and McKerrow, W. S. (1999). Gondwanan palaeogeography and palaeoclimatology: Journal of African Earth Sciences, v. 28, p. 99-114.

Sobiesiak, M. S., Kneller, B., Alsop, G. I., & Milana, J. P. (2016). Internal deformation and kinematic indicators within a tripartite mass transport deposit, NW Argentina. *Sedimentary Geology*, *344*, 364–381. https://doi.org/10.1016/j.sedgeo.2016.04.006

Sobiesiak, M. S., Alsop, G. I., Kneller, B., & Milana, J. P. (2017). Sub-seismic scale folding and thrusting within an exposed mass transport deposit: A case study from NW Argentina. *Journal of Structural Geology*, *96*, 176–191. https://doi.org/10.1016/j.jsg.2017.01.006

Sobiesiak, M. S., Kneller, B., Alsop, G. I., & Milana, J. P. (2018). Styles of basal interaction beneath mass transport deposits. *Marine and Petroleum Geology*, *98*, 629–639. https://doi.org/10.1016/j.marpetgeo.2018.08.028

Sobiesiak, M. S., Buso, V. V., Kneller, B., Alsop, G. I., & Milana, J. P. (2019). Block generation, deformation, and interaction of mass-transport deposits with the seafloor. *Geophysical Monograph Series*, 91–104. https://doi.org/10.1002/9781119500513.ch6

Socha, B., Carignano, C., Rabassa, J., & Mickelson, D. (2014). Gondwana glacial paleolandscape, diamictite record of Carboniferous Valley glaciation, and preglacial remnants of an ancient weathering front in northwestern Argentina. *Gondwana Landscapes in Southern South America*, 331–363. https://doi.org/10.1007/978-94-007-7702-6_12

Spalletti, L. A., Limarino, C. O., Colombo, F., Ciccioli, P. L., & Colombi, C. E. (2023). Sandstone petrofacies, deformational events and the dynamic of the Valle Fértil lineament during the late paleozoic (Paganzo Basin, northwestern Argentina). *Journal of South American Earth Sciences*, *121*, 104106. https://doi.org/10.1016/j.jsames.2022.104106

Starck, D., Bordese, S., Guibaldo, C., Hernández, R., (2021). Size and style of the Gondwana late Paleozoic ice cover: Insights from U-Pb dating of the Tarija Formation granitic boulders. Journal of South American Earth Sciences, 102954.

Steel, R., Porębski, S.J., Plink-Bjorklund, P., Mellere, D., Schellpeper, M., 2013. Shelfedge delta types and their sequence-stratigraphic relationships. Syvitski, J. P., Smith, J. N., Calabrese, E. A. and Boudreau, B. P. (1988). Basin sedimentation and the growth of prograding deltas. J. Geophys. Res. Oceans 93 (C6), 6895–6908.

Sterren, A. F., & Martínez, M. (1996). XIII Congreso Geológico Argentino y III Congreso de Exploración de Hidrocarburos, Actas II: 89-103 El Paleovalle De Olta (Carbonifero): Paleoambiente y Paleogeografia. In *Actas del... Congreso Geológico Argentino* (Vol. 2, p. 89). Congreso Geologico Argentino, distributed by Librart.

Sterren, A.F., Martínez, M., (1996). El paleovalle de Olta (Carbonífero): paleoambientes y paleogeografía. In: 13o Congreso Geológico Argentino y 3o Congreso Exploración de Hidrocarburos (Buenos Aires), vol. 2. Actas, pp. 89–103.

Strachan, L. J. (2008). Flow transformations in slumps: A case study from the Waitemata Basin, New Zealand. *Sedimentology*, *55*(5), 1311–1332. https://doi.org/10.1111/j.1365-3091.2007.00947.x (Sterren, 2008)

Straub, K. M., Paola, C., Mohrig, D., Wolinsky, M. A., & George, T. (2009). Compensational stacking of channelized sedimentary deposits. *Journal of Sedimentary Research*, *79*(9), 673–688. https://doi.org/10.2110/jsr.2009.070

Stow, D. A. V., & Johansson, M. (2000). Deep-water massive sands: Nature, origin, and hydrocarbon implications. *Marine and Petroleum Geology, 17*, 145–174.

Suss, J.F., Vesely, F.F., Santa Catharina, A., Assine, M.L., Paim, P.S.G. (2014). O grupo itararé (Neocarbonífero-eopermiano) entre porto amazonas (PR) e mafra (SC): Sedimentação gravitacional em contexto marinho deltaico com influência glacial. Geociencias 33, 701–719.

Syvitski, J.P.M., Shaw, J. (1995). Sedimentology and geomorphology of fjords. In: Perillo, G. M.E. (Ed.), Geomorphology and Sedimentology of Estuaries. Developments in Sedimentology 53. Elsevier, Amsterdam, pp. 113–178.

Talling, P.J. (2013). Hybrid submarine flows comprising turbidity current and cohesive debris flow: deposits, theoretical and experimental analyses, and generalized models. Geosphere, 9, 460–488.

Talling, P. J., Masson, D. G., Sumner, E. J., & Malgesini, G. (2012). Subaqueous sediment density flows: Depositional processes and deposit types. *Sedimentology*, *59*(7), 1937–2003. https://doi.org/10.1111/j.1365-3091.2012.01353.x

Terry, R.D.; Chilingarian, G.V. Summary of "Concerning some additional aids in studying sedimentary formations" by M.S. Shvetsov. J. Sediment. Petrol. 1955, 25, 229-234.

Terzaghi, K. (1947). Shear characteristics of quicksand and soft clay. *Proceedings of the 7th Texas Conference on Soil Mechanics and Foundation Engineering*, 1–8.

Thomas, G.S.P., Connell, R.J., (1985). Iceberg drop, dump, and grounding structures from Pleistocene glacio-lacustrine sediments, Scotland. J. Sediment. Petrol. 55 (2), 243–249.

Thornton, S.E. (1986). Origin of mass flow sedimentary structures in Hemipelagic basin deposits: Santa Barbara basin, California Borderland. Geo Mar. Lett. 6, 15–19. https://doi.org/10.1007/BF02311691.

Tripsanas, E. K., Bryant, W. R., & Prior, D. B. (2003). Structural characteristics of cohesive gravity-flow deposits, and a sedimentological approach on their flow mechanisms. *Advances in Natural and Technological Hazards Research*, 129–136. https://doi.org/10.1007/978-94-010-0093-2_15

Valdez-Buso, V., Milana, J.P., di Pasquo, M., Aburto, J.E., (2021). The glacial paleovalley of Vichigasta: Paleogeomorphological and sedimentological evidence for a large continental ice-sheet for the mid-Carboniferous over central Argentina. Journal of South American Earth Sciences, 103066.

Valdez Buso, V., Kneller, B., da Silva Reis Assis, V., Farias Vesely, F., & Milana, J. P. (2024). Incorporation of substrate blocks into mass transport deposits: Insights from subsurface and outcrop studies. *The Depositional Record*, *10*(5), 708–719. https://doi.org/10.1002/dep2.283

Van Der Wateren, F. M. (1994). Proglacial subaquatic outwash fan and delta sediments in push moraines-indicators of subglacial meltwater activity. Sedimentary Geology 91: 145-172.

Van der Wateren, F.M.. (1995). Structural geology and sedimentology of push moraines; processes of soft sediment deformation in a glacial environment and the distribution of glaciotectonic styles. In: Mededelingen - Rijks Geologische Dienst, 54. Nederlands Instituut voor Toegepaste Geowetenschappen TNO, Haarlem, Netherlands 167 pp.

Van Der Wateren, F. M. (2002). Processes of glaciotectonism. In: Menzies, J., ed. Modern and past glacial environments. Oxford: Butterworth-Heinemann, pp. 417-443.

Varnes, D.J. (1978). Slope movement types and processes. In: Schuster, R.L., Krizek, R.J. (Eds.), Landslides, Analysis and Control. Special Report 176. National Academy of Sciences, Washington, pp. 11–33.

Veevers, J. J., and Powell, C. M. (1987), Late Paleozoic glacial episodes in Gondwanaland reflected in transgressive-regressive depositional sequences in Euramerica: Geological Society of America Bulletin, v. 98, p. 475-487.

Vesely, F. F., Rodrigues, M. C. N. L., da Rosa, E. L. M., Amato, J. A., Trzaskos, B., Isbell, J. L., & Fedorchuk, N. D. (2018). Recurrent emplacement of non-glacial diamictite during the Late Paleozoic Ice Age. *Geology*, *46*(7), 615–618. https://doi.org/10.1130/g45011.1

Visser, J.N.J. (1987). The palaeogeography of part of southwestern Gondwana during the Permo-Carboniferous glacaiation: Palaeogeography, Palaeoclimatology, Palaeoecology, v. 61, p. 205-219.

Walker, R.G. (1978). Deep-water sandstone facies and ancient submarine fans: models for exploration and stratigraphic traps: American Association of Petroleum Geologists, Bulletin, v. 62, p. 932–966.

Wang, P., Du, Y., Yu, W., Algeo, T. J., Zhou, Q., Xu, Y., Qi, L., Yuan, L., & Pan, W. (2020). The chemical index of alteration (CIA) as a proxy for climate change during glacial-interglacial transitions in Earth history. *Earth-Science Reviews*, *201*, 103032. https://doi.org/10.1016/j.earscirev.2019.103032

Weimer, P. (1989) Sequence stratigraphy of the Mississippi fan (Plio-Pleistocene), Gulf of Mexico. Geo-Mar. Lett., 9, 185–272.

Weimer, P. and Shipp, C. (2004). Mass transport complex: musing on past uses and suggestions for future directions. In: Offshore Technology Conference: Offshore Technology Conference, p. 1–10. https://doi.org/10.4043/16752-ms

Wentworth, C. (1967). Dish structure, a primary sedimentary structure in coarse turbidites: Abstract. *AAPG Bulletin*, *51*. https://doi.org/10.1306/5d25c097-16c1-11d7-8645000102c1865d

Whitehouse, P., (2018). Glacial isostatic adjustment modelling: Historical perspectives, recent advances, and future directions. Earth Surface Dynamics 6, 401-429.

Woodcock, N.H., 1979. The use of slump structures as palaeoslope orientation estimators. Sedimentology 26, 83–99. https://doi.org/10.1111/j.1365-3091.1979. tb00339.x.

Y. K. Sohn . (1997). Characteristics and depositional processes of large-scale gravelly gilbert-type foresets in the miocene doumsan fan delta, Pohang Basin, Se Korea. *SEPM Journal of Sedimentary Research*, *Vol. 67*. https://doi.org/10.1306/d4268513-2b26-11d7-8648000102c1865d

Ziegler, A.M., Hulver, M.L., Rowley, D.B. (1997). Permian world topography and climate, in Martini, I.P., ed., Late glacial and post-glacial environmental changes-Quaternary, Carboniferous-Permian and Proterozoic: New York, Oxford University Press, p. 111-146.